ALMA MATER STUDIORUM – UNIVERSITÀ DI BOLOGNA

DOTTORATO DI RICERCA IN
Ingegneria civile, chimica, ambientale e dei materiali
Ciclo 34

Settore Concorsuale: 08/A2 - INGEGNERIA SANITARIA - AMBIENTALE, INGEGNERIA DEGLI IDROCARBURI E FLUIDI NEL SOTTOSUOLO, DELLA SICUREZZA E PROTEZIONE IN AMBITO CIVILE
Settore Scientifico Disciplinare: ING-IND/30 - IDROCARBURI E FLUIDI DEL SOTTOSUOLO

CHARACTERIZATION OF FIRST SORPTION CYCLE OF WHITE PORTLAND CEMENT BY ^{1}H NMR

PRESENTATA DA Anastasiia Nagmutdinova

COORDINATORE DOTTORATO
PROF. ALLESANDRO TUGNOLI

RELATORE
PROF. VILLIAM BORTOLOTTI

CORRELATORI
PROF.SSA PAOLA FANTAZZINI
DR. LEONARDO BRIZI

Esame finale anno *2022*

1 Acknowledgement

Through this work I experienced a great support and aid, without which this dissertation would not exist.

I would firstly like to thank my supervisor Villiam Bortolotti for his constant help, guidance, insightful comments and feedback. You pushed me to achieve the best possible results and helped to pull this work to a higher level.

Also, I would like to express my gratitude to my co-supervisors Paola Fantazzini and Leonardo Brizi. Your thoughtful suggestions, observations and much needed criticism helped to sharpen my knowledge and to come up with this work successfully.

I would like to thank the Horizon 2020 – Marie Skłodowska-Curie – Innovative Training Network (ITN) – 2017 Actions foundation program. This work would not be possible without Marie Skłodowska-Curie foundation.

I would like to acknowledge all other involved in ERICA program, those who gave me a great opportunity to learn and to gain different experience. I am thankful toward my fellow ESR colleagues for their help through all years of PhD.

Finally, I would like to express my gratitude to my family and friends. You supported me through the tough time and helped me to stay afloat.

2 Abstract

The work carried out in this PhD thesis is focused on the exploration of processes occurring in cement materials during sorption cycles by means of Nuclear Magnetic Resonance (NMR) relaxometry, and it is part of a Marie Curie H2020 European project named ERICA. Long (months) and short (days-weeks) sorption cycles of cement materials were explored. Overall, the long cycle consists of around 6 months of drying and wetting cement samples of different sizes and different water-to-cement ratios in a home-made relative humidity (RH) chamber. During the whole process, temperature and RH were monitored with a data-logger. The measurements were done at specific RH levels in the range 100% - 5% RH. Short cycles were performed by drying samples of different sizes and water-to-cement ratios in the oven at 60 ˚C for several days and re-wetting the samples underwater for up to two weeks. Different NMR techniques, such as one- and two-dimensional relaxometry and solid-signal analyses, were used to study the samples.

Firstly, in this work, by the interpretation of quasi-continuous distributions of T_2 relaxation time, we were able to resolve the cement isotherms components and to investigate changes in the cement pore size distributions. It was found that some reversible and irreversible changes concerning smaller porosity happened during the first sorption cycle.

Secondly, possible water exchange between different pore populations inside the cement samples during rewetting were investigated with the use of 2D NMR measurements. Preliminary results on the T_1-T_2 maps, obtained by means of a new 2D NMR inversion algorithm (MUpen2D), showed water movement inside the cement samples subjected to sorption cycles.

Thirdly, the solid structure of cement samples was qualitatively investigated with T_1 measurements and, as far as we known, for the first time interpreted with the Pake-Doublet theory. Changes of the solid structure was observed, precisely variations of the amount of Ettringite during drying/wetting were proposed to take place.

Finally, a part of thesis work was dedicated to designing an uniliteral magnet of an NMR single-sided equipment, for in situ cement structure investigation, built in the framework of the ERICA project. The multi-cubic-blocks magnet structure design was performed using different specific CAD software, and the magnetic fields generated by RF coils of different geometries were investigated using a specially customized Matlab script. The magnet pulling forces among blocks were also calculated.

The single-sided NMR instrument equipped with the designed single-sided magnet and coil was built by the ERICA partner company MR Solutions (Abingdon, UK), and the preliminary results demonstrated the correctness of the developed design. The instrument will be available to beneficiaries and partners of the ERICA project from winter 2022.

3 Scope and objectives of the thesis

Cement is one of the oldest and the most frequently used material in a wide range of applications. Unfortunately, cement production and its use cause emissions of greenhouse gases and dust, fuel combustion and health hazard for workers. Which brings the need of a more ecological approach to the cement industry. But, despite many scientific researches in the field of cement that were done in the last decades, the manufacture process, chemical formula of compositions and elements ratio have not had major changes. Chemical, internal crystal and pore structure are not completely determined. Therefore, the calcium-silicate-hydrate (C-S-H), that will be better discussed later, despite being the main phase, controlling the performance of cementitious materials, deserves further studies with new innovative approaches.

The Engineered Calcium-Silicate-Hydrates for Applications, Proposal number 764691 project (ERICA) to which this work belongs, serves for the purpose of exploring cementitious material on new, deep levels, and benefit the manufacture use. The research is divided into different packages, focused on different aspects of cementitious materials, such as chemical and crystalline structure, sorption, structure changes, transport properties etc., which is shown in Figure 3.1.1.

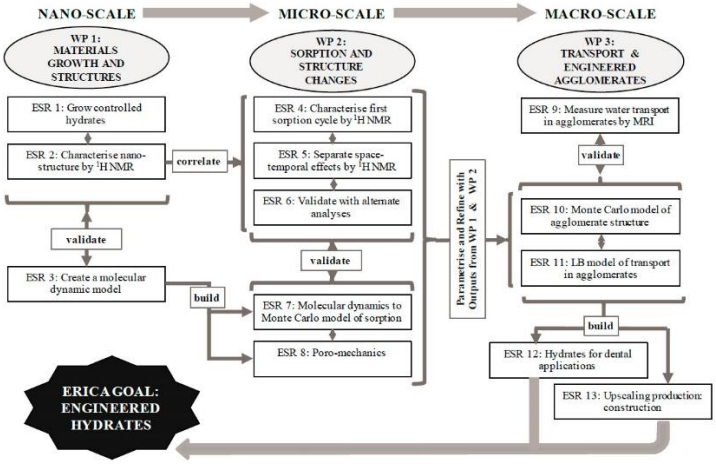

Figure 3.1.1 - Schematic of the ERICA project, divided by the scientific topics [1].

As part of the ERICA project, the scope of this work (ESR4 in Figure 3.1) is to address changes in porosity microstructure through the sorption cycles using ^{1}H NMR (Nuclear Magnetic Resonance). The task of the research is to measure the evolution of water filled porosity in hydrates of different, but controlled oxide mixes as the samples are moved around complete and partial cycles of the sorption loop at different rates (hours to months), using NMR technique with different exploration methods.

In particular, the major objectives of this work are:

- to understand the temporal dependence of the porosity in hydrates of different oxide compositions as the RH is cycled quickly (hours) and slowly (months) around full and partial drying / wetting cycles;
- to quantify the reversible and irreversible changes that occur and the severity of drying required for “structural relaxation”;
- to correlate results with NMR porosity and other analyses in previously done experiments;
- also, as a part of the ERICA project, to design an uniliteral magnet for the *in-situ* experiments on the construction cement sites, bridges, buildings etc.

4 Introduction

4.1 Porous medium

A porous medium could be described as a solid body with passages through which fluids can flow [2]. The skeletal portion of the material is often called “matrix” or “frame” [3].

A lot of different concepts exist to describe porous medium. One concept describes porous medium as a continuous solid with holes in it, a consolidated solid in which holes could be unconnected or connected. Another concept is for an unconsolidated material, a collection of solid particles in a packed bed, where the fluid can pass through the voids, unconsolidated [4].

The porous medium could be studied at two levels: microscopic and macroscopic [2]. At the microscopic level properties of the porous solids are studied as pore size distribution, degree of inter-connection and pore alignment, a fraction of dead-end pores (pores not accessible to the liquid), etc. The macroscopic approach is used to characterize bulk parameters on a scale larger than the pore size. These two approaches are complementary to one another. The microscopic description is necessary to study surface phenomena, for example, adsorption, and macroscopic is quiet enough to study heat and mass transfer [2].

One of the main characteristics of the porous system is the porosity, φ, defined as:

$$\varphi = \frac{Total\ volume\ - Solids\ vol.}{Total\ volume} \tag{4.1}$$

Porosity is defined as a fraction between 0 to 1 [4].

Pores of the solids could be described as micro-, meso- and macropores but as in different fields of study and even in different texts in the same field, the nomenclature varies. Therefore, it is important to define the ranges for the micropores, mesopores, and macropores. In Table 4.1.1 we show the nomenclature from the International Union of Pure and Applied Chemistry (IUPAC) (in catalysts), which will be used to define dimensions for the different pore classes [5]. The pore size is generally specified as the pore width defined as the average distance between the two opposite walls [6]. One should pay in mind, that the pore shape is nonhomogeneous and usually pores are approximated to spheres or planar pores.

Table 4.1.1 IUPAC dimensions for the different pores.

Pore sizes	IUPAC definition (Pore width)
Micropores	Not exceeding about 2.0 nm.
Mesopores	Pore of intermediate size, 2-50 nm.
Macropores	Exceeding about 50 nm

4.1.1 Cement as porous material

In cement studies, cement is considered a consolidated solid with connected pores. As a porous material, cement in general consists of air voids, capillary pores, gel pores, and sometimes interlayer spaces [7]. These structures will be described later in detail. Porosity of cementitious materials play big role in such properties as strength and durability [8].

Though in different works, authors give different dimensions for the classification of pores, and some difficulties for the direct comparison arise. In Figure 4.1.1 the nomenclature for cement pores from different researches is shown.

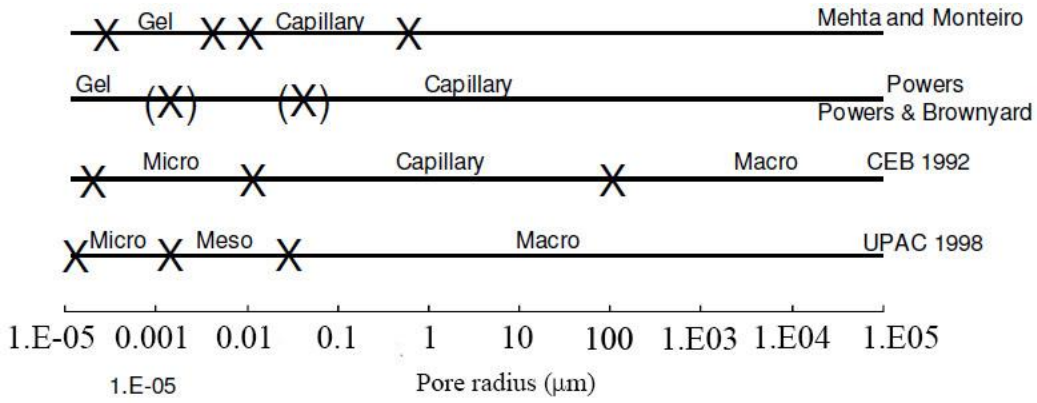

Figure 4.1.1 - Pore size dimensions in different works (adapted from [9]).

Porous structure of cement and its formation will be discussed later in more detail.

4.2 Portland Cement and its composition

Portland Cement (PC) is the most widely used building material in the world. The name Portland cement was firstly introduced by Joseph Aspdin in 1824 as the color of the mix resembled the stone from the Isle of Portland in Dorset (UK).

Different standards (for various purposes and of different origins) exist for PC mixes. For example, the ASTM Standard Specification for PC (ASTM C150) provides five different types of PC, with types 1 and 2 for general construction use [10] or in European and British standards - Class 42.5 Portland cement, named Ordinary Portland Cement (OPC) [11] (sometimes the name White Portland Cement is used (WPC)).

It is important to introduce the classification, as the name of cement is given to other binding materials. The first binder's classification was introduced by Romans, dividing them into non-hydraulic and hydraulic. However, such classification, assuming that the first sets by drying and the second is under-water, is not completely exact and a better distinction is done by assuming their water durability [12].

PC is a powder, which is produced by heating a mixture of limestone with clay or other materials up to the temperature of 1450˚C to get a clinker. Then, the clinker is mixed with a few percent of calcium sulfate and grounded. Calcium sulfate here plays a role in the strength of the material and controls the setting rate. Commonly, calcium sulfate is referred to as gypsum, but it could be replaced partly or fully by other materials [13].

Cement raw material consists of four main phases [14]:

- Tricalcium silicate $SiO_2 \cdot 3CaO$, called alite, takes 50-70% of PC. It reacts relatively quickly with water and is responsible for the strength development in normal PC in the first 28 days of setting.
- Dicalcium silicate $SiO_2 \cdot 2CaO$, called belite, takes 15-30% of PC clinker. It reacts with water slower than alite and determines to strength development at later ages.
- Tricalcium aluminate $Al_2O_3 \cdot 3CaO$, called aluminate, constitutes 5-10% of normal PC clinkers. It reacts fast with water and could cause rapid setting of the paste. For the prevention of the early setting, gypsum is usually added.
- Tetracalcicium ferroaluminate $4CaO \cdot Al_2O_3 \cdot Fe_2O_3$, called ferrite, and constitutes 5-15% of normal PC clinker. The speed of its reaction with water could be variable, but in general it is fast initially and slow at later ages.

In cement notation, these four elements usually are written as C_3S (alite), C_2S (belite), C_3A (aluminate) and C_4AF (ferrite), where S represents SiO_2, C – CaO, A – Al_2O_3, F – Fe_2O_3.

It should be noted that the chemical compositions of these phases are not pure and could be complicated by solid solutions. The chemical composition of clinker is extremely complex, however, the sum of the four components should follow a rule of higher than 95%, thus the phases crystallization process happens in the four components system [14].

4.2.1 Cement hydration and composition

Cement powder then is mixed with water with water/cement (w/c) or water/solid ratio in the range 0.3-0.6, which produces a consistent plastic mass, that is called "fresh cement paste". This paste sets and hardens while strength increases through hydration and the

“hardened cement paste” is produced. Here, “setting” means loss of plasticity and solid material development [15]. And hardening means the development of “hardness” and “strength” that follows the setting of the paste.

Hydration of cement (reaction of the cement clinker with water) is a complex process with a series of chemical reactions. The hydration process is influenced by a number of different factors:

1. The clinker phase composition and the presence of foreign ions in crystalline lattice;
2. Particle size of cement powder;
3. Water/cement ratio;
4. Setting temperature;
5. Presents of chemical admixtures;
6. The presence of additives, such as slag, fly ash etc.

Commonly, cement hydration is performed at room temperature. To prevent water evaporation during setting and hardening and reaction of the paste with CO_2 from the atmosphere, setting conditions may include initial storage in humid conditions, hardening under water or in 100% RH or storage in a sealed container [15].

The hydration process of PC is usually described through a calorimetry curve with a heat evolution over time. Tricalcium silicate, as it represents more than 60% in mass of the clinker is of paramount importance in the hydration reaction and is considered a good model for studying cement reaction with water.

Figure 4.2.1 shows the heat evolution of the PC during hydration process.

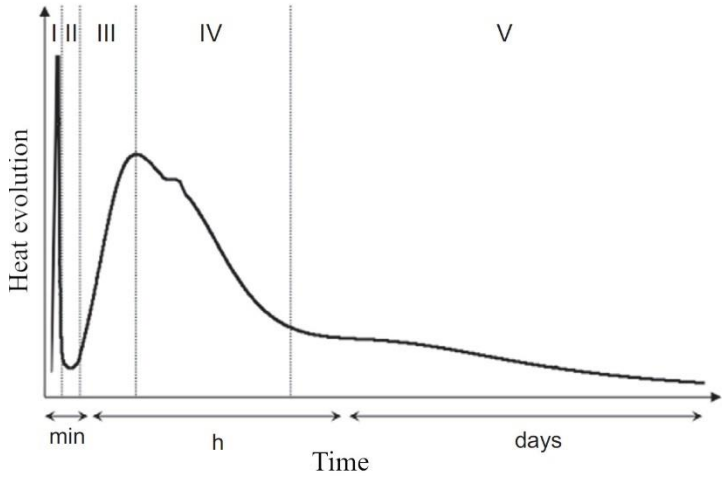

Figure 4.2.1 - Calorimetry curve of the PC through hydration process with highlighted five different phases (or stages), adapted from [14].

Phase I corresponds to the initial hydration of C_3S and C_3A, is called pre-induction period and takes place in the first minutes. Phase II is called “dormant period” or “induction period” in which the chemical activity is reduced and takes place in the first few hours.

The peak between phase III (acceleration phase, 3-11 hours) and IV (post-acceleration period) shows the main hydration of C_3S, while the shoulder in phase IV corresponds to the sulphate depletion point, which leads to massive hydration of C_3A. The hump in phase V corresponds to the transformation of Al_2O_3–Fe_2O_3-tri (AFt) to Al_2O_3–Fe_2O_3-mono (AFm).

The initial hydration of C_3S rises some controversial opinions and two hypotheses exist:

1. congregate dissolution;
2. incongruent dissolution with the formation of silica rich layer on the surface of C_3S.

These two hypotheses are difficult to be verified due to the low concentration of silica and difficulties in the separation of formed C-S-H from the surface of C_3S crystals.

However, it should be noted that data from ^{17}O and ^{29}Si NMR suggests a second model of hydration, which involves the formation of an active complex with five-coordinate Si, dissolution of Si tetrahedra and precipitation of the C-S-H phase [16].

C_3S and C_2S are transformed into nearly amorphous calcium silicate hydrate and hydrated lime $Ca(OH)_2$ by the reaction with water. The chemical composition of C-S-H is complex and could vary. C-S-H has properties of a rigid gel and acts as a binder. This rigid gel has porous structure with pore sizes from macroscopic level to interlayer spaces of the nanometre dimensions [15]. The dashes in the name indicate that no specific chemical composition is implied. For C-S-H, generally the formula CaO_x SiO_2 H_2O_y could be used, where *x* and *y* vary over a wide range [12].

The crystalline form of hydrated lime is called Portlandite.

The hydration reaction of C_3S and C_2S could be written as follows [14]:

(C_3S, C_2S) + water = C-S-H + portlandite

If the calcium sulphates are present, C_3A + C_4AF phase is transformed into Ettringite and monosulphoaluminate, which could be represented schematically as:

(C_3A, C_4AF) + calcium sulphate + water = ettringite + monosulphoaluminate.

Ettringite is a hydrous calcium aluminium sulfate and has a formula of $Ca_6Al_2(SO_4)_3(OH)_{12}\cdot 26H_2O$. Ettringite could form two phases depending on the ratio of calcium aluminate with calcium sulfate as a result of cement hydration [14]. The two phases are:

1. Aft or “alumina, ferric oxide, tri-sulfate”, has general formula $Ca_3(Al,Fe)(OH)_6 \cdot 12H_2O]_2 \cdot X_3 \cdot nH_2O$, where X represents a doubly charged onion;
2. AFm or “alumina, ferric oxide, mono-sulfate”, has general formula $[Ca_2(Al,Fe)(OH)_6)] \cdot X \cdot nH_2O$ $[Ca_2(Al,Fe)(OH)_6)]$ $X \cdot nH_2O$ where X represents a singly charged anion.

Figure 4.2.2 (a) shows a Scanning Electron Microscope (SEM) image of hardened WPC [17] with different phases indicated and (b) the C-S-H model, based on the Feldman-Sereda [18] and Jennings [19] models.

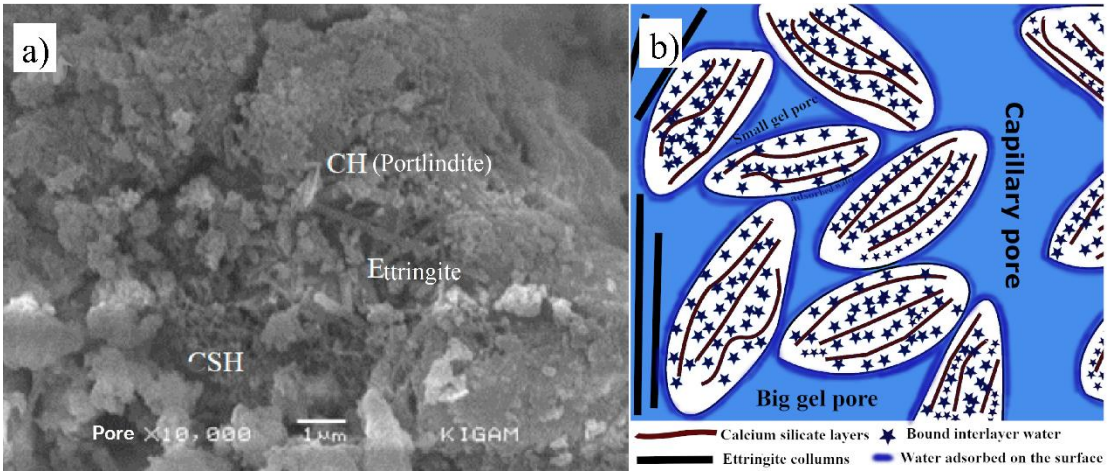

Figure 4.2.2 - Hardened PC structure, a) SEM image of hardened WPC, adapted from [17] b) C-S-H model, based on the Feldman-Sereda [18] and Jennings [19] models.

The morphology of hydrated paste could vary depending on the w/c ratio. With high w/c ratio, due to the big amount of space and water, the growth of hydrates is unhindered for a long time, leading to the large crystal formation, referred to as an outer product as it forms outside the boundaries of the initial cement particles. And with low w/c ratio, the hydration growth is hindered much sooner and water availability is limited, so the structure will be composed of amorphous C-S-H and poorly crystalized Portlandite [14].

The C-S-H phase formed during hydration of dicalcium silicate is similar to that formed during hydration of C_3S. In the same way, as for C_3S hydration, the C-S-H phase that is formed during the induction period is different from the one formed later, as it does not contain polymerized C-S-H sites (silicate species Q_1 and Q_2 by the ^{29}Si NMR spectroscopy), only single SiO_4 tetrahedra with Si–O–Ca bonds [15].

After the beginning of acceleratory period, cement paste starts to set. The amount of hydrated material increases, and the volume of the liquid phase decreases. Individual cement

particles develop chemical bonds with the hydrated material, that cover these particles. Eventually, a continuous network of solids develops within the paste.

It appears that C_3S and C_3A minerals hydration is responsible for the “normal” setting of the paste, due to the C-S-H and AFt phases formation [15].

As it was said, hydration of cement results in the heat release that is a function of the cement composition, and it is important to note that the amount of actually hydrated cement determines the amount of heat released.

The hydration process also leads to a volumetric contraction and as it may have consequences on the volumetric stability of the cement through the autogenous shrinkage, it is very important from a technological point of view. But, if the hydration process goes with the source of internal or external water, autogenous shrinkage could be significantly less [14].

To define the water content inside the cement samples, specified drying conditions should be examined.

The most hydrated state of the cement is that of the saturated paste, during which all the pores are fully filled with water. According to the Powers and Brownyard model (P-B model) [20] C-S-H could form only if enough space is available to have a defined proportion of pore space.

Thus, it could be said, that w/c ratio has a threshold value under which complete hydration is impossible, and such mature cement consists only of hydration products, including essential pore space. The water content of such paste in the saturated conditions is 42-44%, referred to as the ignited mass.

The hydration process of the tricalcium silicate for approximately 0.4 w/c ratio could be graphically displayed as follows in Figure 4.2.3 [21].

In Figure 4.2.3a, the un-hydrated cement paste is shown as isolated cement grains surrounded by water. At the beginning of hydration (33% in the Fig. 4.2.3b), primary Portlandite by the calcium hydroxide crystallization at numerous centers and other products from inner and outer hydration are produced. The growth of Portlandite is highly dendritic, as shown in Fig. 4.2.3c at 67% hydration. Here the un-hydrated cores surrounded by the inner products and the columnar zone of the outer product are growing on the outer surface of each grain. The dendritic growth probably leads the silica to be trapped in the inter-dendritic regions. At 100% hydration (Fig. 4.2.3d) all cement is consumed, but the shape of the original grains could be distinguished if the inner products differ from the columnar zone of the outer products.

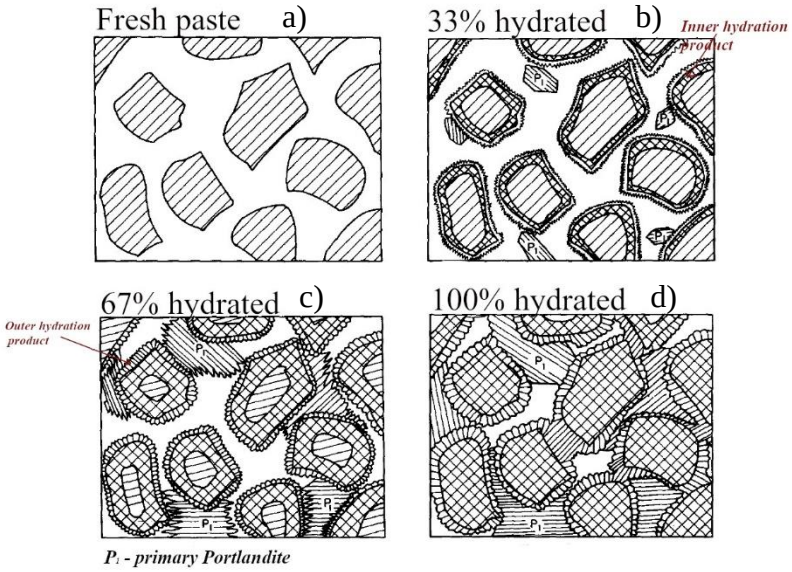

Figure 4.2.3 - Schematic representation of WPC hydration, adapted from [21].

Several models for the hydrated cement paste and C-S-H nanostructure have been developed.

One of the first models was done by Powers and Brownyard (P-B model) [20].

In this model cement paste is represented as a microporous solid (cement gel) randomly distributed in a network of capillary cavities that are orders of magnitude larger than the gel pores. The model is shown graphically in Figure 4.2.4.

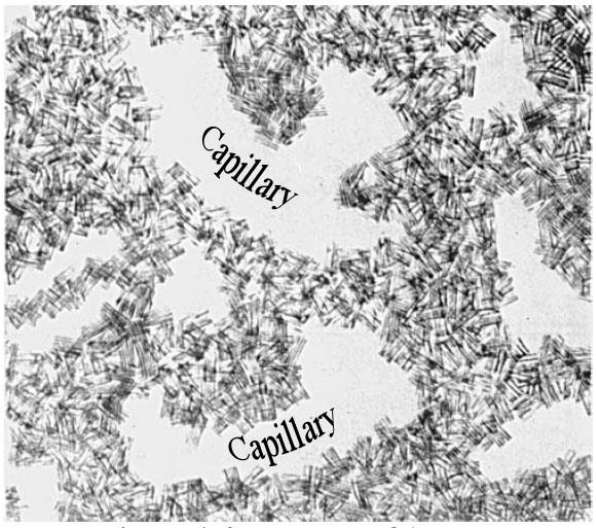

Figure 4.2.4 - Simplified model of the cement paste structure, adapted from [20].

Gel particles are represented as needles. Portlandite, un-hydrated cement and other hydration products are not represented. By this model, the densest possible fully hydrated cement paste has a porosity of about 26% with an average size of gel pores of 1.8 nm. It is

stated by the Powers and Brownyard that gel can be produced only in water-filled capillary cavities and when all cavities become full, no further hydration of the cement can occur. The "outward" and "inward growth" of gel particles were introduced by the model, and the gel particles formed by these two growth processes have different morphology and stoichiometry.

Another model is the Feldman-Sereda (F-S) model, which is more complex than P-B model. The F-S model is represented Graphically in Figure 4.2.5.

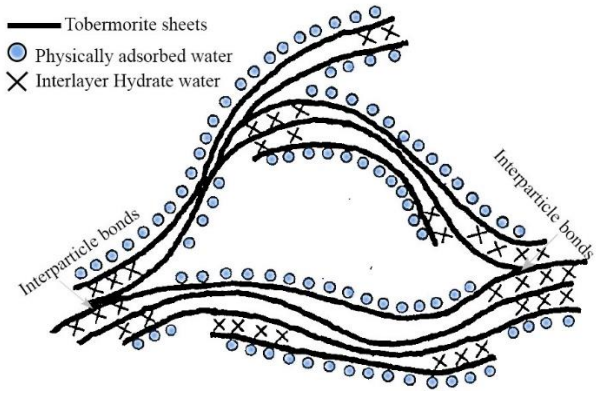

Figure 4.2.5 - Simplified F-S model for hydrated WPC, adapted from [18].

The model demonstrates the significance of the interlayer water. By the adsorption studies, it was concluded that tobermorite gel particles have layered structure into which water enters as "chemical" and structural component – interlayer-hydrate water.

4.3 Sorption processes

To investigate the sorption processes accurately it is essential to set universal terminology, sample preparation and experiments, which are reproducible.

Adsorption, a specific case of sorption, is a surface phenomenon that can be defined as the accumulation (adhesion) of a substance or material on a solid surface, creating a thin film of the adsorbate on the surface of the adsorbent [22]. Adsorption is the enrichment (positive adsorption, or briefly, adsorption) of one or more components in an interfacial layer [23]. Desorption is a reverse process, during which the substance is released from the surface.

Adsorption could be physical or chemical, but full separation of the two processes is not always possible. Physical adsorption is associated with the attachment of adsorbed molecules to the surface of the solid and is due to physical interactions, generally Van-der-Waals, but locally, the adsorption is chemical on the active sites (at which molecules are

adsorbed before taking part in the reaction) of the solid where chemical reactions could take place.

The energy of the reaction for physical adsorption is usually similar to that of condensation of the gas, although it may be considerably higher on active sites of the solid. The amount of gas or vapor adsorbed when equilibrium is established at a given temperature and pressure is a function of the nature of adsorbent and adsorbate. The experimental observation most frequently made for sorption systems is of the adsorption isotherm; this is the measurement of the quantity of adsorbed material as a function of its vapor pressure at constant temperature. For a given solid-gas system, this isotherm should be reversible if there is no irreversible change in the nature of the solid and/or gas, since there can be only one state of equilibrium at a given vapor pressure. At lower pressures this is usually the case, but at higher pressures the problem of primary hysteresis arises [18].

Speaking of classical description of sorption process, we are speaking about general system that consists of adsorption and desorption processes. Many uncertainness arises from the definition of the term sorption. Basically, in different literature we can see that authors use the term “sorption” for absorption and adsorption processes equally, not separating the two terms, and as well we see that even for cement authors use these two terms equally [24].

As it was said, clarification of the terms “absorption” and “adsorption” needs to be done. In some works, the term adsorption is used to describe the process of the liquid uptake, including both the adsorbed and the capillary condensed liquid. While some other authors, e.g., use “absorption” to describe exactly the same content, i.e., including both types of liquid uptake [25, 26].

In this work we would use the terms “sorption”, “desorption” to describe processes in general, including capillary absorption and “adsorption” to describe the effect of the surface water.

For the sorption measurement it is very important to carefully choose the reference dry state of the sample to be able to calculate water amount inside the cement specimen, as if not doing so, sorption curves could be changed dramatically and misinterpreted.

In our work we will define the dried reference state as a sample dried under vacuum, or submitted to the lowest RH achieved in the experiment.

In some works, authors carry out preparation of the samples (usually drying) as it might be necessary for the technique used or to start with the desorption curve [27]. But in this case one might measure the second drying cycle, as the first one already was run and, in many cases,

immediately at the first cycle irreversible changes in the structure are reported. Different drying techniques could cause alteration in the structure as well [28].

Cement samples need to be stored underwater for the preparation, so we can measure material in the "virgin" state [24].

Some difficulties arise from the difference in cement hardening time, which could vary from 28 days of hardening (as it has been reported that cement reaches its full strength on the 28^{th} day) to several years. It was reported that some processes are still taking place even after 28 days of hardening, and can influence the sorption isotherms. It was shown that hydration reactions tend to occur even after 28 days and towards much longer periods [27].

Pioneers of sorption investigation of cement are Powers and Brownyard [20]. They were the first authors to investigate reactions of water with cement powder, processes of hardened cement formation and made a model, which distinguishes phases of solid components and water filled porosity [29].

Typical adsorption isotherm for the cement gel, which represents pure C-S-H is shown in Figure 4.3.1. A lot of information could be gained from such experiments. Here, some findings from the work of Powers and Brownyard will be discussed. Their isotherm was obtained with the P-dried method (meaning that the samples are dried to "constant weight" in a sealed system charged with magnesium perchlorate [30]) of the cement samples and using water vapor. From this experiment they found that at RH below 45% the amount of water held is proportional to the amount of cement reacted and, hence, the amount of gel formed. Above 45% RH water condenses in capillary pores. With BET theory the quantity of water V_m necessary to cover the hydrated cement with one monolayer was measured. The first layer was obtained at RH of 20% and they obtained that V_m is linearly proportional to the amount of evaporable water. Powers and Brownyard concluded that depending on the cement composition the amount of internal surface differs.

The gel isotherm in Figure 4.3.1 shows the relation of w_g/V_m (w_g – mass of gel water) as a function of the RH. For RH of 0% and 100% w_g/V_m is 0 and 4 respectively, which corresponds to 0 and 2 mol of gel water retained. Inside this range, gel space is not completely filled with water anymore.

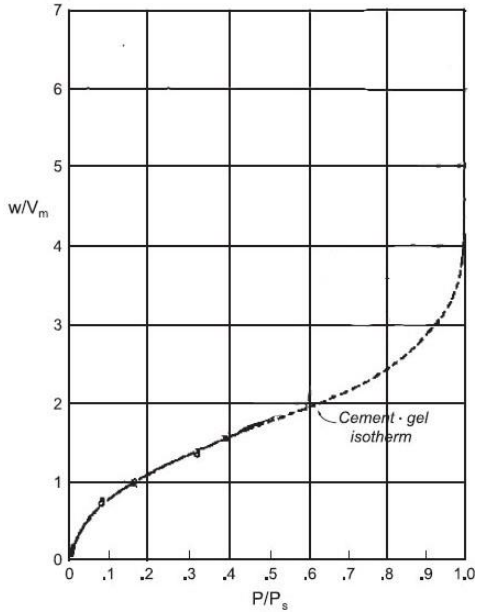

Figure 4.3.1 - Typical adsorption isotherm of the cement sample, adapted from [20].

4.3.1 Experimental methods

In the literature we can find many different research done on the adsorption-desorption process on the cement materials, with different experimental procedures, such as flow division method that mixes dry and saturated air, method consisting of altering temperature or pressure or both, volumetric method that isothermally changes the vapor pressure in a vacuum system, and gravimetric methods.

For many experiments, the model used to fit the data in sorption experiments is based on BET equations [31], which on one hand could show very good results, but need to be carefully adjusted with the change of every property of the cement [32].

The most popular method of sorption investigation is the “dynamic vapor sorption”. This method shows water content of the sample against the RH of the environment (considering the internal RH of the sample equal to the external one). From such experiments one can determine many important properties, such as porosity and its connectivity, specific surface area, and transport processes.

The determination of surface area by adsorption of N_2 has become a standard method in the realm of surface chemistry. But it was pointed out that for cement studies large difference in the specific surface area and pore size distribution exists between experiments made by water vapor and nitrogen.

In the case of hydrated PC, the "water area" has been the one generally considered "true and valid". It was considered that the N_2 molecule could not enter small pores and adsorb on the whole surface because of molecules large size. The diameters of the water, nitrogen, and methanol molecules are approximately 2.7, 3.64 and 3.6 Å respectively; but it seems unrealistic for the situation where up to 90 % of the area is excluded to N_2 because of the small difference in the molecule's sizes. If the holes were part of the crystal structure like certain "molecular sieves" which are cage-like molecules with small entrances, it would be realistic, but hydrated cement is not of this nature [18]. It was stated as well that nitrogen cannot penetrate many large pores [33] due to the ink bottle effect.

The same observation was made by Kalousek [34], who found that surface area measured by nitrogen and water vapor sorption is different. He explained it by the inability, unlike water, of nitrogen to penetrate between the layers of the calcium silicate hydrate. Brunauer et al. [35] used the same explanation on account of tobermorite. Later on, Brunauer et al in their later work [36] found that the same explanation (inability to penetrate between layers) for tobermorite is not fully valid. The density experiments showed that tobermorite dried to an H_2O/SiO_2 ratio of approximately 1.0 did not swell in a saturated $Ca(OH)_2$ solution, but showed a slow swelling with less dried tobermorite. Prior to surface area determinations, tobermorite is dried to this water content. In the work [36] the maximum RH used in the surface area determinations was 33%; it seems, therefore, very unlikely that water vapor entered between the layers in the adsorption experiments. Though, in some other experiments, a great discrepancy between water and nitrogen surface area is observed. It seems that the rolling of the sheets of tobermorite or aggregation of the crystallites or both together produces surfaces inaccessible to nitrogen molecules, though accessible to water molecules [36].

Some articles [37] state that the theory of different molecular sizes is wrong because even cement with a great proportion of larger pores still are not completely filled with N_2. Brunauer et al. [36] proposed that due to the small dipole moments as compared to water, experiments with N_2 show smaller porosity and surface area. In some works, the discrepancy is explained by the inability of N_2 to fill large pores due to capillary condensation, even at relative pressures close to 1.00 [37].

It was pointed out as well that the difference in the surface area and porosity for the two methods increases with the decrease of the w\c ratio. For smaller w\c ratio, it was concluded that pore size distribution displays a greater number of small pores as it is shown in Figure 4.3.2 [38]. Though it should be noted that in that research nitrogen adsorption is used and only the pores accessible to nitrogen are represented, which is about 40% of the total pore system

for the 0.35 w/c ratio paste, and about 50% for the other two pastes (0.5 and 0.7 w/c ratio) as stated in the research.

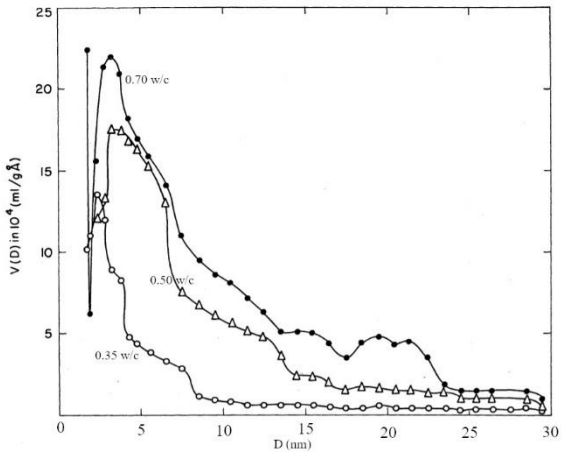

Figure 4.3.2 - Pore size distribution curves of hardened PC pastes, adapted from [38].

Another reason for using water vapor in studying cement-based materials is that unlike for experiments with nitrogen, pre-drying of the samples could be avoided, as it was stated that drying could cause alteration of the hardened cement structure.

A relatively easy method is to use salt solutions to achieve precise RH levels, for drying and wetting. This procedure belongs to gravimetric methods [39]. But, to estimate the amount of water, porosity and structural changes, one can use different experimental techniques. Very powerful and advanced techniques to use for such measurements is NMR or Magnetic Resonance Imaging (MRI). These non-destructive and non-invasive techniques allow one to run experiments *in situ* and to estimate not only water content but water populations and solid phases.

4.3.2 Hysteresis in cementation material. Pore-space structure

IUPAC classification of sorption isotherms is derived from porous classification of materials. So, in Figure 4.3.3 six types of sorption isotherms characterizing different porous absorbents are shown. Hysteresis takes place at types IV and V of Figure 4.3.3a, which are denoted as mesoporous materials.

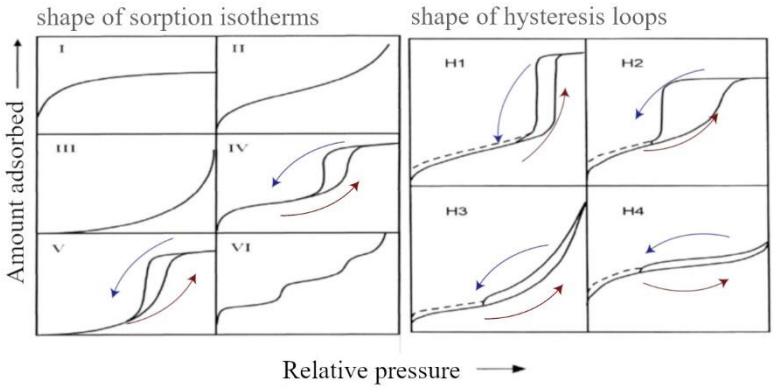

Figure 4.3.3 - IUPAC classification of sorption isotherms for different materials.

It should be said as well that the shape of sorption isotherms and hysteresis loop can correlate with different distribution of pore sizes and pore connectivity.

Figure 4.3.3 b shows the IUPAC classification of hysteresis loops. According to this classification, type H1 is often associated with porous materials consisting of well-defined cylindrical-like pore channels or agglomerates of approximately uniform spheres. Type H2 corresponds to materials that are often disordered, where the distribution of pore size and shape is not well defined and also indicative of bottleneck constrictions. Materials that give rise to H3 hysteresis have slit-shaped pores (the isotherms revealing type H3 do not show any limiting adsorption at high P/Po, which is observed with non-rigid aggregates of plate-like particles). The desorption curve of H3 hysteresis contains a slope associated with so-called tensile strength effect (this phenomenon occurs perhaps for nitrogen at 77 K in the relative pressure range from 0.4 to 0.45). Type H4 hysteresis is also often associated with narrow slit pores.

The dashed curves in the hysteresis loops shown in Figure 4.3.3 reflect low-pressure hysteresis, which may be associated with the change in volume of the adsorbent, for example, the swelling of non-rigid pores or the irreversible uptake of molecules in pores of about the same width as that of the adsorptive molecule [40].

Based on test results of nitrogen adsorption, the shape of the hysteresis loop obtained on cement pastes was of the H3 type according to the IUPAC classification [41].

So, it is evident that hysteresis loop for sorption cycles in cement materials is a usual phenomenon even for the low RH levels [42]. And as can be seen in Figure 4.3.4 [18], the hysteresis loop is evident for all the RH scales (5-100%). And from that figure one sees that the isotherm is irreversible at any point in the range of 5 to 100 % and probably lower.

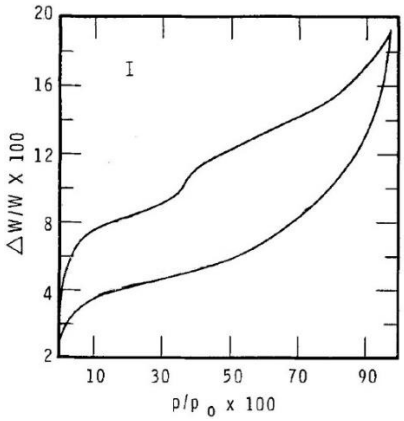

Figure 4.3.4 - Sorption of water on hydrated PC, scanning loop, adapted from [18].

There is not a clear picture of the explanation of the hysteresis and irreversible changes of the cement structure during sorption cycles, despite a lot of experimental and theoretical works that exist on the topic. In the literature, the most documented process that governs hysteresis occurring during sorption is the action of the capillary forces.

Capillary forces

The phenomena that regulate the hysteresis that occurs during absorption most documented in the literature are the capillary forces. Hysteresis is explained by strong capillary forces, especially for solids with mesopores (2 nm < d < 50 nm) [43]. For pores of such size during water sorption, menisci form in pores and create capillary stresses that are extremely strong and cause shrinkage of the porous material.

In cement samples capillary pores usually are emptying at 85%, but Powers and Brownyard [20], with the use of the P-dried samples in sorption experiments with water vapor, found that at a RH below 45%, the amount of water held is proportional to the amount of cement reacted and, hence, the amount of gel formed. Above this RH, the water condenses also in the larger capillary pores [29].

Capillary forces are supposed to act in the high RH range (down to approximately 50% RH for drying curve), since capillary stress fails to explain shrinkage deformations at low RH (according to Kelvin equation the maximum hydrostatic stress is reached in the range 40 to 50% RH) [44]. But, as some results obtained in different experiments are not in good agreement, we suppose that there should be other processes responsible for hysteresis in sorption experiments of cement samples.

Actually, in some investigations observed hysteresis is less significant below 40% RH. Some other results declare this observation not compulsory true for all cements, but more likely depending on pore distribution in the cement body [45].

In Figure 4.3.5 it is shown that for the cement with less amount of small pores hysteresis is rather almost not completely present for low RH, though cement with larger amount of micropores and small mesopores has pronounced hysteresis through all the RH range. This hysteresis is also reflected in the values of the volume change of the solid skeleton [29, 45].

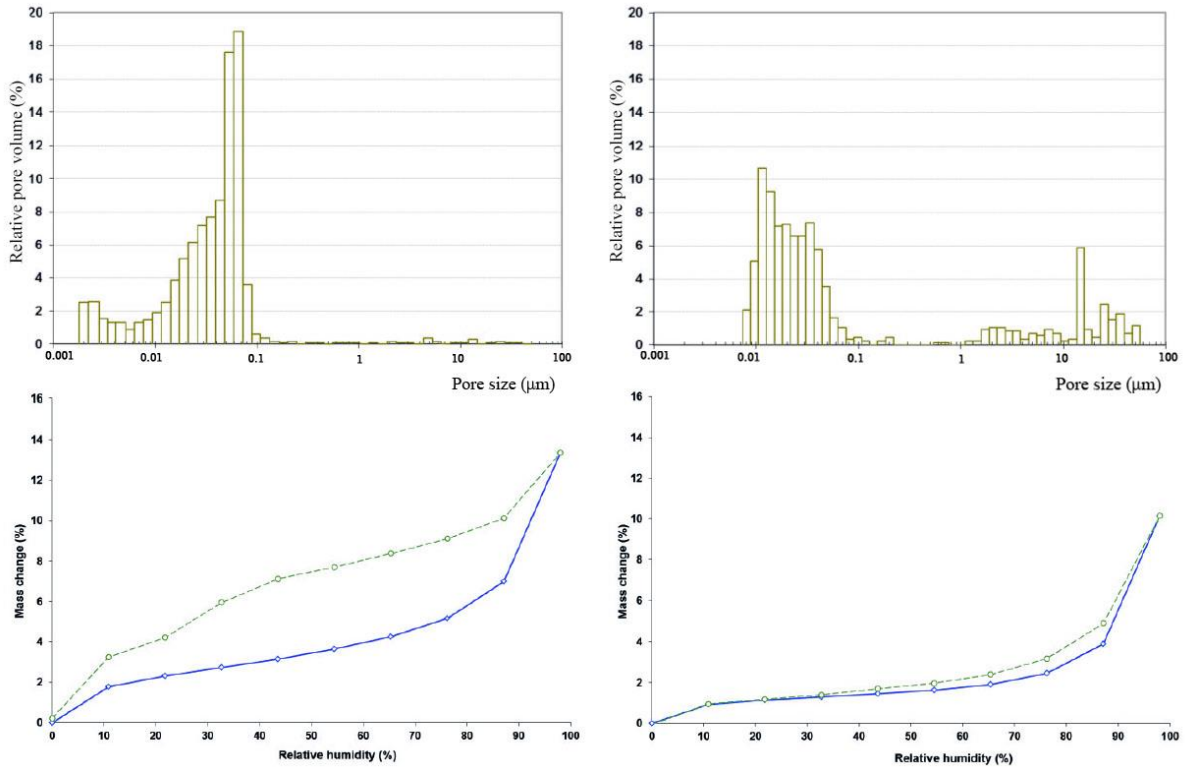

Figure 4.3.5 - Pore size distributions obtained from mercury intrusion porosimetry (MIP) (upper diagrams) and corresponding water sorption isotherms (lower diagrams) of PC pastes. The material with a large amount of micropores and small mesopores (a), material with a low fraction of small pores b), adapted from [29].

Papadakis et al. proposed that hysteresis was due to the extremely slow hygrothermal equilibrium rate, which implies that actual equilibrium curve state is in between those obtained by adsorption and desorption [46].

Ink-bottle effect

Some other authors, such as J.W. McBain or C.G. Vayenas, proposed the ink-bottle effect, due to which initial and completed filling of the pores correspond to different RH. So, depending on the RH level and the size of the throats of pores, the sorption curve representing

the amount of liquid retained during desaturation will lie above that for progressive saturation and this hysteresis will be due to the ink-bottle effect [46, 47].

Z. P. Bazant proposed to observe the dependence of sample mass W on RH as a function of pores geometry. The irreversible changes are explained by the fact that in a pore of a given geometry the surface menisci of capillary water may take various equilibrium forms ("bottle neck" effect and "open-pore" effect).

Such possibility is illustrated in Figure 4.3.6 a, b, another possibility is displayed in Figure 4.3.6 c, showing that at $h = 1$ and $P_a = 0$ (where P_a is theoretical pressure in the hindered layer and h is the humidity or relative vapor pressure inside the pore) the pores need not be full of liquid water, but a surface with opposite curvatures, $r_1 = - r_2$ (r_1, r_2 = principal curvature radii of capillary menisci), can exist in equilibrium. Irreversibility below $h = 0.45$ may be explained by closure of the thinnest gaps on drying (formation of a chemical bond), preventing re-entry of adsorbed films or by a similar effect for the evaporable interlayer hydrate which is chemically bound [48].

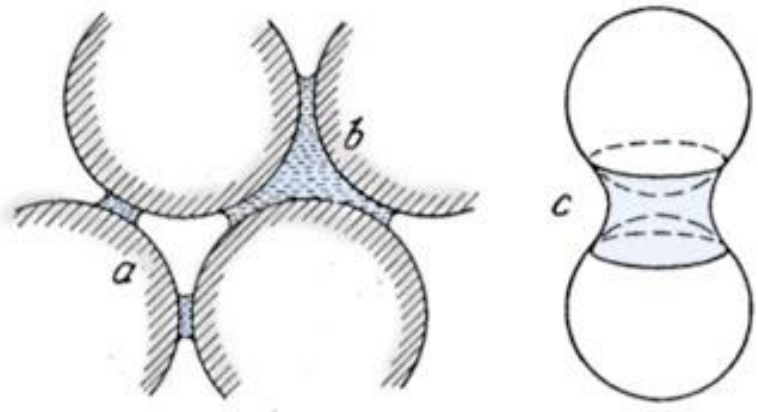

Figure 4.3.6 - Example of different equilibrium shapes of capillary menisci (a, b for same humidity; c for h=1), adapted from [48].

Nanoporous structure and disjoining pressure

In many previously done experiments, sorption hysteresis theory in PC has generally been interpreted under the hypothesis of some sort of changes of the nanopore structure. In nanoporous solids most of the adsorbate is in the form of hindered adsorption layers, i.e., layers confined in the nanopores (which are sometimes defined as pores ≤ 2nm wide). These layers have no surface directly exposed to vapor and communicate with the vapor in macropores by diffusion along with the layer. It is well known that large transverse stress, called the disjoining pressure (or solvation pressure), must develop in these layers [49]. In particular, it was

proposed that the exit or ingress of water, called the interlayer water, from or into the narrowest nanopores would somehow cause large relative changes in pore widths.

This mechanism was proposed in the 60's by Powers [50] in order to explain the continued shrinkage below 40% RH and has been recently recognized to be the dominant mechanism behind hygral expansion above 50% RH, since the pore solution at the nano-scale cannot form a capillary meniscus [51].

But this theory of hindered adsorption is also reversible. Thus, the theory is not sufficient to explain the hysteresis.

Interlayer spaces

From the F-S [18] model, gel pores and interlayer spaces could be distinguished. Different studies suggest that water in interlayer spaces does not evaporate till 20-25% RH. With lowering RH to 0%, as the adsorbed layer on the particles is removed, the particles are brought in close contact together. In the work by Feldman and Sereda, the authors propose the existence of irreversibility of the sorption curve on interlayer spaces, as if water is removed from interlayer spaces, it does not re-entry during re-saturation. This conclusion is not completely supported by the NMR data in the work done by Gajewics et al. [52] and in this study as well. In the study [53], it is suggested that a new interlayer space is created when adjacent particles are brought together by drying.

Interlayer spaces undergo substantial collapse and swelling as water is removed and reinserted, respectively. In other words, the insertion of water into the interlayer space confers a mechanical disjoining effect. The disjoining pressure mechanism can operate in parallel with capillary stresses.

Surface area

In the work by Thomas et al. [53] it was stated that the total surface area is decreased to the maximum of 18% after a drying and re-saturation procedure. The authors attributed this effect to the loss of surface area at particles contact, as adjusted particles are brought together. But, as it was said earlier, NMR data could not support this theory as the re-establishing of interlayer spaces was also observed in previously done works [52, 53].

In the work done by Aono et al. [54], authors found significant decrease of the surface area measured both by N_2 adsorption and water vapor sorption. They stated that surface area, obtained by the model at a monolayer adsorption state decreased slightly, but the surface area by the multilayer adsorption state decreased significantly. Authors connect these changes with

structural densification, due to the particles being drawn together. But, as well from the ^{29}Si NMR Q_2 [54] measurements authors found that decrease of the surface area could be associated with polymerization of the silicate anions.

On the contrary, in the study by Person and Allen [55], done with small-angle neutron scattering (SANS), it is noticed the surface area and the C-S-H gel structure can be fully recovered upon the rewetting of a D-dried (vacuum drying at 105˚C usually for 12 hours) specimen.

In the work done by Maruyama et al., it was shown that by the N_2 measurements, the surface area from desorption curve is much higher than from the adsorption process. As the water adsorption sites are considered to lie mainly in interlayer spaces of C-S-H, it was proposed that generation of new interlayer space is expected to occur at the higher RH, which could be the "destabilization" process [56].

Solid phases

As it was said, Aono et al., observed the polymerization of the C-S-H chains while drying the PC samples at 50˚C [54]. Bentur et al. observed polymerization in pure calcium silicate paste during the drying process [57]. Cong and Kirkpatrick used NMR to observe the polymerization of silicate chains in C–S–H. The polymerization did not occur during drying at room temperature, whereas it did occur at elevated temperatures [58].

In the study done by Maruyama et al. it was found by the use of ^{29}Si MAS NMR a decrease in the amount of Al, which was attributed to ettringite, till ≈40 RH, and an increase as the cement was dried to lower RHs. This was confirmed by the ^{27}Al MAS NMR results. Consequently, the mean chain length of C–S–H was increased by drying. The Al atoms probably migrate into the C–S–H interlayers during drying [59].

4.4 ^{1}H NMR technique

In the previous chapter the experimental technique and methods for the sorption study were discussed. As this work focus on the NMR as an experimental tool for the cement investigation, in this chapter the theoretical background of the technique will be explained in more details.

NMR technique could be divided into three large sections: MRI, Spectroscopy and Relaxometry NMR. In this work we only discuss about methods that fall under Relaxometry technique. The general theory, described in this Chapter follows that is reported in the books

“Nuclear Magnetic Resonance and Relaxation” by Brain Cowan [60] and Spin Dynamics: Basics of Nuclear Magnetic Resonance by Malcolm H. Levitt [62].

For a deeper understanding of NMR method also the book Pulse and Fourier Transform NMR Introduction to Theory and Methods by Thomas C. Farrar and Edwin D. Becker [61] is suggested.

4.4.1 Introduction to NMR

NMR represents a number of powerful techniques, used to study the structure and dynamics of molecules. We can use NMR to indicate a physical phenomenon and indicate a suite of techniques that uses spin of the nuclei as a probe. Strictly speaking, NMR is one of the wide range of phenomena, associated with the interaction of electromagnetic radiation with matter, precisely with nucleus of atoms.

In NMR quantum mechanics theory, the energy levels are associated with the different orientations of the nuclear magnetic moments of an atom in an applied magnetic field [60].

The very first experimental attempt on bulk material was performed by C.J. Gorter in 1936, but it failed due to the use of an unfavourable substance.

Y.K. Zavoisky in 1941 observed resonance in bulk substances but dismissed the results as not reproducible. He is recognized as the discoverer of electron paramagnetic resonance in 1944.

For the first time, the successful observation of these phenomena in the condensed matter are usually attributed to two independent teams by Bloch etc, and Purcell etc, in Stanford and Harvard Universities, respectively in 1946. We should mention here Rabi and co-workers, who in 1938, using a beam of silver atoms, observed the change in the fluxes of beams representing the different energy states of nuclear magnetic moments.

The main differences in these observations were that Bloch observed NMR phenomena in a bulk matter and not in a beam of non-interacting atoms and that, the transitions are through the energy absorbed from the radio-frequency (RF) fields.

Bloch in his works showed that NMR could be observed in several ways. The slow passage experiments, which consists of slowly sweeping RF field in a fixed magnetic field or vice versa. Another way is an adiabatic rapid passage with the sweeping rate of the field RF or external in a specific limit. These methods are usually referred to as continuous wave (cw) techniques.

A third method is called pulse or free precession method. In this method to observe the NMR signal the short burst of RF pulses is used. The signal is produced after the RF is turned off [61].

In order to understand how NMR phenomena are produced, we should firstly speak about nuclei and the concept of spin.

4.4.1.1 Basics of NMR phenomena

Firstly, the difference between NMR Spectroscopy and NMR Relaxometry should be addressed. While both these techniques observe spin of the nuclei over time, Spectroscopy is a technique typically used in chemistry, it gives information of chemical composition and structure of the measured sample by exploration of the chemical shift of the observed nuclei, where Relaxometry deals with physical-chemical bulk properties of a sample, including molecular dynamics of fluids both in bulk and confined by surfaces. In Spectroscopy, chemical shift resolution often relies on a high-field superconducting magnet, while Relaxometry measurements could be performed with the use of low-filed permanent magnets, with relatively inhomogeneous fields.

If NMR Spectroscopy needs strict quantum mechanical explanation, most of the Relaxometry experiments could be explained by the classical vectoral approach. In this work both ways: classical and quantum are addressed.

4.4.1.2 Spin system. Quantum explanation

The concept of a spin cannot be explained by the classic equation of motion, so some quantum mechanical explanation is needed.

Atomic nucleus has an important property called spin. The concept of a spin is highly abstract, but nevertheless, we should try to “grasp” it.

This quantum property arises from the quantum angular momentum that could be thought to be similar to classical angular momentum (or rotational momentum).

Classical angular momentum could be visualized by the “right hand rule”, illustrated in Figure 4.4.1. Classical angular momentum is a vector quantity. Imagine the rotating wheel and the axes of rotation as a pole through the centre of a wheel. If using a right hand with the thumb pointing along the rotation axis, wrapped fingers will be in the direction of the rotation [62].

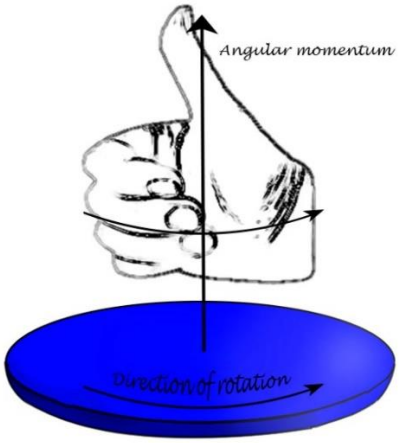

Figure 4.4.1 - Right-hand rule.

The equation for the module of the angular momentum in classic mechanic is

$$L = I\omega, \tag{4.4.1}$$

where ω is the angular velocity and I is the moment of inertia.

And module of the angular momentum of a particle about the point O is

$$L = rp, \tag{4.4.2}$$

where r is the position vector of the particle with respect to O and p is its linear momentum.

As it is implied by the name, in quantum theory the angular momentum is quantized. In 1913 Bohr introduced the postulate that the angular momentum of a system was quantized, i.e., that it could only take values which were integer multiples of a quantum of action h times $1/2\pi$:

$$Angular\ mometum\ quantum = \hbar = \frac{h}{2\pi} \approx 1.0546 \times 10^{-34}(\text{Js}), \tag{4.4.3}$$

where $\hbar$ is the reduced Plank constant. A measured vector component of angular momentum gives either half-integer or integer multiple of $\hbar$.

Later on, it was suggested that the direction of orientation of angular momentum is quantized, meaning it could take only certain directions with respect to a fixed axis [63].

In the quantum theory a total angular momentum is equal to

$$L_{tol} = [J(J+1)]^{1/2}\hbar, \tag{4.4.4}$$

where J takes integer values $J = 0, 1, 2, \ldots$.

And the total angular momentum quantum number parameterizes the total angular momentum of a given particle, by combining its orbital angular momentum and its intrinsic angular momentum (i.e., its spin).

As the rotational energy is proportional to the square of the total angular momentum, the energy is also quantized. For the rigid molecule, the energies of the stable rotational states are

$$E_j = BJ(J+1), \qquad (4.4.5)$$

where *B* is a rotational constant of the molecule.

The direction of the rotation is described by the secondary total angular momentum quantum number M_J, which takes one of the 2*J*+1 integer values M_J = -*J*, -*J*+*1* ... +*J*.

Without external magnetic field, 2*J+1* states are degenerate, have the same *J* value, but different M_J value, meaning they have the same energy [62].

If an external magnetic field is applied, the degeneracy is broken and each of 2*J+1* sublevels have different energy. Such effect is called Zeeman effect. The energy separation is called Zeeman splitting [62].

As it was said, intrinsic angular momentum of the particle, spin, is a part of the total angular momentum.

In the case of spin of the particle, total angular momentum is $[S(S+1)]^{1/2}\hbar$. Spin sublevels (2*S+1*) will have different energy in the presence of external magnetic field, while are degenerate without external magnetic field [62].

Different particles have different quantum value of the spin. Particles with integer spin value 0,1,2… are called bosons. Particles with half integer spin, 1/2, 3/2, 5/2 … are called fermions.

Spin is a completely intrinsic phenomena of the particle. Rotational angular momentum of the molecule can vary due to collisions, on the contrary spin is a feature of the particle's 'nature'. Particles at absolute zero will not have a rotational angular motion, but particles will always have the same spin.

As it is known, atomic nuclei consist of neutrons and protons and is specified by the atomic number, the mass number and spin quantum number.

The nuclei having the same atomic number but different atomic mass are called isotopes. Here are some stable isotopes:

^{1}H = p $\qquad$ ^{12}C=6p+6n

^{2}H = p+n $\qquad$ ^{13}C=6p+7n

Most atomic nuclei possess spin, denoted by the spin quantum number *I*. The main hydrogen isotope ^{1}H has only one proton, meaning its quantum spin number *I=1/2*. Spins of other nuclei are formed by the combination of the proton's and neutron's spins.

Just as with the ordinary angular moments, if the magnetic field is applied, the (*2I*+1) energy degeneracy levels are broken. The splitting between the energy levels is called the nuclear Zeeman splitting and is represented at Figure 4.4.2.

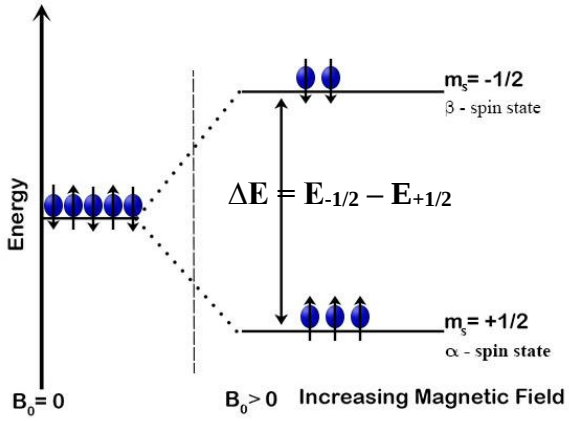

Figure 4.4.2 - Zeeman effect.

NMR is the spectroscopy of the nuclear Zeeman sublevels. If the spin number =1/2, the energy state is split in two. In case of other spin numbers, it could be split in more levels. In this study we are focusing on the spin of ^{1}H hydrogen isotope and for simplicity later on we will use "proton" as a synonym for ^{1}H nuclei.

But as it was already said, explanation of most NMR Relaxation experiments could be done without the use of quantum theory.

4.4.1.3 Magnetic field

For many NMR experiments one can describe spins behaviour in an external magnetic field by using classical mechanics and operating with vectors, where the vector B_0 represents external magnetic field which interacts with the magnetic moments.

Energy of the magnetic moment can be written as a scalar product of two vectors:

$$E = -\mu_Z B_0, \tag{4.4.6}$$

where subscript z in μ_Z means that spins are aligned along the field direction z, and μ_Z is the z-component of μ, B_0 is the strength of the magnetic field (magnetic flux density) and negative sign indicate that the energy is lower, when the magnetic moment is parallel to the magnetic field, as displayed in Figure 4.4.3.

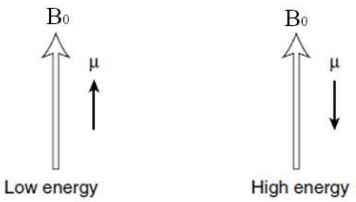

Figure 4.4.3 - Magnetic energy.

The magnetic moment of the nucleus is connected to the spin as:

$$\mu = \hbar I \gamma \tag{4.4.7}$$

Where γ is the gyromagnetic ratio of the nucleus and differs for different nuclei [60].

Combining equations 4.4.6 and 4.4.7 we can write

$$E = -m\hbar\gamma B_0 \tag{4.4.8}$$

So that, the nuclei energy is shifted proportionally to the magnetic field strength, gyromagnetic ratio and the z-component of the angular moment. Energy levels are spaced with a gap of $\hbar\gamma B_0$ [64].

If we consider adjacent states, the energy difference is given by

$$\Delta E = \hbar|\gamma|B_0 \tag{4.4.9}$$

$\Delta E = \hbar|\gamma|B$ And the resonance will occur, or in other words, transition will be induced, when the applied radiation has the angular frequency

$$\omega_0 = \gamma B_0 \tag{4.4.10}$$

So, from the vector point of view, what is happening to the nuclear spin in an external magnetic field? Angular momentum of a particle with a spin is also a vector, in some text the direction is called the spin polarization axis. Without external magnetic field, spin polarization axes point in different directions, as represented by Figure 4.4.4 (a). In the vectoral picture the spin is sketched as a magnetic needle. As we are working with hydrogen and gyromagnetic ratio has positive value, the vector of magnetic moment points in the same direction as the spin polarization. Now, let's suppose that an external magnetic field was applied, in this case spin vectors will align with the vector of the external magnetic field, as showed in Figure 4.4.4 (b).

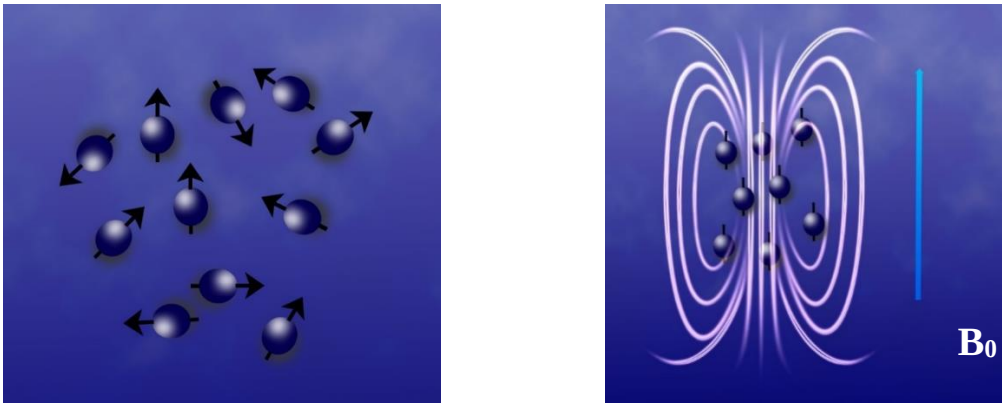

a) b)

Figure 4.4.4 - Spin orientation, a) without external magnetic field, b) in external magnetic field.

As nuclei have also an angular magnetic momentum, the spin polarization will act as a gyroscope, processing around an external magnetic field. The magnetic moment is moving with constant angle with the field. Such motion is called precession, represented in Figure 4.4.5. Here, the assemble of spins is aligned with the magnetic field B_0 and seen as a magnetisation vector M, which precesses around B_0.

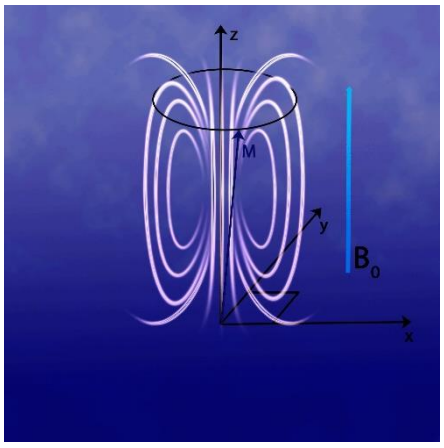

Figure 4.4.5 - Spin procession in an external magnetic field.

The frequency of this precession is called Larmor frequency

$$\omega_0 = -\gamma B_0 \tag{4.4.11}$$

The sign of a Larmor frequency indicates the sense of precession. As most nuclei have positive gyromagnetic ratio, the Larmor frequency will be negative, meaning that the precession is happening in clockwise direction. Larmor frequency is important as nuclei can absorb or emit energy only at their Larmor frequency and for the ^{1}H nuclei Larmor frequency is at 42.58 MHz for the field strength of 1 T [60].

4.4.2 NMR measurements

4.4.2.1 Relaxation time and its measurement in bulk

Again, let's consider ^{1}H nuclei in a sample of water and the vectoral picture. Without magnetic field, spin orientation is uniformly distributed. The total magnetisation is close to zero, as approximately the same amount of spins points toward all directions.

Water molecules, that carry spins, undergo constantly motion. The orientation of the molecules changes continuously. Though, spin assembly is still pointing in the same direction and the total magnetization still precesses around the external magnetic field, independently of the continuous molecular motion.

Such motion influences the field experienced by the nuclei. Each nucleus is a source of a microscopic magnetic field. These microscopic fields may arise from the interactions with orbital electrons and possible quadrupole interactions with crystal fields [60], and with the magnetic fields of the surrounding nuclei. These magnetic fields in have slight amplitude and direction fluctuations.

The wandering molecular motion is not completely isotropic. With slight probability spin will be oriented parallel to the magnetic field (lower magnetic energy). This thermal wandering motion is slightly biased towards spin orientations with magnetic moments parallel to the magnetic field B_0. This leads to a stable anisotropic distribution of nuclear spin polarization, called thermal equilibrium.

Magnetization distribution anisotropy in thermal equilibrium means that the entire specimen has a small net magnetization along the field B_0, which is called longitudinal component of the magnetisation, and this is the microscopic mechanism producing the nuclear paramagnetism. For protons in water, the contribution of the nuclei to the magnetic field is [62]:

$$\chi_{nuc} = \frac{\mu_0 \hbar^2 \gamma^2 c}{4 k_B T}, \tag{4.4.12}$$

where c is a protons number in a unit of volume.

This leads to

$$\chi_{nuc} = +4.04 \times 10^{-9} \tag{4.4.13}$$

Which is near three times smaller than observed diamagnetism of water [60]. So, in practise each spin sees a slightly different magnetic field and these fields may change with time.

To summaries, the relaxation processes observed in the dynamics of a spin system are due to the interactions of the spin dipoles with their environment and with themselves.

We already introduced the term longitudinal component of the magnetisation. Let's speak about it some more. In this case we are referring to the relaxation of the magnetisation component parallel to B_0. This process involves change of spin magnetisation energy density. Exchange of energy with other degrees of freedom plays role in this process, as the total energy must conserve. In NMR field, degrees of freedom are referred to as "lattice" and thus this process is called spin-lattice relaxation [60].

To further explain the process, imagine that the external magnetic field B_0 is suddenly turned on. The initial total nuclear magnetisation is zero, but gradually grows due to the spins biased orientation. The curve of the magnetisation grow is approximately exponential [62] with time constant T_1 (spin-lattice or longitudinal relaxation time).

On the other hand, we have also relaxation measured perpendicular to the field B_0.

Let's suppose that the spin system reached thermal equilibrium in a magnetic field. As described above the spin system consists of a large number of spins all processing around the magnetic field B_0 at an angle to the field. Component of the net magnetisation perpendicular to the field is absent. Now, suppose that the net magnetisation M_0 is suddenly rotated about the x-axis by $\pi/2$ radian (a short radiofrequency pulse, which will be described in detail later). Now, the net magnetisation will be in y-axis, perpendicular to the external field B_0, how it is illustrated by Figure 4.4.6.

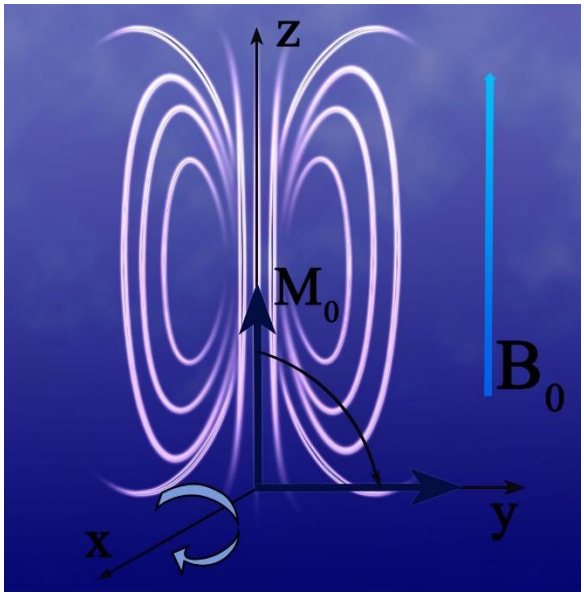

Figure 4.4.6 - Rotation of the net magnetisation around the x-axis.

After the rf pulse, this component of the magnetization tends to go to zero in the *xy* plane, so such relaxation is named – transverse relaxation process. Unlike in longitudinal relaxation process, there is no exchange of energy with surrounding, and transverse relaxation process might be called spin-spin relaxation time or T_2 relaxation time. As we already mentioned, the field B_0 is not homogeneous through the sample, and net magnetisation M_0 consists of all spins of the system, which are processing around z-axis with slightly different frequencies. As a result, the precession of the spins quickly becomes out of phase. Always we will have spread of values of the intensity of B_0 through the specimen.

These variety of the field cause spins to process at different Larmor frequencies. This motion incoherence leads to the dephasing and thus relaxation. As inhomogeneity of the field influences relaxation time, here we are essentially speaking about T_2*, which is shorter than the actual T_2 of the system. It is influenced by the inhomogeneity of the magnetic field, so that using different methods it is possible to reduce the magnetisation loss due to the inhomogeneity.

Other possible contribution to this relaxation process may arise from the solids with defined crystalline structure, as nuclei usually lie in certain lattice positions and are not free to move around. Hence, neglecting magnetic uniformity, due to the neighbouring nuclei in the sample, T_2 could be very short. But, in balk liquids, nuclei move fast enough so that the varying local magnetic fields are averaged so the only cause for transverse relaxation is the returning to the z-axes. Thus, in liquids T_2 is equal to T_1, and it is assumed that T_2 cannot be longer than T_1 [65]. It is worth to note that in specific cases, under particular circumstances not encountered in the systems investigated in this thesis, it is possible for T_2 to be longer than T_1 [62].

Through relaxation times and using phenomenological Bloch equations, we can quantify these processes. As we are introducing magnetisation through their vector forms, it is possible to write for the net magnetisation:

$$\dot{M} = \gamma M \times B_0, \tag{4.4.14}$$

where $\dot{M}$ is a total magnetic moment per unit volume, γ is the gyromagnetic ratio.

In phenomenological approach, adding relaxation term to the precession equation 4.4.14 [60],

$$\begin{cases} \dot{M}_x = \gamma |M \times B|_x - M_x/T_2 \\ \dot{M}_y = \gamma |M \times B|_y - M_y/T_2 \\ \dot{M}_z = \gamma |M \times B|_z + (M_0 - M_z)/T_1 \end{cases} \tag{4.4.15}$$

where M_0 is an equilibrium value of M_z. While M_x and M_y relax to zero, M_z relaxes to M_0. Relaxation described by these equations will follow an exponential law. For a constant filed B_0 in the direction z, solution to these equations is [60]:

$$\begin{cases} M_x(t) = M_x(0)\exp(-t/T_2) \\ M_z(t) = M_0 - [M_0 - M(0)]\exp(-t/T_1) \end{cases} \quad (4.4.16)$$

The evolution of the magnetisation can be measured giving rise to exponential functions represented in Figure 4.4.7(a) and 4.4.7(b) [60].

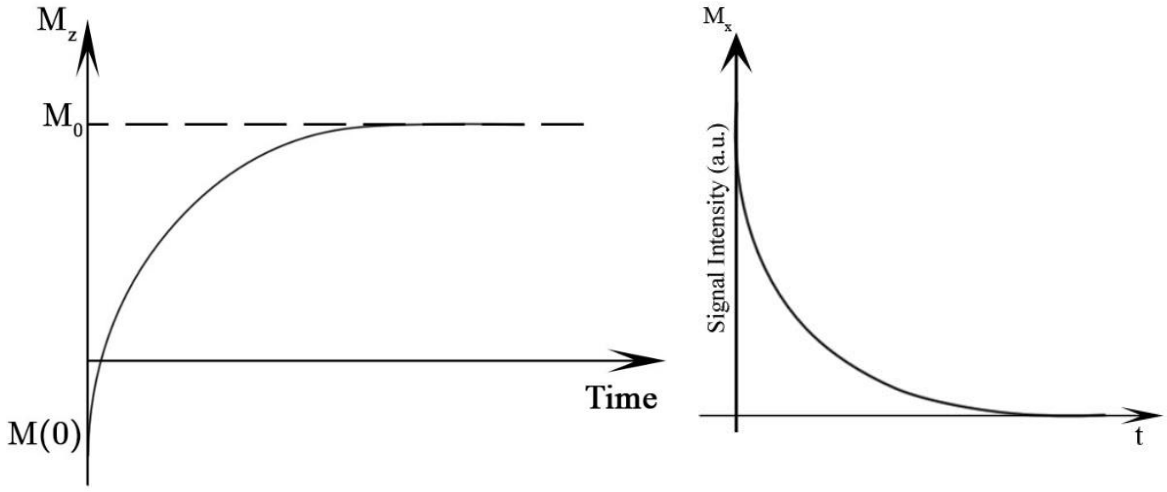

a) b)

Figure 4.4.7 - Magnetisation processes behaviour, a) longitudinal relaxation, b) transverse relaxation.

Here, in Figure 4.4.7, the graph presented in b) is a result of the measurements in the rotating reference frame, which is used to simplify the complex motion of processing spins.

With the rotating frame, we, as to say, looking at the system through eyes of a someone rotating, rather than stationary with respect to the system [60]. As the Larmor precession is always occurring, it is only natural thing to do. The precession of a magnetic moment is described by eq. 4.4.10 and observer, rotating at the same rate of ω_0 will observe a stationary magnetic moment, the effect of the field will be omitted. In a rotating reference frame, a static magnetic field may thus effectively disappear. Mathematically it is described as:

$$B_{eff} = B_0 + \omega/\gamma \quad (4.4.17)$$

In general, we see that in a rotating frame there appears an extra 'fictitious' magnetic field. It is usual to choose the frame rotating at the same rate as the applied transverse field. In this frame the effective field is then stationary [60].

4.4.2.2 FID signal as the simplest measurement

Usually, in a laboratory experiment, samples are placed in the glass tube or sample holder, which is positioned between the magnet poles and the rf coil is looped around the tube or sample holder in such a way, that the magnetic field B_1, created by the rf coil is perpendicular to the magnetic field B_0, created by the magnet.

The spins of a sample, placed in a magnetic field B_0, as it was mentioned previously, due to the angular momentum of the nuclei (property, that characterise the rotary inertia of a spin), form a magnetisation vector M, that acts as a gyroscope, processing around the external magnetic field (Fig. 4.4.5).

As a current pulse is applied through a coil with the frequency, equal to the Larmor frequency (so called "in resonance"), that generates the magnetic field B_1, this field cause the assemble of nuclei to tip through an angle θ. The duration of the pulse can be adjusted in such a way, that the magnetization M is tipped at specific angle.

With a certain pulse duration, the magnetisation M is tipped at 90˚ into the xy plane. After the pulse is turned off, the magnetisation M or spin assemble will process about the static magnetic field in the transverse xy plane. Usually, the 90˚ pulse is used to measure the relaxation of the signal, called Free Induction Decay (FID). The FID signal is largely influenced by the field inhomogeneity, paramagnetic impurities and T_2 and T_1 of the sample. The relaxation time of this decay is T_2^*. The signal normally decays exponentially with time as:

$$M(t) = M_0 \exp(^{-t}/_{T_2^*}) \tag{4.4.18}$$

The Fourier Transform (FT) of the FID signal will be a sharp peak at the Larmor frequency, if the FID is long, and a broad peak, if the FID is short, meaning heterogenous field distribution. FT will be explained briefly further.

We are working with NMR relaxation techniques, and usually we do not need to undergo the acquired signal to the FT, meaning that the main information drawn from the experiment are gained from the signal in time domain, not in the frequency domain. The mathematical transformation in the case of time domain NMR is usually an Inversion procedure, commonly referred as an Inverse Laplace Transform (ILT), which gives the distribution of relaxation times as will be explained briefly further.

It is worth to note that this mathematical operation usually is not applied on the FID signal, because the distribution of the T_2^*s in a sample does not give useful information.

It should be noted here, that as we are speaking mostly about low-filed Relaxometry technique, in this case the raw data from time-domain is analysed without Fourier transformation. Anyway, it is worth a short explaining of FT, because it is later mentioned in the text.

FT is a mathematical technique to convert the function of time into the function of frequency and vice-versa (inverse FT).

Mathematically FT could be defined as:

$$M(\Omega) = \int_0^\infty M(t) \exp\{-i\Omega t\}\, dt, \tag{4.4.19}$$

where $M(\Omega)$ is the NMR intensity at offset frequency Ω_0. Here, the input $M(t)$ is a function of time or time-domain signal and output $M(\Omega)$ is the spectrum or frequency domain signal.

The offset frequency Ω_0 is the frequency difference at which sample oscillates respect to the reference Larmor frequency and created by the detector, that combines the NMR signal ω_0 with the reference signal ω_{ref} [62]:

$$\Omega_0 = \omega_0 - \omega_{ref}, \tag{4.4.20}$$

The quadrature receiver is used for the signal frequency conversion by combining the signal at Larmour frequency with reference frequency.

The signal from the receiver is split as two outputs and receiver does not distinguish between these two output signals, collected from the axes *x* and *y*. These two signals are labelled as real and imaginary, which arises from the mathematics of the FT, as a time-domain and frequency-domain signals are complex functions, and are of the form:

$$\begin{aligned} M_A(t) &\sim \cos(\Omega_0 t) \exp\{-\lambda t\} \\ M_B(t) &\sim \sin(\Omega_0 t) \exp\{-\lambda t\}, \end{aligned} \tag{4.4.21}$$

where λ - damping factor with the rate constant T_2^{-1}.

Or it could be interpreted as real and imaginary parts of a single complex signal $M(t)$.

$$\begin{aligned} M_A(t) &= \mathrm{Re}\{M(t)\} \\ M_B(t) &= \mathrm{Im}\{M(t)\} \end{aligned} \tag{4.4.22}$$

So, the signal $M(t)$ could be shown as

$$M(t) = M_A(t) + iM_B(t) \sim \exp\{(i\Omega_0 - \lambda)t\} \tag{4.4.23}$$

Such output scheme is called quadrature detection [62].

4.4.2.3 Lineshape of NMR signal

The lineshape of the NMR signal in the presence of noise and its careful fit could give a lot of information on the measured samples, the area of each line is proportional to the number of spins, whereas the shape and its width give information on the relaxation process.

In high resolution NMR, the spectra are normally supposed to be a superposition of Lorentzian lineshape functions (Figure 4.4.9), which sometimes is considered to be a specific case of Voigt lineshape. In the time domain, the Lorentzian lineshape corresponds to the exponential decay of FID, with a time constant T_2*.

The presence of broadening effects leads to a Gaussian lineshape (Figure 4.4.9), which, for some solids, is a convenient lineshape approximation.

The convolution of two broadening effects, such as random broadening in the Gaussian lineshape and broadening due to imperfect shinning and susceptibility variations, will lead to a Voigt lineshape, which is a conjunction of the Gaussian and Lorentzian lineshapes (Figure 4.4.9) [66].

These lineshapes are shown in Figure 4.4.8 for different values of the Voigt parameter $a = {W_L}/{W_G}$, where W_L and W_G are the full width at half maximum height for Lorentzian and Gaussian lineshapes, respectively.

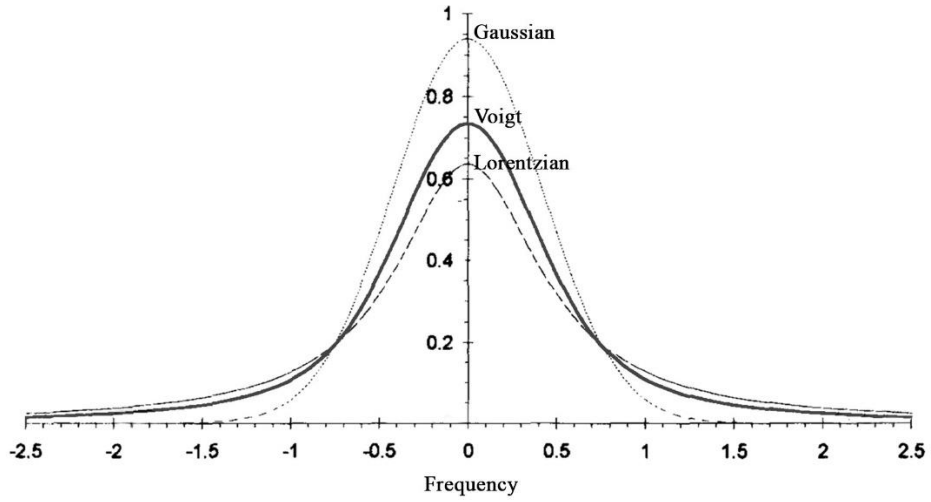

Figure 4.4.8 - Voigt lineshape with different values of a parameter, adapted from [66].

4.4.2.4 T_2 measurements

Previously FID measurements of T_2* were explained, but in order to observe the real T_2 of the sample, an intrinsic relaxation time, a technique that reduce the influence of the filed

inhomogeneity should be used. Such technique is an implementation of a special sequence (train of pulses), called Carr-Purcel-Meiboom-Gill (CPMG), described later.

Consider that that at time *t=0* the 90˚ pulse is applied, spins are tipped from the z direction into the transverse plane. The local fields near the spin will contribute to the dephasing and loss of the precessing magnetization, as some spins precesses faster and some other slower.

If a 180˚ pulse is applied at some time after the initial 90˚ pulse, the motion of the spins will go reverse. Spins that initially precessed faster now will travel in opposite direction with faster rate and spins with slower rate now will travel backwards at slower rate. After some time, spin precession will again be in phase forming an echo signal. The vectoral representation of a spin (Hahn) echo is shown in Figure 4.4.10. The result of such rotation is to transform magnetization vectors as:

$$\begin{cases} M_x \rightarrow M_x \\ M_y \rightarrow -M_y \\ M_z \rightarrow -M_z \end{cases} \tag{4.4.24}$$

If the initial magnetization was created with a 90˚ pulse along *y* axis then M_0 is imaginary and the echo is along *-y* axes, if the magnetization was created along *x* axis, M_0 is real [60].

The growing echo graphically could be seen as an opposite of an FID and the dephasing is similar to the initial relaxation after 90˚ pulse. Generally speaking, the shape of the spin echo is like two back-to-back FIDs as it is demonstrated in Figure 4.4.9.

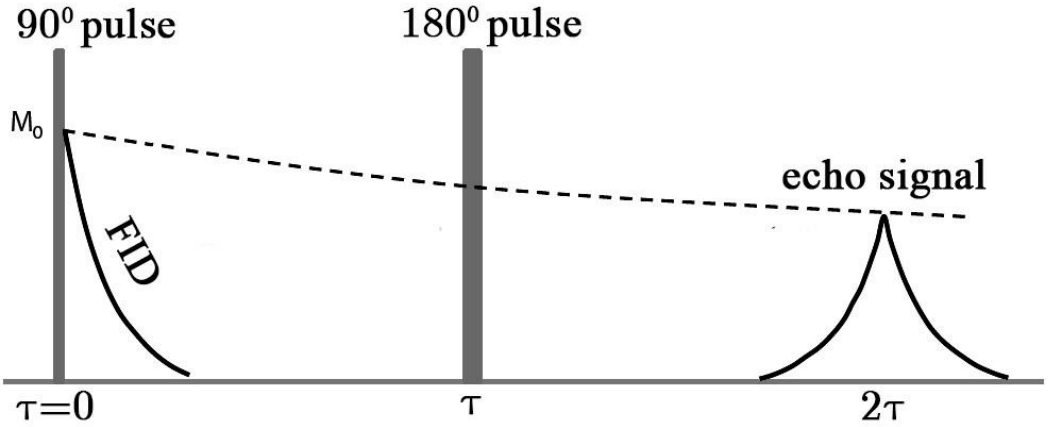

Figure 4.4.9 - Schematic of the spin (Hahn) echo, adapted [67].

T_2 could be found from the echo height in *90˚-t-180˚-t-echo* sequence by repeated measurements at different echo times:

$$M(2t) = \exp(^{-2t}/_{T_2}) \quad (4.4.25)$$

From such sequence, only a single data point will be measured, but in order to correctly determine the T_2 value a number of data points should be used by changing *t* value in *90˚-t-180˚-t-echo* sequence. It is necessary to wait in between pulse sequences for a time of the order of a few T_1 (usually 5*T_1) for M_z equilibrium reestablishment.

There is a less time-consuming solution, which was proposed by Carr and Purcel. They proposed a possibility to apply multiple 180˚ pulses to recover the magnetization again and again. If the 90˚ pulse was applied along the *x* axis, then *M*(*0*) would be pointing along y direction and will be imaginary, and echo will be pointing in the direction opposite to the initial magnetization.

To compensate for some errors of the echo due to the loss of transverse magnetization, Meiboom and Gill proposed to apply the 180˚ pulse with a phase perpendicular to the 90˚ pulse. In this case the initial magnetization is along x direction and all echoes point in the same direction. In this way there is no cumulative effect due to the error [60].

Resulting sequence is known as Carr-Purcell-Meiboom-Gill (CPMG), and its pulse sequence timing diagram could be written as $((\pi/2)_x - (\tau - (\pi)_y - \tau - echo\ acquisition -)_n$ and is shown in Figure 4.4.10.

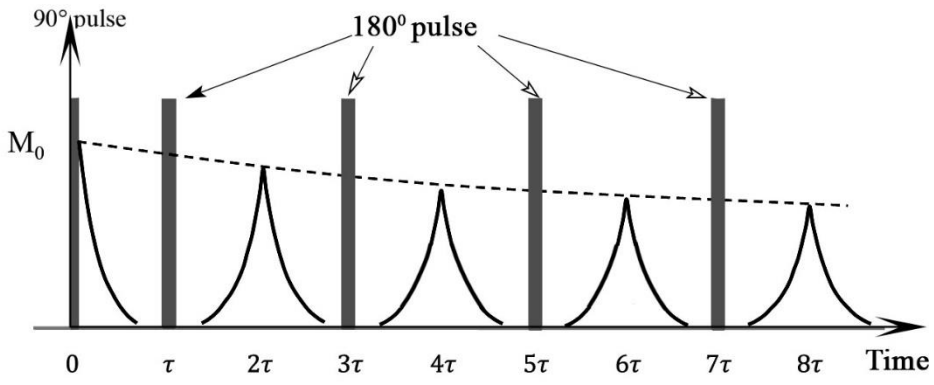

Figure 4.4.10 - Schematic representation of the CPMG sequence.

4.4.2.5 Measurements of T_1 relaxation time

As it was said, T_1 is the relaxation time of the longitudinal component of the magnetization. As it is not possible to measure T_1 directly, one needs to use 180˚ pulse to align magnetization along the *-z* axis, which we denote as *M*(0) and after some recovery time τ, 90˚ pulse to monitor in the x-y plane the amount of recovered magnetization along *z*-axis. The

intensity of the FID that follows the 90˚ pulse is related to the growth of the magnetization along the positive z axis, occurred since the initial 180˚ [60].

Such pulse sequence is called inversion recovery (IR), as a first rf pulse invert M_0 and its pulse sequence timing diagram could be written as ($\pi_x - \tau - (\pi/2)_x - FID\ acquisition$).

A magnetization will return towards equilibrium according to the equation, assuming exponential T_1:

$$M(\tau) = M_0(1 - 2e^{-\tau/T_1}), \quad T_1 = \tau_1 \ln 2 \tag{4.4.26}$$

where τ_1 is the time τ at which M(t) crosses the zero value.

In order to get a correct estimation of T_1, the sequence should be repeated for different values of τ, the corresponding FID then are plotted against the variable recovery time, and using equation 4.4.26 T_1 could be computed. For the *z* component of magnetization to return to thermal equilibrium one need to wait for $5T_1$ between sequences. A quick estimation of T_1 could be done using the equation $T_1 = \tau_1 \ln 2$. A schematic of the IR sequence is shown in Figure 4.4.11.

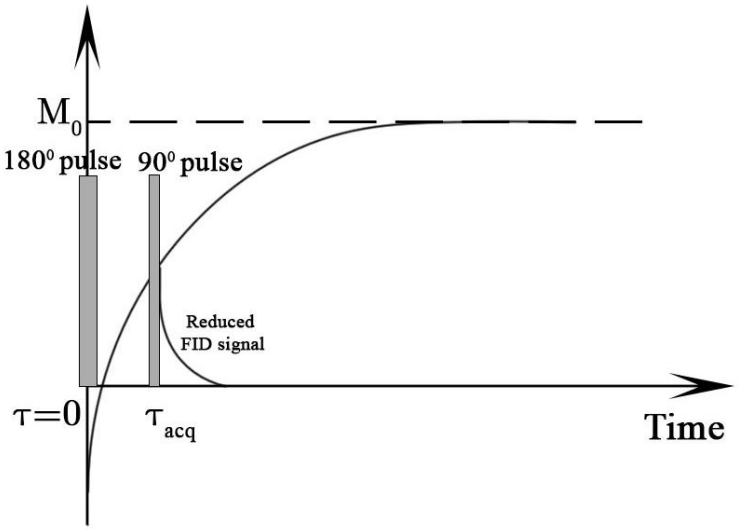

Figure 4.4.11 - A schematic representation of IR sequence.

Another possibility is to use Saturation recovery (SR) sequence for T_1 measurements, which uses 90˚ pulse, followed by the 90˚ pulse at the time τ for signal detection. The equation for the SR sequence is:

$$M(\tau) = M_0(1 - e^{-\tau/T_1}) \tag{4.4.27}$$

Such sequence simplifies the equation to which data must be fitted and shorten the time for measurements, as an infinite train of 90˚ pulses can be used [60].

4.4.3 Measuring crystalline solids

Up to now, measurements of the relaxation times were discussed in relation to the relaxation of ^{1}H nuclei in a liquid phase, specifically - water. With the use of different experimental methods, it is possible to measure low mobility ^{1}H, solid as crystalline water in cement samples. The T_2 of such components is extremely short due to the strong interactions of protons, not averaged to zero by molecular motion [67].

The first method described here is the solid or quadrature echo (QE) sequence, which could be written as a train of pulses $P_{90x} - \tau - P_{90y} - \tau$ - *echo.* Two 90˚ pulses are different in phase for the purpose of refocusing magnetic dipolar interactions between rigidly bound pairs of protons. The solid echo is produced at time 2τ. This sequence allows one to distinguish between solid and liquid components, because the solid component created by the refocusing has a Gaussian shape, while the liquid component decays exponentially with T_2*.

This method allows to avoid the use of equipment with very short time resolution. Usually spectrometers suffer from the dead-time of a few microseconds, due to the saturation of the receiver pre-amplifier by the rf pulse and needs time to restore. It was found [68] that for rigid spin echo refocuses with the error proportional to the fourth power of τ, which measures the deviation of the echo from the Bloch decay in the beginning. The magnetization in this experiment could be described as:

$$M(t) = M_{sol}\exp\left(-{(t-2\tau)^2}/{T_{2sol}^2}\right) + M_{liq}\exp\left(-t/T_{2liq}^*\right) \quad (4.4.28)$$

where M_{sol} and M_{liq} are the signal amplitudes of the solid and liquid part respectively, T_{2sol} and T^*_{2liq} are relaxation times of solid and liquid. To increase the signal-to-noise ratio (SNR) the sequence is repeated for a specific number of scans and the signal is averaged. Between the scans, a repetition time usually of $5T_1$ of the sample is used for the thermal equilibrium re-establishment.

To correctly estimate the relaxation time of the solid component, several experiments with 6-10 different τ values should be performed, usually in the range of 10-50μs. The values are incremented so the solid signal is the most visible and it is possible to capture its decay.

Data from individual measurements is fitted to the equation (4.4.29), Therefore, the solid intensity is extrapolated to τ=0 using another Gaussian to find the true solid fraction:

$$M_{sol}(\tau) = M_{sol}^0\exp\left(-{\tau^2}/{T_{2sol}^2}\right), \quad (4.4.29)$$

where M^0_{sol} is the value of M_{sol} at the τ=0.

Another possibility for the solid fraction exploration is the Pake-Doublet analysis [69].

In 1948 it was shown by G.E. Pake that it is possible to study the solid state of materials and to estimate the proton-proton distance from the ^{1}H NMR fine-structure spectrum. By studying gypsum, Pake found that the spectrum forms a “Pake doublet” (or “Pake pattern”) [69].

In addition to the polarizing external applied magnetic field B_0, neighbouring nuclei of a sample influence the magnetic environment of the absorbing nuclei. Therefore, the dipolar coupling among ^{1}H nuclei of a sample influences the shape of the NMR signal and the corresponding spectrum. In gases, liquids and some solids this influence is quite insignificant compared to the inhomogeneities of B_0. For the crystalline solids, atomic nuclei usually lie in certain lattice positions, and in this case the interaction of static magnetic dipoles is expected to influence the spectrum line widths and modify the spectrum shape for the nuclei of I=1/2.

Pake showed an analytical expression for such an absorption line, to which corresponds a complex FID curve, that, as Abragam has pointed out, bears a strong resemblance to a function which is a combination of a sinc function and a Gaussian broadening (Figure 4.4.12) [70]. However, Look et al. [71] succeeded in computing the Fourier transform of the Pake expression to determine the correspondent function in the time domain $G(t)$ (see eq. 4.4.30).

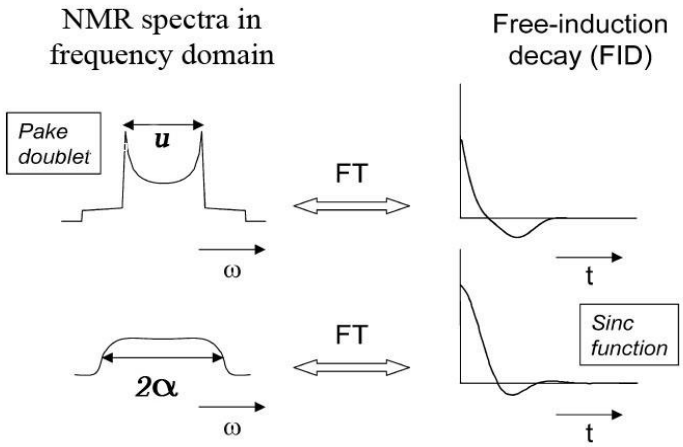

Figure 4.4.12 - NMR spectra in frequency domain, characterized by the Pake doublet and its FT, where u and α are parameters that indicate the characteristic widths in the spectra, and defined through equations 4.4.30 and 4.4.31 (u=4/3*α), adapted from [72].

The $G(t)$ function is the sum of a Gaussian modulated by an oscillating term, plus an exponential for the “liquid component” (free water) characterized by T_{2L}*:

$$G(t) = \alpha A\sqrt{8\pi}\, e^{-\frac{1}{2}\beta^2 t^2}\left[\frac{\cos(\alpha t)}{\sqrt{\alpha t}}C\left(\sqrt{\frac{6}{\pi}\alpha t}\right)+\frac{\sin(\alpha t)}{\sqrt{\alpha t}}S\left(\sqrt{\frac{6}{\pi}\alpha t}\right)\right]+M_L\, e^{-\frac{t}{T_{2L}^*}} \quad (4.4.30)$$

,

where $C(x)$ and $S(x)$ are the Fresnel integrals, β is the standard deviation of the Gaussian broadening function, which describes the extent of broadening by non-nearest neighbour ^{1}H nuclei, and

$$\alpha = \frac{3}{4}\frac{\mu_0}{4\pi}\frac{\gamma^2\hbar}{r^3}, \tag{4.4.31}$$

where r is the distance between the two interacting nuclei (proton-proton distance or radius), γ is the gyromagnetic ratio, μ_0 is the magnetic permeability of free space, and $\hbar$ the Planck constant divided by 2π.

The FID shape, function of the time *t*, can be therefore modelled by the function $G(t)$. In order to increase the SNR instead of a single FID, groups of adjacent FIDs acquired in IR sequences, called stacks, were used. Each stack was then analysed by using the function $G(t)$, to obtain two outcomes:

- to separate the signal in two components: "solid" and "liquid", and analyse the T_1 behaviour of both components

- to compute the distance *r* between the pairs of dipolar interacting ^{1}H nuclei.

Using such approach, it was possible to identify the chemical compound responsible for the observed behavior, by comparing the proton-proton distances computed by eq. 4.4.31 with the values obtained from SANS or/and SAXS measurements [73].

4.4.4 Relaxation in porous medium

The aim of this work is to gain information on cement materials, therefore in the following we will investigate by relaxation what is happening inside small pores, which is one of the most important and major relaxation processes inside the cement body, beside relaxation in bulk water and in crystalline solids, that were discussed in the previous section.

The standard model of the relaxation in porous media was developed starting from the work by Brownstein and Tarr [74]. Water in small pores can be divided into two fractions: water near the pore surface and water in the bulk of the pore. Water in the bulk will behave as "free liquid", and water near surface will have lower mobility, due, especially in cement materials, due to the adsorption on the surface and to the surface forces; relaxation of water on the surfaces can also be affected by paramagnetic impurities [67]. If the diffusion of the water molecule is fast enough, a single averaged relaxation time is observed, but if the diffusion rate is low, multiple modes can be observed [75].

Generally, in small pores, the rapid water exchange between bulk and surface ensures that the observed relaxation time is averaged.

Therefore, an averaged relaxation rate, denoted as the weighted sum of all the rates will be:

$$\frac{1}{T_2^{obs}} \approx \frac{\lambda S}{V}\frac{1}{T_2^{surf}} + \frac{(V-\lambda S)}{V}\frac{1}{T_2^{bulk}}, \qquad (4.4.32)$$

where S is the surface area of a pore of volume V, λ is the thickness of the surface layer (normally assumed to be a molecular monolayer) and T_2^{obs}, T_2^{surf} and T_2^{bulk} are the observed, the surface and the bulk relaxation time, respectively.

For a spherical pore (excluding the bulk component):

$$1/T_2^{obs} = 3\lambda/(aT_2^{surf}), \qquad (4.4.33)$$

where a is the radius.

The equivalent result for a planar pore of thickness b, that is often considered as a model for a cement gel pore, is:

$$1/T_2^{obs} = 2\lambda/(bT_2^{surf}) \qquad (4.4.33)$$

More precisely, if we speak about cement studies, several models for the longitudinal and transverse relaxation exist. For example, Schreiner et al. presented a simple 3-phase model with bound water, gel water and capillary water as phases. The model is widely used for the data interpretation. Bound water (chemically combined in CSH gel) has almost no mobility, have long T_1 (>100 ms) and extremally short T_2. The difference could be explained by the BPP (Bloembergen-Purcell-Pound) model, represented in Figure 4.4.13, that shows the dependences of the relaxation times on the correlation time (a parameter that depends on the viscosity and/or molecular size), defined as the time at which the average molecule rotates on one radian [75, 76].

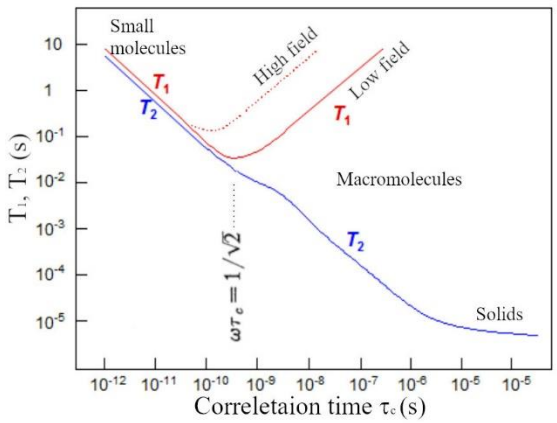

Figure. 4.4.13 - Graphical representation of the BBP model.

Another model was developed by Kimmich and co-workers [77], which observes a fluid in which molecules desorb from a surface, diffuse in a bulk-like layer close to the surface, before returning to the surface. A frequently applied model is the Korb model, developed by J.-P. Korb and co-workers, which could be applied to a mobile liquid in porous system in the presence of rare paramagnetic impurities, fixed at the surface of the pores [78]. Another model, developed by D. Faux and co-workers, called 3τ model, is designed for fluid molecules at a flat pore surface, describing water molecules dynamics in two distinct environments [79].

4.4.5 2D measurements

So far, all the experiments discussed are one-dimensional experiments, in the sense that the NMR signal is recorded as a function of a single time variable, but a lot of different powerful methods of NMR experiments are multi-dimensional. In such experiments the signal is recorded as a function of two or more NMR parameters.

The idea to use multi-dimensional experiments was firstly proposed by Jeener in 1971, but it was never published due to the technical drawbacks of the spectrometers at that time. The full potential of the idea was brought out by Ernst et al. five years later [80,81].

Though many types of 2D experiments exist, such as T_2-T_2, D-T_2 and T_1-T_2, in this study we will explore only the T_1-T_2 one.

2D experiments allow one to map transport, exchange, and molecular motion, and gained popularity in the wetting/drying processes of liquids in porous media [82].

2D methods with two parameters x and y employ the sampling of a data matrix M with varied time intervals τ_1 and τ_2. The acquired signal of a 2D experiments $M(x,y)$ and its relation to the correlation function $F(x,y)$ could be described by the Fredholm integral of the first kind

(it will be discussed in more details later in the text) with k_1 and k_2 representing the (separable) kernels related to relaxation processes that are continuous and smooth functions:

$$M(x,y) = \iint F(x,y)k_1(x,\tau_1)k_2(x,\tau_2)dxdy \qquad (4.4.34)$$

Concerning the experiments performed on this work, the effects of diffusion on the relaxation processes can be neglected thus justifying the separability of kernels in equation 4.4.34. But for fluids in porous media, in general, the influence of diffusion on relaxation cannot be dismissed [83] and the diffusion term should be considered [84] in the magnetization evolution following the Bloch-Torrey equation [85].

4.4.6 Data processing

In previous part we addressed the Fourier transform of the raw data, which is usually done for spectroscopy measurements in chemistry, but for relaxometry measurements the raw data are processed in the time-domain.

In the beginning of relaxometry experiments, data points were recorded and plotted of a graph plot by hand. If the relaxation is exponential, the data curve may be plotted on semi-log scale or the logarithm of the signal may be plotted on linear scale, and data points should lie on a straight line whose slope gives the relaxation time.

Nowadays, for data processing different computer programs are used. If the decay curves are mono- or bi-exponential, the analysis is pretty straightforward, but challenge lies for decay curves with more exponents. In this case an inverse procedure (a mathematical algorithm), commonly referred as ILT (Inverse Laplace Transform), could be used to extract time constants [86]. This kind of algorithms are implemented in a number of programs, such as CONTIN [87] or UpenWin [88].

It should be noted that the standard inversion of the Laplace transform does not perform the calculation of relaxation time distribution. Actually, in an inversion calculation the operation performed is an estimation of the solutions of a Fredholm Integral Equation (of the First Kind) [89]. But for simplification and as term “ILT” is widely used in NMR, it will be used through the text. Sometimes term linear fitting for ILT is used.

If the recorded data signal is noisy, conversion of the relaxation data by ILT presents an ill-posed problem, in the sense that even small noise could cause large changes in the spectrum [90]. Assuming that the signal originates from the collective molecules with T_2

distribution function *f*, the signal *M* could be measured as a function of delay time *t*, in the presence of the error *E*(*t*). The probability density $f(T_2)$ in this case is modelled as [91]:

$$M(t) = \int_0^\infty e^{-t/T_2} f(T_2) dT_2 + E(t) \tag{4.4.35}$$

This equation describes the superposition of signals relaxing independently, with $f(T_2)$ the amplitude of the component decaying with the relaxation time T_2. Here we assume that the noise *E* is additive, zero mean and white Gaussian noise. The problem lies in the estimation of $f(T_2)$, given a set of values for *M*(*t*) for a series of increasing values of *t*, and is an ill-posed problem. T_1 relaxation and diffusion problems could be resolved in the same way by changing the kernel function [90].

In matrix form equation 4.4.35 could be written as

$$M = KA + E, \tag{4.4.36}$$

where *M* is a data vector, *E* – noise, *K* is a kernel and *A* is the discretised version of a $f(T_2)$.

Theoretical work of the ill-posed inverse problem was done by Tikhonov and by Lavrentiev. It was proposed to use the smoothing or "regularizing" parameter for the noisy data. Usually, L_2 norm regularization method known as "Tikhonov method" is used. The method requires that the solution *f* minimize the sum of two quantity, one is the weighted sum of the squared residuals, the other quantity is one of several quadratic functionals of *f*, which accomplishes the smoothing of the function $f(T_2)$ by causing variations of *f* to tend to be small. The problem of regularization algorithm is the difficulty to choose an appropriate smoothing level [93]. In UpenWin software multi-regularization parameters are used, the algorithm is based on Tikhonow regularization, with the novelties to determine locally adapted regularization parameters and optional nonnegative constrain automatically computed [92].

In principle, ILT makes an a-priory assumption about relaxation time distribution. Another requirement for ILT data processing is high SNR. It has been shown that the resolution of the Laplace Inversion in the first approximation is more or less proportional to the SNR of the experimental dataset [90]. The regularization is used even for multi-dimension data, such as T_1-T_2, T_2-T_2 and D-T_2.

In the case of 2D measurements, which are usually acquired in regard to equation 4.4.35 with two separated components of a kernel – k_1 and k_2,

$$k(\tau_1, \tau_2, x, y) = k_1(\tau_1, x) k_2(\tau_2, x), \tag{4.4.37}$$

The matrix form of a probability density function in this case could be modelled as:

$$M = K_1 A K_2^T + E. \quad (4.4.38)$$

Here *M* and *E* are two-dimensional matrixes of an acquired data and noise respectively.

Another method used – is the discrete multi-exponential fitting, for which one needs to presuppose how many relaxation components with different relaxation times could be found.

For example, for a CPMG measurement, if we suppose that the signal was measured at echo times t_n, the decay of magnetization can be represented as the sum of N exponential decays with amplitudes A_n:

$$M(t_n) - E(t_n) = \sum_{i=1}^{N} A_i e^{-t_n/T_{2i}}, \text{ for n=1,2…, N=1,2…} \quad (4.4.39)$$

The data is then fitted with the use of methods for solving a minimization problem, such as simplex method or others.

The approach is to fit the decay curves with the smallest number of discrete exponential terms. This approach becomes inaccurate when more than two or three components are used or when two components have similar time constants. The data should be analysed with a continuous distribution approach in this case. It requires few a-priori assumptions and usually provides more stable fit [94].

4.4.7 NMR apparatus

NMR measurements are technically difficult as the compromise between resolution, sensitivity, cost and velocity of the measurements should be considered. The NMR signal is weak and the NMR properties should be measured with high accuracy. Some problems of resolution and sensitivity were resolved through time, but obtaining a good reliable signal with high SNR is still an instrumental challenge.

4.4.7.1 Magnet

Most of the NMR experiments require magnetic field with high homogeneity over relatively large volume of the sample in the Liquid-state NMR and even bigger region in MRI experiments, as a variation in space will cause a shortening of FID. Magnetic field should also be stable through a long period of time (i.e.: a stationary field), since Larmor frequency must not fluctuate, because some measurements could take hours to perform.

For example, water signal requires field homogeneity of about 1 in 100 over 1 ml. In this case signal will last for about 0.4 ms. While searching for the signal (sweeping the field) it is desirable that the field stays constant at least to within the linewidth $\Delta\omega$. This implies a time stability over many seconds. Such requirements could be met with a permanent magnet or an iron core electromagnetic magnet.

In chemical field or NMR spectroscopy large strong magnetic fields are needed, which could be achieved by the use of large superconducting magnets, but in case of cementitious materials investigation, especially concerning relaxometry, low-resolution NMR is used with a maximum field strength usually up to 1 T. A permanent magnet of the field strength of 0.05 to 0.5T, equivalent to Larmor frequency of 2 to 20 MHz, for ^{1}H are common.

For relaxation and spectroscopy measurements homogeneity is defined as a half-height width of the field strength distribution over a specified volume, for imaging application it is better to specify the maximum magnetic field deviation from the mean value over this volume, since the field deviation translates directly to image distortion. Homogeneity of the magnetic field is typically specified in parts per million (ppm) over a spherical volume, or diameter of sample volume (DSV).

As the absolute width of the field distribution increases as the field strength increases for a fixed homogeneity in ppm, it is better to express it as an equivalent NMR ^{1}H $T_2^{\Delta B}$ (decay time associated with inhomogeneity of the magnetic field):

$$1/(\pi T_2^{\Delta B}) = \Delta f_0 = \gamma \Delta B_0/(2\pi) \tag{4.4.40}$$

The presence of any magnetic susceptibility (i.e., the sample itself and inside the sample) will inevitably perturb the magnetic field and provide the Larmor frequencies of MR-sensitive spins with an unwanted spatial dependence. These perturbations which arise essentially from the Maxwell's electromagnetic field theory, and scale nearly linearly in magnitude with applied B_0 field strength [95].

B_0 field inhomogeneity lowers the SNR, which is at the core a Johnson noise (or thermal noise), brought by thermal fluctuations of stationary charge carriers and it does not depend on the material or configuration of the electrical circuit [96].

Theoretically, the SNR decreases with the square of the magnetic field strength, but in reality, the relation is not strictly proportional as many additional factors, such as RF penetration, radiative loss, quality of the coil, combine to reduce the theoretical SNR [97].

In order to improve homogeneity of the field and consequently to increase the SNR one can apply magnet shimming, which broadly refers to the optimized application of external magnetic fields for the compensation.

Magnet properties can be improved by the active or passive shimming technique. Active shimming uses steady electric currents flowing in shim coils around the active volume to modify the field profile, it allows precise control of the homogeneity [67]. Approximately two orders of magnitude of improvement can be achieved with the use of a set of up to 18 shim coils which correct for the various spatial derivatives of B_z.

Passive shimming, which involves carefully sticking small pieces of magnetic material to the pole pieces in order to modify the field, is usually performed by the magnet manufacturer as it requires special equipment and is suited to reduce large inhomogeneities [67].

4.4.7.2 One-sided magnet

So far, we were speaking about open bore magnets, magnets that contain an air gap between the two magnetic poles. A limitation of such magnet's arrangement is that the sample should be brought inside, and it must fit into the limited space between the magnetic poles.

One of the possibilities for relatively big samples, that require non-destructive analysis, is the use of the single-sided magnets. An origin of such device is the inside-out NMR, applied firstly many decades ago in the oil industry, for the so-called Log measurements. In that case the NMR equipment is lowered into bore holes to analyse the liquid in the surrounding rock matrix.

Although a concept of unilateral NMR existed for a long time, systematic investigation and application of such equipment started only in the mid 1990 with the development of the NMR-MOUSE (Mobile Universal Surface Explorer) in 1996 and 1998 [98, 99].

Though for long time the developments of the NMR equipment were made by increasing the magnetic field strength, its size, and decreasing inhomogeneity, meaning using large, unmovable superconducting magnets, that required cooling, inside-out NMR, used for the oil industry demonstrated that even magnets as low as 0.03 T with gradients of the order of 0.1 T/m is enough to measure the decay of transverse magnetization. Moreover, the echo techniques could be used to compensate for homogeneity problems.

NMR-MOUSE is a relatively small uniliteral NMR sensor that generates polarizing magnetic field strength up to 0.5 T with an adjustable gradient higher than 10 T/m.

Two are the most popular geometries for the single-sided magnet: U-shaped, or a horseshoe, first NMR-MOUSE design had such shape, and the bar magnet, which is the simplest geometry possible with a coil places at one of the magnet's faces. By optimizing the magnet and the rf coil it is possible to obtain a flat sensitive volume some distance from the sensor surface. A sample profile is obtained by simply changing the distance between sensor surface and the sample or by rerunning the resonance frequency [100]. In Figure 4.4.14 two uniliteral sensors of the most used geometries are shown.

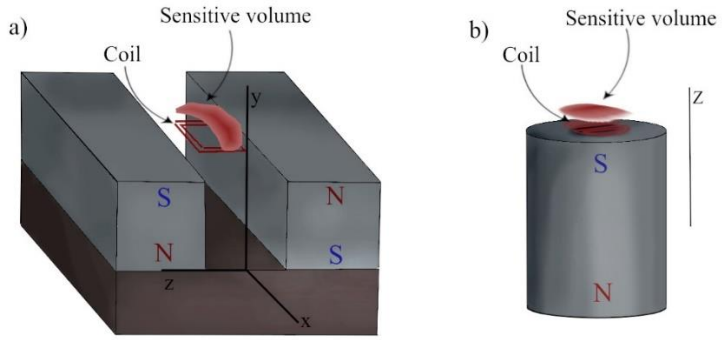

Figure 4.4.14 - Uniliteral NMR magnets of the most used geometries, where a) u-shaped magnet, b) bar magnet.

In many cases such equipment is used to discriminate NMR data as a function of depth in the sample. If samples are spatially homogeneous, the main goal is to maximize the detection sensitivity and increase the excited volume. These designs use the so-called sweet spot approach, which is the research of a region in the magnetic field with strong homogenous condition. Due to symmetry, in general along lateral directions first-order derivatives are zero and the only parameter that must be cancelled is the gradient along the depth direction [100].

A number of publications exist describing a single-sided magnet with different geometries, such as single bars with a hole inside, barrel magnets with the bar magnet inside, cylindrical or square cross section that generate a static magnetic field perpendicular to the sensor surface. Later in the Section 8 we will focus more on the unilateral sensors consisting of the barrel and bar magnets inserted.

4.4.7.3 Sample probe

Sample probe is the most specialized part of the NMR apparatus and has several functions:

1. Locates the sample in the homogeneous magnetic field region;

2. Includes r.f. electronic circuits for transmitting the exiting R.F. train of pulses and for detecting NMR signals from the sample;

3. In some cases, it has a device to rotate the sample and/or to stabilize the temperature;

4. For specified purposes it can contain additional coils.

The coil geometry should ensure that the oscillating magnetic field B_1 is perpendicular to the main magnetic field B_0. The schematic of the probe is shown in Figure 4.4.15.

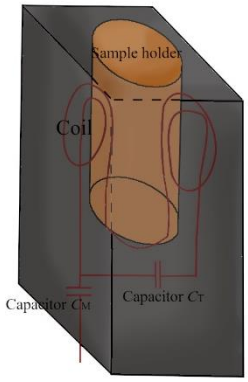

Figure 4.4.15 - Schematic representation of the sample probe.

Two capacitors C_T and C_M are the tuning and matching capacitors accordingly. The tuning capacitor is used to set the correct frequency of the oscillating circuit, while the matching capacitor to couple the external load with the pulse generator circuit to obtain the maximum signal transmission efficiency [62].

According to elementary circuit theory, a parallel circuit of capacitor C_T (in farads) and a coil of inductance L (in henrys) comprise an electronic oscillator with frequency in radians per second:

$$\omega_{osc} = (LC_T)^{-1/2} \qquad (4.4.41)$$

The tuned oscillator acts as accumulator of the energy, when the r.f. pulse arrives from the amplifier, it sets up the oscillations in the tuned circuit, if pulse frequency is close to the oscillator frequency, oscillations build up. The signal detection is the reciprocal process.

With such system the quality factor of the coil Q is increased, but it should be noted that it does not increase SNR, as the coil noise voltage is also increased [60].

The number of turns of wire in the solenoid coil influence the voltage. Consider cylindrical coil with the number of turns $N=4W^2/(\pi d^2)$, where W is a size of a square winding cross-section and d is a diameter of a wire.

The voltage induced in the coil will be:

$$V = B\omega_{osc}\pi D^2 N/4 \quad (4.4.42)$$

In order to obtain a high *Q* factor, coils are operated much below their self-resonance frequency and the number of turns is limited, $N<<c/(D\omega)$, where c is the speed of light [101].

In case of uniliteral magnets, the coil is usually placed on the magnet surface, it could be "printed" or composed of the flat wire, bar magnets coils are built in a similar way. Surface coils produce a B_1 field perpendicular to the B_0 magnetic field, which is in turns perpendicular or parallel to the surface of the coil. The perpendicular one is based on a single loop in the plane, and frequently used for the u-shaped magnets, while parallel are based on the at least two opposed current loops.

In uniliteral magnets, coils play more important role as its combination with the magnet determines the size of the sensitive volume. In the case of depth profiling measurements, the rf coil must be designed to generate and detect signals only from the region where the B_0 field is constant, a condition that assures a highly flat sensitive volume. In this case the lateral selectivity provided by the rf coil is crucial. As a rule of thumb, the lateral extension of the selected region is of the order of the diameter of the rf coil. The variation of B_1 across the selected volume strongly depends on the particular rf coil geometry. Any B_1 inhomogeneity results in a sensitivity loss, as well-defined 90 and 180◦ pulses cannot be generated even for on-resonance spins. Notice that each point in the profile is defined by the response of all spins inside the sensitive volume and that there is no lateral localization other than that provided by the coil.

The sensitivity and homogeneity of the coil can be increased by optimization. The knowledge of the magnetic field and its calculation is crucial in this case. The calculation using Bior-Savart law is one of the most used methods as it could be applied for coils of different geometries [102]. The Bior-Savart law and calculation will be discussed in following chapters.

4.4.8 Application of NMR technique in cement studies

Cement is a porous material with pores containing water, which makes cement a suitable material for ^{1}H NMR measurements, as water contains ^{1}H nuclei.

NMR technique have a lot of advantages in the field of cement and rocks studies, such as:

1. Samples do not require drying or other preparation before measurement;
2. The technique is non-invasive and non-destructive;
3. It is possible to study samples *in-situ* continuously over time;

4. Experiments can be easy and quick to perform;
5. Allows quantification of the main cement components – crystalline solids, porosity and hydrates.

Such properties of cementitious materials as porosity, pore size distribution, specific surface area and others could be studied by the NMR technique. It is also possible to analyse molecular diffusion, permeability or allowing separate measurements of surface and subsurface properties.

As water molecules play the role of the probe in NMR study of cement, it is possible to study sorption process, meaning pore-size distribution, loss of the water, and its return to the initial state of the sample.

The first investigation of WPC material by NMR was performed by Blinc et al. in 1978 [103]. Relaxation time T_1 and T_2 of PC and C_3S pastes were studied through hydration from 10 minutes up to 28 days. In the work only one component (one relaxation time) of the pastes was shown. In 1985 Schreiner et al. [104] were among the first who separated the acquired signal into two and more components, as well to investigate hydration process of the cement. In that work, 4 distinct stages of hydration were identified. Halperin et al. [105] were among the first researchers to use fast exchange theory in NMR experiments on cement and to calculate total surface area and its changes due to hydration process. A lot of different studies were carried out on the cementitious materials in the following years, including solid state NMR experiments, such as Si MAS-NMR on hydrated cement with additives (silica fume) [106].

One of the first works done with MRI on the materials with porous structure to monitor internal water content was performed in 1979 by Gummerson et al. [107]. An advantage of MRI is the possibility in relatively easy way to monitor a sample *in-situ*, for example for sorption studies, showing promising results for the porous materials and possibility to monitor transport of liquid inside the samples as in work by Bohris et al. [108]. One of the first works with the use of MRI for cement measurements was performed in 1995 by Bogdan et al. [109] and by Jehng et al. in 1996 to study freeze-thaw cycles of cement [110].

Greener et al. [111] in 2000 measured with the use of a 26 MHz system spin-spin relaxation of white cement as a function of time, finding good correlation between NMR results and measurable chemical and stoichiometric variations inside the cement structure during the hydration process, which allowed a better description of the cement gel structure.

In 2003 one of the first measurements with Fast Field cycling (FFC) NMR technique were done on cement samples by Barberon et al. [112] and Plassais et al. [113]. This technique

measures spin-lattice relaxation time rate R_1 ($1/T_1$) as a function of the magnetic field strength over a range of frequencies. FFC allows one to obtain information on the molecular dynamics such as characterisation of rotational dynamics, of surface exchange effects, of local diffusion effects, of translational diffusion in bulk and geometrically restricted environment etc.

In 2005 one of the first detailed analysis on the cement samples with the use of two-dimensional NMR T_1-T_2 exchange experiment was performed by McDonald et al. The study showed direct evidence of the chemical exchange of water between gel and capillary pores during cement hydration [114].

Few studies, such as [115] by M. Gombia et al and [116] by V. Bortolotti et al were done on the endodontic cement. In the studies, endodontic cement porous structure formation was monitored through hydration up to 30 days, it was possible to distinguish chemical compounds and to successfully monitor the build-up of the nano- and subnano-structured C-S–H gel.

In 2013 Muller et al. [117] followed cement hydration. They measured densification of C-S-H and measured pore-resolved desorption isotherm. In 2016 Gajewicz et al. [118] did a systematic study of the cement pore structure on mature samples, stating that the volume of water in pores larger than 10 nm exceeds that in smaller pores [119].

In 2013 a sort of 2D analysis was performed on the WPC pastes through hydration. The analysis allowed to distinguish two solid components, ascribed to Ettringite and Portlandite. It was found that the solid components were increasing through hydration in amount and it was possible to confirm surface relaxation effect of water in pores [120].

In 2014 the possibility to study crystalline water contained in Ettringite and Portlandite of mature cement samples with the T_1 relaxation time and Pake pattern fitting was showed by Bortolotti et al. [121]. The results obtained in the same study by a proper analysis of the NMR relaxometry data were interpreted with a picture of the porous structure at nano and sub-nano levels consistent with the Jennings colloidal model for C−S−H gel [19]. Actually, those results strongly supported the picture of C−S−H gel developing in comparable-sized clumps of the same composition, but not easily interpretable by models proposing quasi continuous sheets of C−S−H layers.

Considering previously studies done on cement samples, we can classify the pore structure depending on T_2 values and pore sizes of the WPC sample. The relaxation times could vary from study to study, but the overall range is shown in the Table 4.5.1 for an as-prepared sample (28 days of hardening under water).

Table 4.5.1 Typical relaxation times of a components of an as-prepared WPC.

^{1}H components (water in different space or pores)	Size (nm), circa	T_2 relaxation time (ms)	T_1 relaxation time (ms)	Reference
Capillary pores	10^3	12-40		[117, 118]
Interhydrate pores	10-20	0.80-2.0	5-10	[67, 104, 117, 118, 146]
Gel pores	3-5	0.3 - 0.5	0.5-1	[67,73, 104, 117, 120, 146]
Interlayer spaces	1	0.1 - 0.2		[67, 73, 118, 120, 146]

In relation to the sorption studies, as it was said, one of the first desorption isotherms for the cement samples studied by NMR was done by Muller et al [117]. The results are shown in Figure 4.4.16.

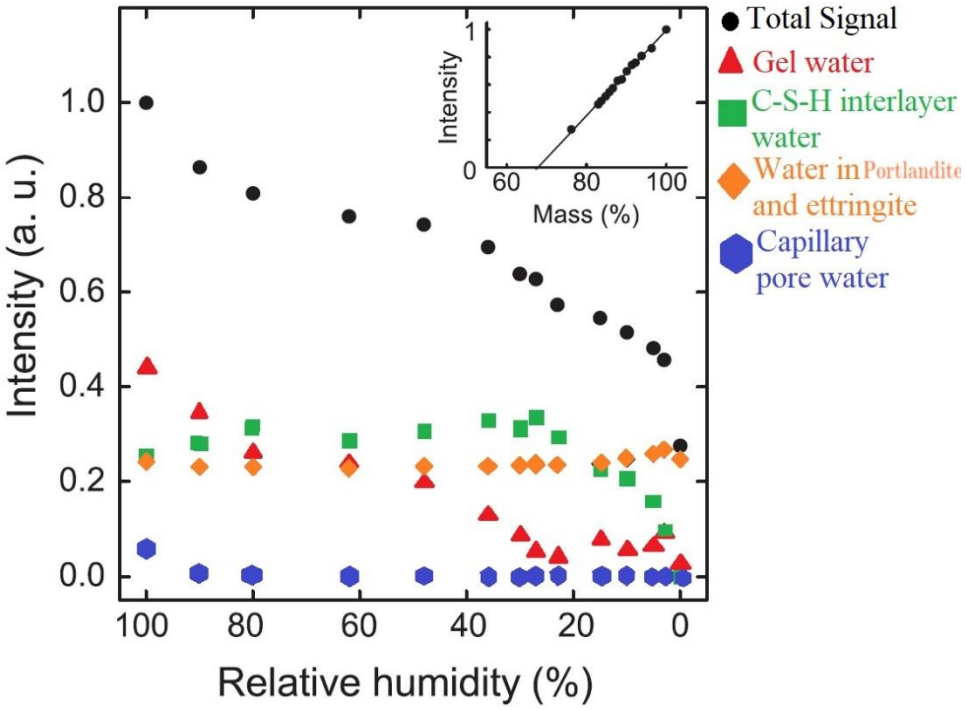

Figure 4.4.16 - Pore classes resolved from desorption isotherm experiments for progressively dried cement sample with w/c=0.4, adapted from [117].

Nevertheless, nowadays, the number of publications using NMR technique for building sorption isotherms is quite limited and overall suffers from different type of experiment preparations and absence of a uniform sorption theory.

5 Materials used and methods applied in this NMR study

5.1 Materials

For the sorption cycles investigation, WPC from Aalborg was used. The water-to-cement ratio of the samples used are 0.4, 0.45 and 0.5. The chemical composition of the cement is shown in Table 5.1.1 (private communication [147]).

Table 5.1.1 Chemical composition in percent of the WPC samples used.

Al_2O_3	CaO	Fe_2O_3	MgO	Na_2O	P_2O_5	SO_3	SiO_2	SrO
2.46	68.41	0.31	0.75	0.21	0.27	2.16	24.52	0.14

Samples with 5.5% of gypsum by the weight of cement were used (labelled WPCG). Cement powders were stored in the desiccator at constant RH and room temperature.

The mixing procedure used here was proposed by the head of LMC (Laboratory of Construction Materials) at EPFL (École Polytechnique Fédérale de Lausanne). The samples prepared with the following steps: in accordance with the desired w/c ratio, the dry cement powder was mixed with distilled water for 2 minutes at 1600 rpm. Prepared past was cast into a Teflon home-made mold to set. After 24 hours, hardened sample was put into the NMR glass tube to harden for 28 days, with water added to the glass test tube to completely cover the sample. After 28 days samples were measured with NMR (referred to “as-prepared” state) and subjected to drying. Some samples were maintained intact with the sizes circa 1 cm in height and 0.8 in diameter (sized determined by dimensions of the NMR tube), some other samples were crashed to millimetre size pieces and then placed in the tube. For 2D NMR measurements, a number of samples were hardened for longer time – circa 2 months and had shape of disk with radius ≈ 20 mm and height ≈ 8 mm.

Samples were dried in three different ways:

- In home-made RH chamber with the use of different chemicals, such as saturated salt solutions, silica gel and glycerol. Overall, it took circa 6 months for one sorption cycle. Temperature and RH was constantly checked by the data logger;
- Partial dried in RH chamber down to 10% RH;
- In the oven at 60˚C for three days or more (up to one week);
- In the vacuum oven under 60˚C and is -0.1 bar (relative pressure) for three days;

Samples of a long sorption cycle were re-saturated in the RH chamber by increasing RH levels step-by-step. Partial dried samples were re-saturated under-water, without vacuum pump. Samples dried in the oven were re-saturated under water with the use of vacuum pump. Samples for the 2D measurements were re-saturated with water uptake by placing the disk samples in the petri dish with water under the sample.

5.2 Methods

NMR measurements were done at 25°C using a relaxometer composed of a permanent magnet (ARTOSCAN, ESAOTE, Genova, Italy) with a magnetic field $B_0 \approx 0.2$ T (corresponding to ^{1}H Larmor frequency ≈ 8 MHz), a probe equipped with a 10 mm solenoid coil, and an NMR console (Stelar s.r.l., Mede, Italy). The dead time of the spectrometer was 25 μs. The NMR set-up is shown in Figure 5.1.1.

a) b)

Figure 5.1.1 - NMR set-up, where a) permanent magnet and NMR console, b) probe with a sample in a glass tube.

T_2 data were obtained using the CPMG sequences (Paragraph 4.4.2 and Figure 4.4.11) with the value of the parameters listed in Table 5.2.1.

Table 5.2.1 Parameters of the CPMG experiments.

Parameter name	Value
Echo time (μs)	60
Repetition delay (s)	0.6 - 1
90 ° pulse width (μs)	4.5 - 5
Number of scans	100 - 200
Number of echoes	512-2048

Values with the dash in Table 5.2.1 and in the following tables through this paragraph indicate that, depending on the type of the sample and its condition, different values for some parameters were used. As it was said in the paragraph 4.4.2, waiting time (repetition delay) for

thermal equilibrium in between pulses should be $5T_1$ (between consequential scans) which means that the choice of NMR parameters is always a compromise between measurement duration and quality of the data.

When the samples were dried the overall signal intensity was small, a larger number of scans for one measurement was needed. For as-prepared samples the repetition delay was longer, with a smaller number of scans. The choice of the number of echoes depends as well on the relaxation time of the sample, therefore, experiments for dried samples could be run with a smaller number of echoes than for as-prepared.

T_1 relaxation time data were acquired using the Logarithmically distributed Aperiodic-Pulse Saturation Recovery (LAPSR) [122] pulse sequence and the Inversion Recovery sequence. Parameters for the LAPSR and IR sequences are listed in Table 5.2.2.

Table 5.2.2 Parameters of the LAPSR and IR sequences experiments.

Parameter name	Value LAPSR	Value IR
Repetition delay (s)	1E-05	0.6-1
90 ° pulse width (μs)	4.5 – 5	4.5 - 5
Number of scans	40-140	40-100
Number of blocks (BS)	128 (512)	128 (512)
BINI (μs)	30	25
BEND (s)	1.6 – 2.4	1.2 – 2.4

In the Table 5.2.2, BINI is an initial τ value (see paragraph 4.4.2.5) and BEND is the last τ value, where it increased logarithmically and should be 5 times the longest T_1 of a sample.

The analysis of the LAPSR and CPMG data were done with the use of Uniform PENalty (UpenWin) software, developed by the Bologna group [88], described in details in Paragraph 4.4.6. For comparison and verification, multi-exponential non-linear fitting was also used (see Paragraph 4.4.6) with the help of Psi-Plot software [123] and scripts, done by the Bologna NMR group (see Appendix A).

UpenWin software was used to obtain the T_2 distribution, which implement ILT fitting with uniform-penalty smoothing with applied non-negative constrain (for more information see Section 4.5.6). Values of T_2 shown in the text are the geometric-mean value produced with the percentage of each component by UpenWin computation. For more detailed explanation on how UpenWin fits NMR data, we suggest to look through next works by G.C. Borgia et al, published in 1998 [124] and G.C. Borgia et al, published in 2000 [125].

For exploration of the solid components of the cement samples also QE sequence was used with the parameters listed in Table 5.2.3.

Table 5.2.3 Parameters of the QE sequence experiment.

Parameter name	Value
Echo time (μs)	20; 22; 24; 28; 30; 32; 36
Repetition delay (s)	0.8 - 1
90 ° pulse width (μs)	4.5 - 5
Number of scans	200
Block size	1024

To analyse the data from the QE sequence, Psi-Plot software was used with scripts, done by Bologna NMR group (see Appendix A). The overall procedure for the data analysis of QE data is described in Paragraph 4.4.3.

2D NMR measurements were done at the Department of Physics and Astronomy (DIFA) of the University of Bologna with the use of NMR-MOUSE PM10 (Magritek, NZ) with a field gradient of 14 T/m, size of the sensitive volume *x*,*y*,*z* [15x15x(0.1-0.3)] mm^3, and a magnetic field in the sensitive volume B_0 = 327 mT. In Figure 5.1.2 the NMR-MOUSE PM10 set up and its graphical representation are shown.

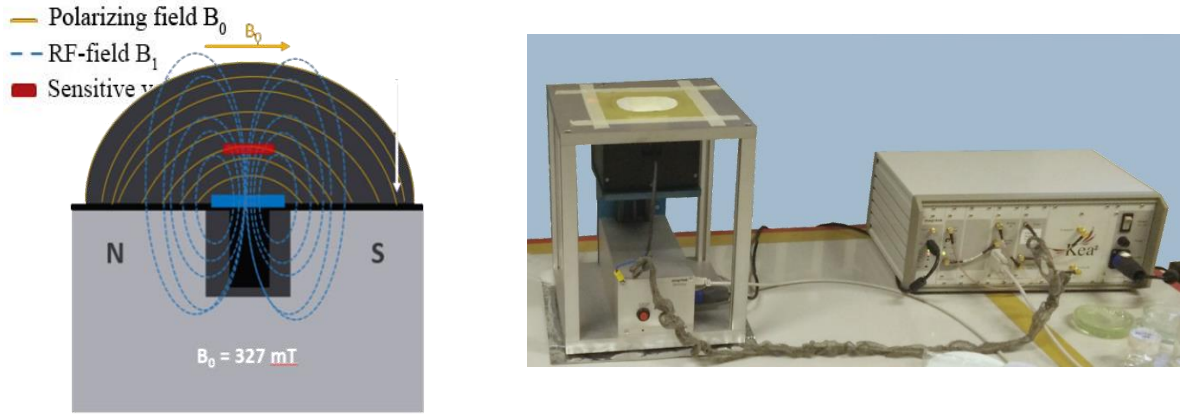

a) b)

Figure 5.1.2 - NMR-MOUSE PM10 a) graphical representation “cut-through” plane along vertical axis of symmetry, b) photo of the set-up.

T_1-T_2 measurements

T_1-T_2 experiments allow one to correlate longitudinal and transverse relaxation time distributions and obtain the T_1/T_2 ratios used for the study of molecular surface relaxation mechanisms in porous material and it is very useful tool for the cementitious materials study.

The T_1-T_2 data could be obtained using a conventional saturation recovery pulse sequence detected by a CPMG pulse train as shown in Figure 5.1.3. The recovery time τ_1 and the echo time τ_2 are two independent variables and the data are acquired as a two-dimensional array $M(\tau_1, \tau_2)$ [126]. Over the time τ_1, the spin magnetization decays along z axis, which is essentially a longitudinal relaxation process (T_1). Instead, during the τ_2 period the relaxation is due to the transverse process. The acquired signal relates to the probability density function $s(T_1, T_2)$ as [126]:

$$M(t_1, t_2) = \iint (1 - e^{-\tau_1/T_1}) e^{-\tau_2/T_2} s(T_1, T_2) dT_1 dT_2 + E(\tau_1, \tau_2) \quad (5.1.1)$$

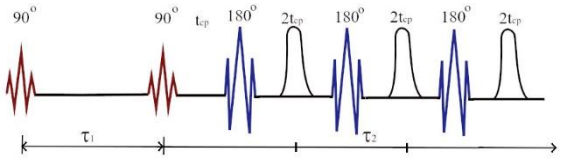

Figure 5.1.3 - Schematic representation of the typical T_1-T_2 experiment.

T_1-T_2 measurements were done with the SR-CPMG sequence, explained in the paragraph 4.4.5, with the parameters listed in Table 5.2.4.

Table 5.2.4 Parameters of the SR-CPMG sequence experiment.

Parameter name	Value
Echo time (μs)	50
Number of echoes	512
90 ° pulse width (μs)	5.5
Number of scans	64 - 80
Repetition delay (s)	1.8
Gradient	600 kHz/mm
δ_2 (μs)	1500
δ_1 (μs)	100

2D experiments were processed using Mupen2D and Upen2D package, which is currently under development by the NMR Bologna group. Upen2D [127] package is essentially a 2D extension of the Uniform PENalty (Upen) principle, to compute locally adapted regularization parameters and approximate solutions by solving a sequence of regularized least squares problems. The software is written in Matlab® script language. The numerical method implemented in Upen2D is an iterative procedure, its approximate distribution is obtained by solving a problem with Newton's Projection method. In recent time some additional changes were implemented to the algorithm, which is still in progress. For verification, the Wellington

software (Victoria University of Wellington Software) was used [128]. Unlike Upen2D, it uses a pure Tikhonov regularization parameter.

Solid components analysis

For the Pake-Doublet analysis, discussed in detail in the Paragraph 4.4.3, UpenWin software was used, along with a software tool (a Windows application called Stackview, developed by the Bologna NMR group) for stack exploration from IR datafile. The fitting of each separate stack was done with Psi-Plot software with the scripts developed by the Bologna NMR group (Appendix A). The Pake-Doublet analysis was performed on stacks of FIDs extracted at a proper inversion recovery time from IR datafile.

By the use of the equations 4.4.30 and 4.4.31 also the distance r_E and r_P between two interacting nuclei for Ettringite and Portlandite accordingly was computed. The exact values are shown in the paragraph 6 RESULTS.

The solid-liquid separation (it should be noted that in our experiments by "solid" we mean lower mobility protons, such as protons of crystalline water) and the resulting solid-T_1 and liquid-T_1 distributions computation were performed using UpenWin. This software automatically creates stacks of FIDs from IR sequences and using an empirical version of the function G(t) (eq. 4.4.30) and fits the stacks separating liquid from solid parts, where solid corresponds to the Gaussian part of the stack, characterized by the Gaussian time T_g, and liquid corresponds to the exponential part with relaxation time T_{2FID}.

The empirical model implemented by UpenWin is given by equation 6.1:

$$G(t) = X_2 \, e^{\left[-\frac{1}{2}G_{frac}\left(\frac{t}{T_g}\right)^2\right]} \times \left[1 - \frac{1}{2}\left(1 - G_{frac}\right)\left(\frac{t}{T_g}\right)^2 + C_c\left(1 - G_{frac}\right)^2\left(\frac{t}{T_g}\right)^4\right] + X_1 \, e^{-\frac{t}{T_{2FID}}} \quad (5.1.2)$$

,

where G_{frac} and C_c are solid-shape FID parameters. Specifically, G_{frac} is a coefficient, which corresponds to the Gaussian initial part of the FID, X_2 is the corresponding extrapolated amplitude for the solid, X_1 is the corresponding extrapolated amplitude for the liquid part.

The computed solid and liquid signals are saved in specific datafiles and then they can be processed by UpenWin to produce the T_1 distribution for solid and liquid populations.

Magnet design

For solving problems related to the design of the magnet for the single-sided instrument developed in the framework of the ERICA project (as for example: modelling the magnetic

field of the permanent magnet composed of NdFeB cubic blocks, modelling the magnetic field of a rf coil and finding the best construction wise form for the permanent magnet), specific software were used: Finite Element Method Magnetics (FEMM) [129], Ansys (Discovery AIM) [130] and the Matlab environment [131].

FEMM, a free open-source suite of programs with a CAD-like interface for solving low frequency electromagnetic problems on two-dimensional planar and axisymmetric domains, was used for the preliminary testing of the block's arrangement.

Ansys, a professional simulation tool offering integrated single discipline and multiphysics solutions to evaluate the performance of product design, was used for more detailed modelling and as a comparison and verification of the FEMM results.

For modelling the magnetic field generated by the rf coil, a MATLAB customized script was used by modifying the Biot-Savart magnetic Toolbox [132]. A detailed description of the script is reported in Appendix B.

Mercury Intrusion Porosimetry analysis

To have a more in-depth characterization of cement samples, also some MIP measurements were performed, and the results were compared with NMR results.

MIP is a popular technique to investigate porous structure of a material. It consists of intruding mercury through sample with high external pressure. Mercury is non-wetting material, which allows one to convert applied pressure to the pore size in accordance with Washburn equation:

$$r = -\frac{2\gamma cos\theta}{p}, \tag{5.1.3}$$

where r is the pore entry radius, p is pressure, γ is the surface tension of mercury and is equal to 0.48 N/m, θ is the wetting contact angel of mercury [133].

6. Results

In this chapter we show results obtained by experiments on cement samples through sorption cycles with different drying technique and different NMR measurements methods. In Paragraph 6.1 we show composition of cement samples with different w/c and with additional gypsum in the beginning of the hydration process. Additionally, we compare results with that obtained by ESR2. Paragraphs 6.2 and 6.3 shows results on as-prepared samples (28 days hardening) and 6.4 shows comparison of two raw NMR data processing methods: multi-exponential and quasi-continuous. In paragraph 6.4 and 6.5 we show results on sorption cycles experiments and solid components changes through sorption cycles respectively. In paragraph 6.7 we show MIP results on as-prepared cement sample.

6.1. Composition at the beginning of hydration (comparison with literature)

In the paragraph 4.2.1 the composition of the cement paste used in this study at the beginning of the hydration was described, and different models of the hydration process were presented. In this part we report the results obtained by T_2 quasi-continuous distribution analysis of CPMG data, during early hydration (up to several days) of the cement paste with WPC samples of 0.5 and 0.4 w/c. Likewise, the WPCG samples were investigated.

In Figure 6.1.1 examples of T_2 quasi-continuous distributions of the WPC sample with w/c 0.5 at different hydration times are shown.

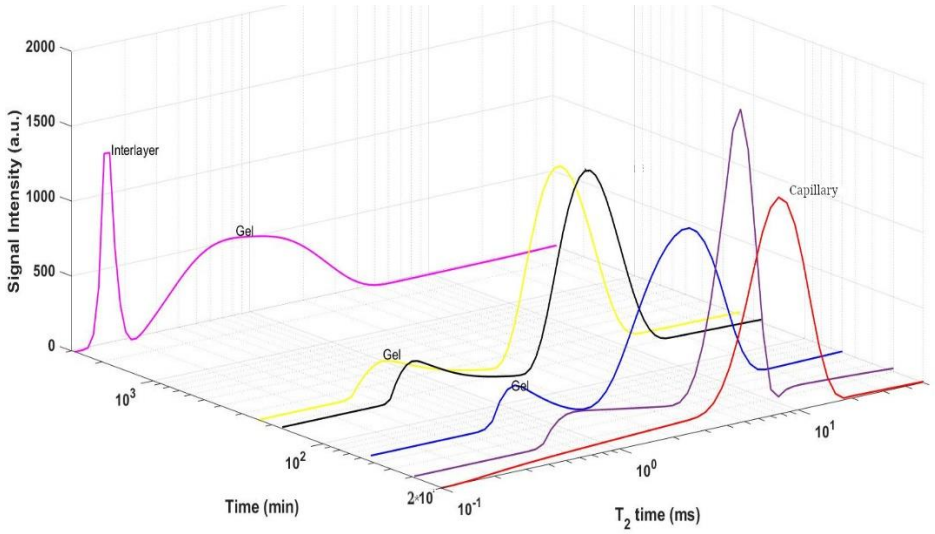

Figure 6.1.1 - CPMG T_2 distribution of the fresh WPC sample (0.5 w/c) through early hydration process.

As seen in Figure 6.1.1, at the beginning of the hydration (20-30 minutes, red curve in Figure 6.1.1) the distribution is bi-modal: a low intensity ^{1}H population with T_2 of around 500-1000 ms (not shown in Figure 6.1.1), which is most probably some residual free water, and a large intensity population with relaxation time around 8 ms, which is attributed to the capillary water. There is also some shoulder to the lower relaxation times (around 1 ms), which is seen as separated peak at later hydration time (60 minutes and more) and might indicate formation of the C-S-H gel pores.

The higher intensity peak shifts to shorter relaxation times through hydration and the observed relaxation time of the peak at 240 minutes is around 5 ms.

For comparison with literature, T_2 distribution data on WPC sample through hydration from ESR2 thesis [134] is shown in Figure 6.1.2.

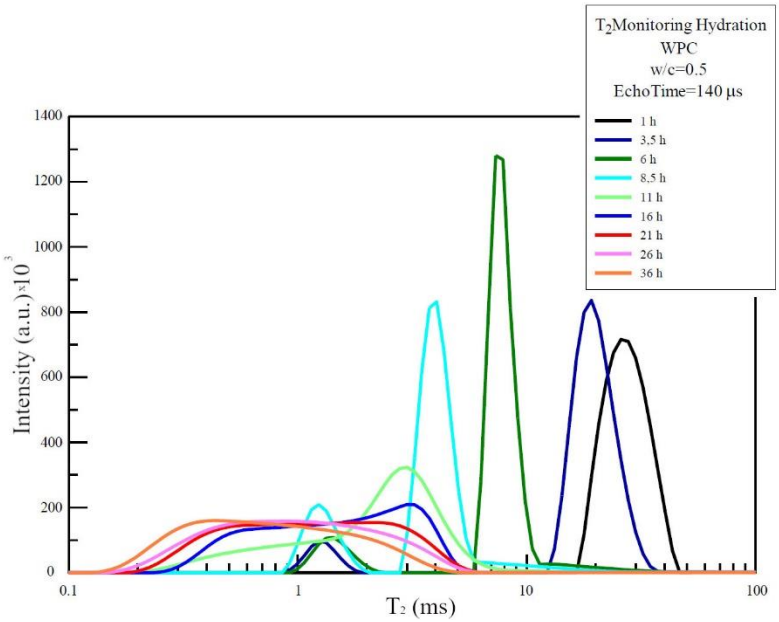

Figure 6.1.2 - CPMG T_2 distribution as a function of hydration time, adapted from (ESR2 thesis).

In this work, we studied also cement samples with the added 5.5% w/w of gypsum (WPCG). In Figure 6.1.3 T_2 distribution of WPCG sample at the beginning of the hydration process is shown. To understand how added gypsum influence porosity at the beginning of the hydration and observe the difference between samples with and without additional gypsum, in Figure 6.1.3 T_2 distributions from both samples are shown.

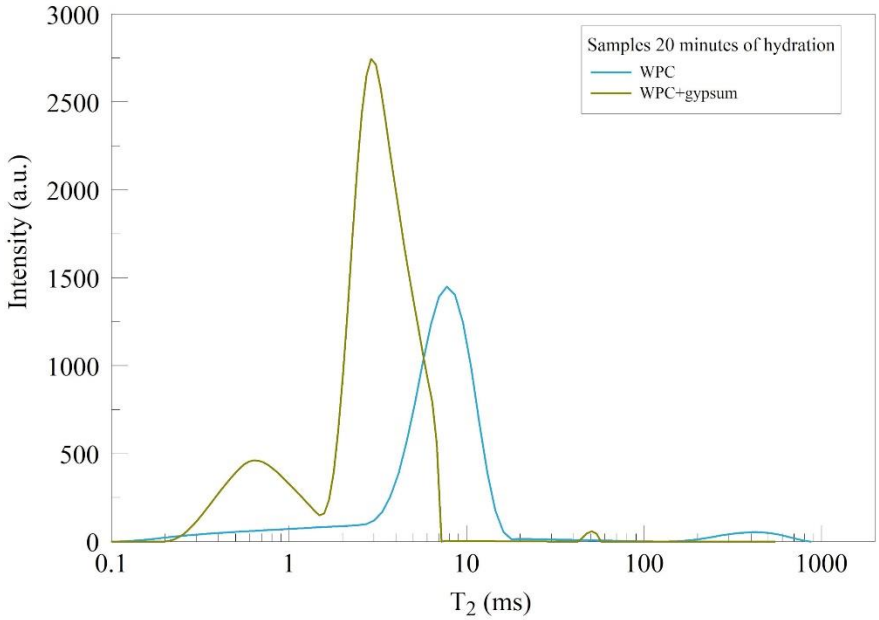

Figure 6.1.3 - T_2 distribution of the WPCG and WPC samples (w/c = 0.5).

As shown in Figure 6.1.3 already at 20 minutes of hydration it was possible to observe bimodal T_2 distribution for WPCG sample (0.6 ms and 4 ms components was attributed to gel pores and capillary pores respectively), where the sample without gypsum had one population with longer relaxation time (around 8 ms, representing capillary water) and some small signal for bulk water (500-1000 ms) which could be attributed to the cracks and voids.

In Figure 6.1.4 NMR measurements of the WPCG sample through early stage of hydration is shown.

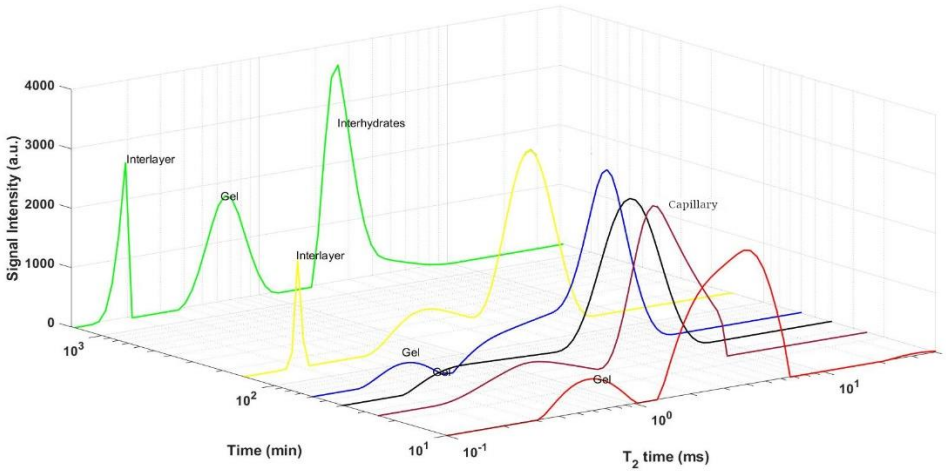

Figure 6.1.4 - T_2 distribution of the WPCG samples (w/c = 0.5) through early hydration stage.

As could be seen in Figure 6.1.4 in the beginning of hydration process, two distinct peaks could be observed (0.6 ms and 4 ms components attributed to gel pores and capillary pores accordingly) and a third peak (≈ 0.2 ms, attributed to the interlayer water formation) appeared already at 2 hours 30 minutes of hydration, whereas for ordinary cement sample with

the same w/c ratio, interlayer water was not observed until 48 hours, with the distribution remaining bi-modal.

In order to observe how the cement porous structure is changing depending on the amount of water (meaning water-to-cement ratio), we used samples with w/c 0.4. Notwithstanding, that difference between 0.5 and 0.4 w/c ratio is not very big, we still found differences in the hydration process for these samples. But, samples with the bigger gap between w/c ratios should be experimented on in the future.

T_2 distribution vs hydration process, from 10 minutes to a little more than 24 hours (light blue curve), of the WPC sample with w/c ratio of 0.4 is shown in Figure 6.1.5.

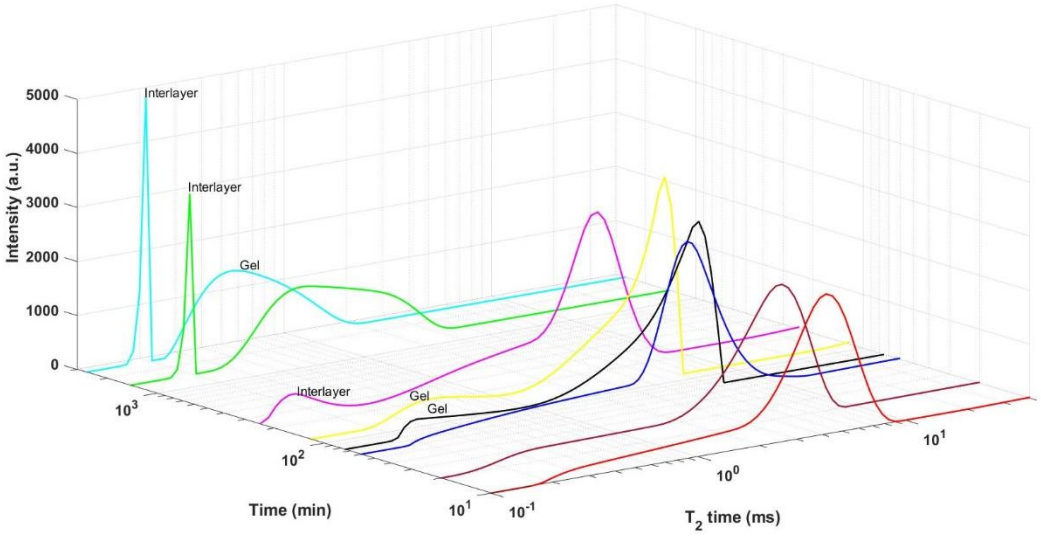

Figure 6.1.5 - T_2 distribution of the WPC samples (w/c = 0.4) through early hydration stage.

As it is seen from Figure 6.1.5, the hydration process for the 0.4 w/c sample did not fundamentally differ from other samples. At 1 hour of hydration two components were seen: at ≈5 ms (capillary water) and a small amount at ≈500 ms (bulk water). After 1 hour of hydration we observed the start of formation of the gel pores and at ≈2.5 hours, signal indicating interlayer water formation emerged. After 24 hours it was possible to observe clearly separated interlayer water signal (0.2 ms) and gel pore signal (0.7 ms) with small amount of water ≈60ms, indicating capillary water.

6.2. Porosity distribution and solid composition of the as-prepared cement samples

6.2.1. WPC of 0.5 water-to-cement ratio

In the introduction section, the porous structure of the as-prepared (100% RH, samples constantly kept under water, hardened for 28 days) WPC was discussed, and some references and description of the structure by the NMR technique were added. In the following, the T_1 and

T_2 distributions observed by the LAPSR and CPMG pulse sequences, respectively, and the results of QE pulse sequence used for the solid components, are reported.

In Figure 6.2.1 the T_2 distribution is shown, averaged over four 0.5 w/c WPC samples.

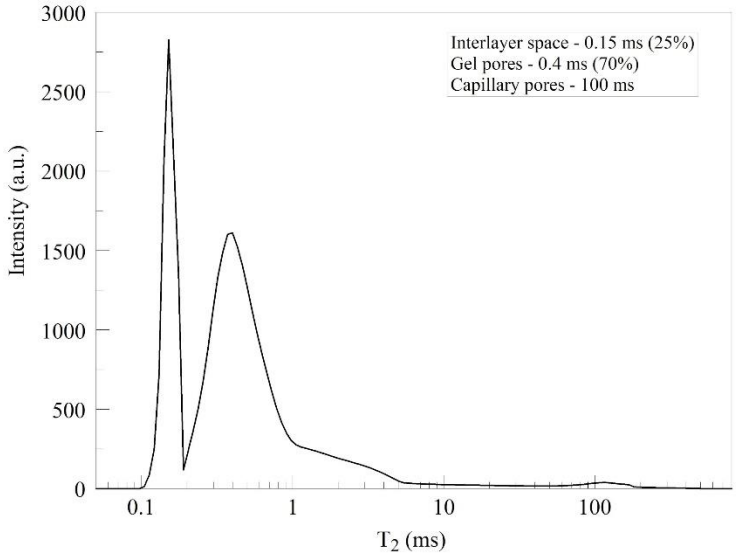

Figure 6.2.1 - Averaged over 4 samples T_2 distribution of the as-prepared WPC sample.

The relaxation times of the components is in a good agreement with literature [118], for example with the results, obtained by Gajewicz et al. for WPC sample of 0.5 w/c, hardened for 28 days, shown in Table 6.2.1.

Table 6.2.1 Characteristic sizes of cement porous structure and corresponding T_2 for a WPC as-prepared sample of 0.4 w/c, as reported in [118].

Assignment	Characteristic size (nm)	T_2 (ms)
Crystalline phase		$1.0 \cdot 10^{-2}$
Hydrate interlayers	1	0.2
Gel pores	3-5	0.6
Interhydrate pores	10-20	2
Capillary pores	10^3	40

The original table reported in ref. [118] also showed the amplitudes of the components. Here they were not reported because in Table 6.2.1 also the crystalline phases were included. Moreover, the sample was prepared with w/c 0.4 and in general, the experimental procedure was not exactly the same. Moreover, ref. [118] did not report information about the measurement uncertainties, so we can consider the T_2 values in the table as orders of magnitude, consistently with the intervals shown in Table 4.4.1.

In addition, differences between Table 6.2.1 and Figure 6.2.1 have most of their origin from the different approach used for data processing.

Figure 6.2.2 shows the T_1 distribution for the as-prepared 0.5 w/c WPC, averaged over four samples.

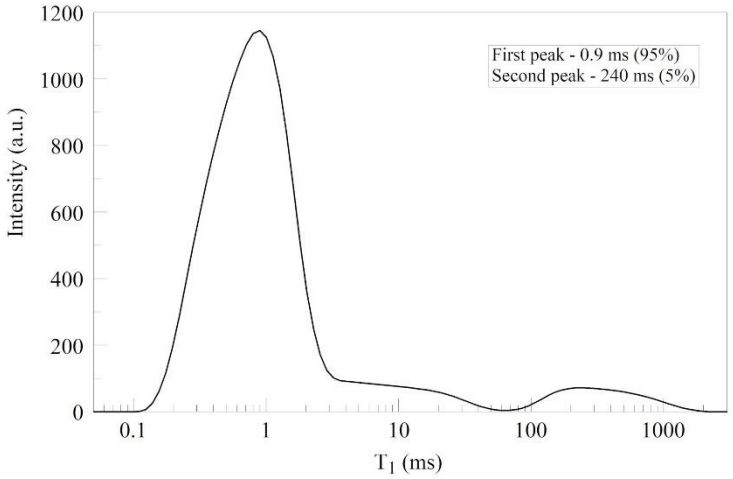

Figure 6.2.2 - T_1 distribution of the WPC sample 0.5 w/c ratio.

As seen in Figures 6.2.2 and 6.2.1 the overall shape of distributions is the same, one difference is that for the T_1 distribution the big peak (around 1 ms) is not separated into two groups of interlayer and gel water as for T_2 distribution, but the shoulder for T_1 around 10 ms and for T_2 around 2 ms is seen for both distributions (supposedly it corresponds to interhydrate pores) and the peak for capillary pores with the same signal amount (5%) is about 240 ms for T_1 and about 100 ms for T_2 amount. In some papers the ratio of T_1/T_2 for cement and some sandstones are around 1 – 2.6. In the presence of such a wide pore size distribution and therefore for water in such a wide distribution of conditions, including possible changes in surface relaxivity, the evaluation of a single value of the T_1/T_2 ratio can lose its meaning [135].

The dependence of a T_1/T_2 on pore geometry is explained in previously done works [114].

Figure 6.2.3 shows the averaged result from QE measurements for the same sample.

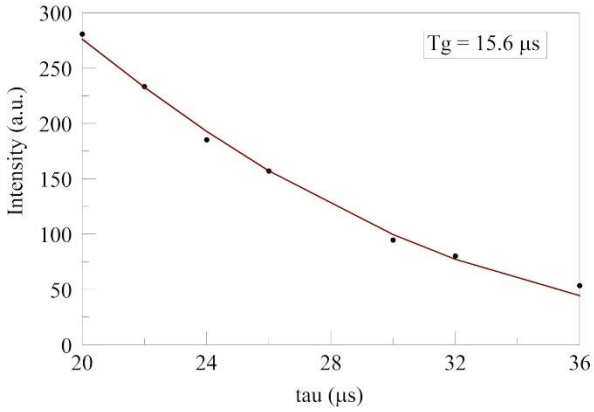

Figure 6.2.3 - QE measurements of as-prepared 0.5 w/c sample.

The T_g of the solid components was 15.6 µs, and the amount of the solid signal was around 25% which is in a very good agreement with the literature [118].

6.2.2. WPC of 0.4 water-to-cement ratio

In Figure 6.2.4 the T_2 distribution for the 0.4 w/c WPC is shown, averaged over measurements of 4 samples. The legend in figure reports the percentages and T_2s of the different components, computed by means of UpenWin.

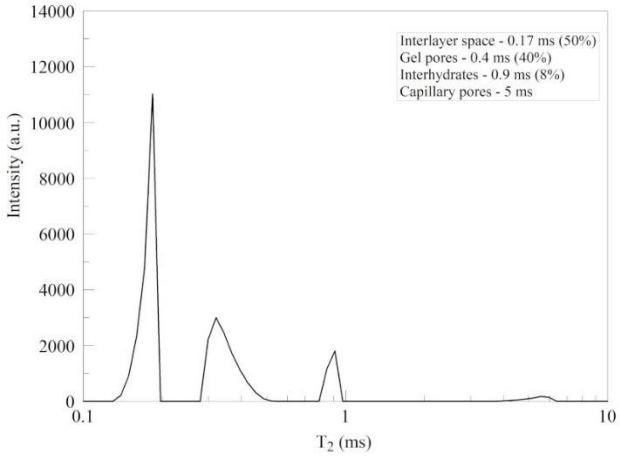

Figure 6.2.4 - Averaged T_2 distribution of the as-prepared WPC sample.

T_1 distribution of the WPC sample of 0.4 w/c is shown in Figure 6.2.5.

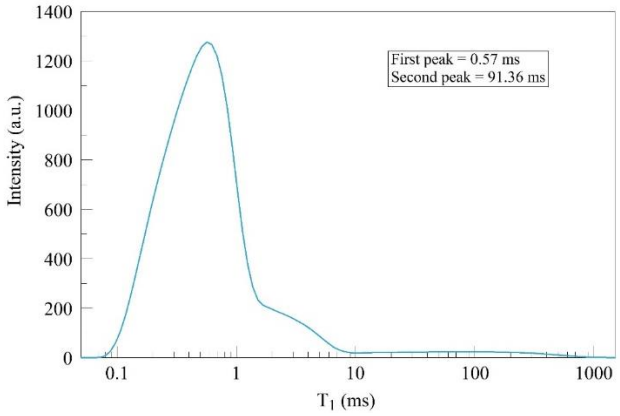

Figure 6.2.5 - T_1 distribution of the WPC sample 0.4 w/c ratio.

As seen in Figure 6.2.5, the T_1 distribution is similar to the T_1 distribution of 0.5 w/c, the difference is the same as for T_2 distribution, meaning that the main peak shows lower T_1 value here than for 0.5 w/c sample, which could represent bigger amount of smaller pores for the sample.

The results from QE measurements of the solid structure are shown in Figure 6.2.6.

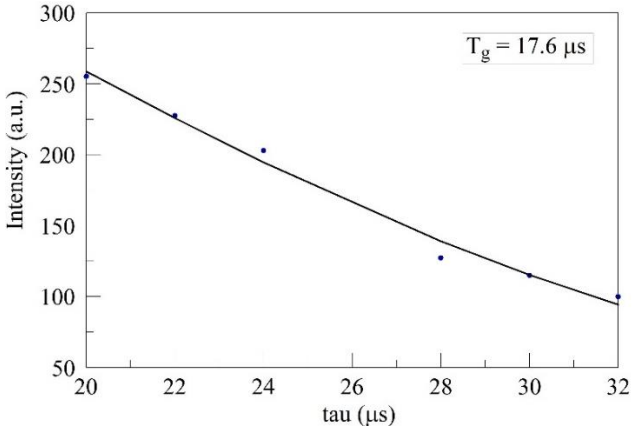

Figure 6.2.6 - QE measurements of the 0.4 w/c as-prepared sample.

As can be seen in Figures 6.2.6 and 6.2.3 and by the values of T_g, there is not so much difference between samples, and it could be explained by the data processing methods rather than physical difference.

6.3. Porosity distribution and solid composition of the as-prepared WPCG samples

In Figure 6.3.1 the results for the as-prepared 0.5 w/c WPCG sample are shown. In the inset percentages and the T_2s geometric average values of the component are shown, computed by UpenWin.

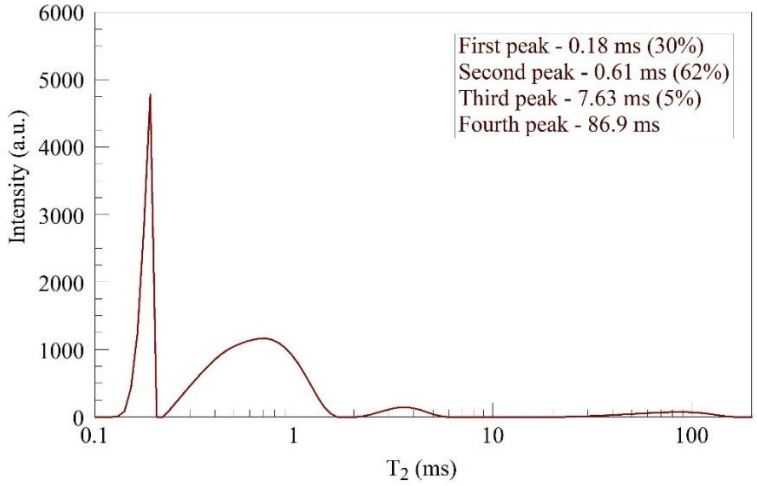

Figure 6.3.1 - T_2 distribution of as-prepared WPCG samples.

As shown in the distribution in Figure 6.2.1, it is not very different in regards to porous system of regular cement of 0.5 w/c ratio. The peaks position and amplitude of each components are almost similar to the one showed in Figure 6.2.1, the difference is in the position of second peak (presumably gel pores), which could be partial due to the computational uncertainty of noisy data.

T_1 distribution from measurement data of the WPCG sample is shown in Figure 6.3.2.

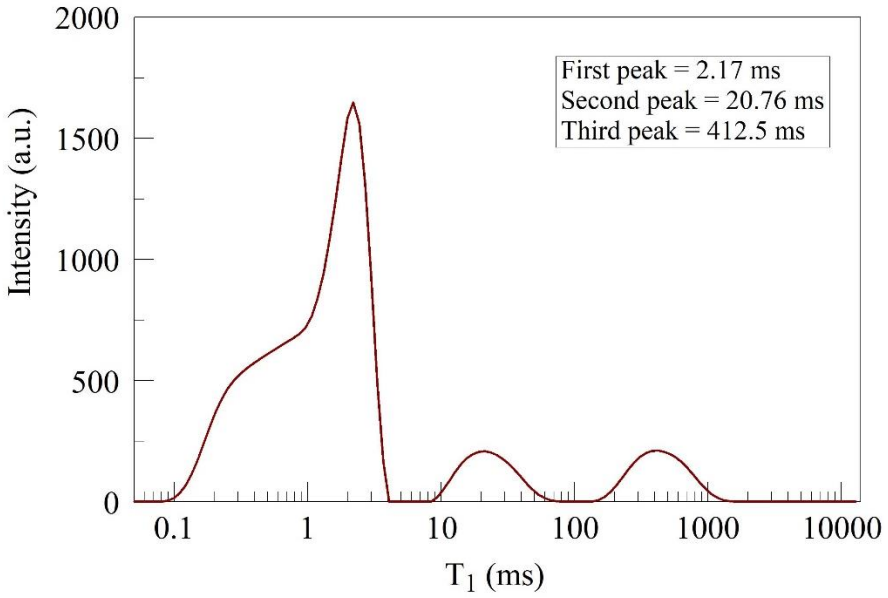

Figure 6.3.2 - T_1 distribution of the WPCG as-prepared sample of 0.5 w/c ratio.

As can be seen in Figure 6.3.2, just like for other WPC samples, the biggest peak might represent two proton populations – gel pores and interlayer water and it is similar to the 0.5 w/c WPC distribution in Figure 6.2.2 with the main peak shifted slightly to the right and showing longer relaxation time than in the distribution for 0.4 w/c sample. In this experiment

it is as well possible to see two more separated peaks which might be interhydrate and capillary pores and represent third and fourth peak in T_2 distribution in Figure 6.3.1.

Likewise solid structure of the WPCG sample was observed with QE sequence method and the result is shown in Figure 6.3.3.

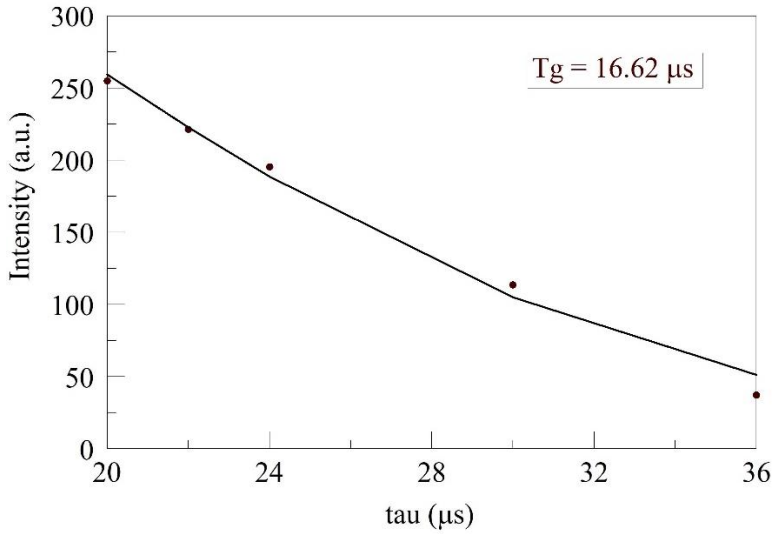

Figure 6.3.3 - QE measurements of WPCG sample of the 0.5 w/c ratio.

From QE measurements of all different samples, which are shown in Figures 6.2.3, 6.2.6 and 6.3.3 it is possible to conclude that solid structure was not different by the view of QE measurements, as it had similar T_g of a solid component and more or less the same amount of the solid signal.

6.4. Data processing methods comparison

As data processing methods could introduce differences about the estimated parameter values, which could affect the final analysis, the acquired data were processed by means of two methods – ILT (using UpenWin) and multiexponential fitting (using scripting for Psi-Plot).

Figure 6.4.1 shows comparison of a signal intensity separated into cement components for as-prepared samples of 0.5 and 0.4 w/c ratios.

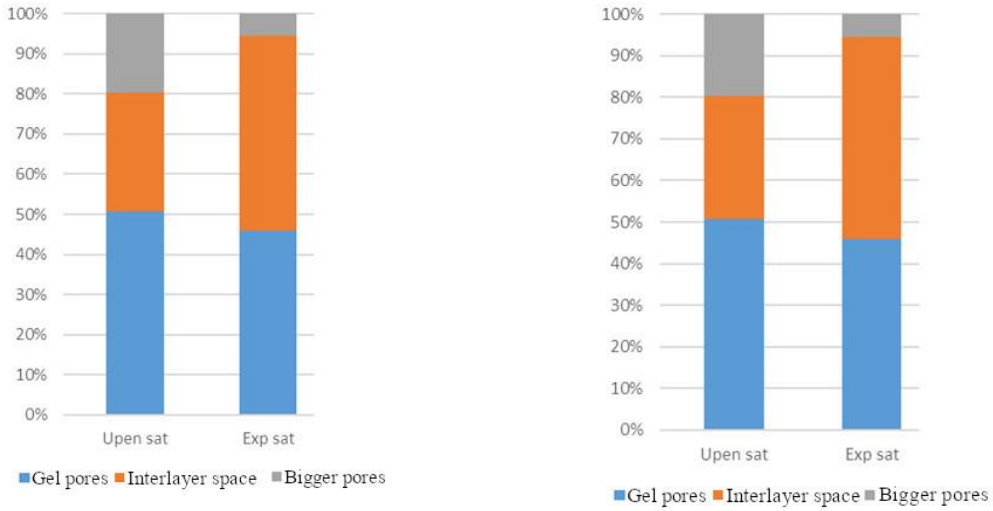

a) b)

Figure 6.4.1 - Different data processing methods comparison for as-prepared cement samples of a different w/c ratios, where a) 0.5 w/c and b)0.4 w/c.

The comparison of the T_2 values for the three components is shown in Table 6.4.1.

Table 6.4.1. Comparison of a T_2 values for cement components, discovered by UpenWin and multi-exponential fitting procedures

Pore population	T_2 by UpenWin (ms)	T_2 by multi-exp fitting (ms)
w/c 0.5		
Interlayer space	0.15	0.21
Gel pores	0.42	0.67
Bigger pores	1.32, 34.2	3.2
w/c 0.4		
Interlayer space	0.15	0.18
Gel pores	0.43	0.54
Bigger pores	1.4, 32.2	2.4

6.5. Evolution of the NMR signal through drying/re-saturation process

6.5.1. Full RH drying

Samples, both cylindrically shaped and crushed, were progressively dried from 100 to 5% RH and measured at 100, 80, 70, 60, 45, 35, 15, and 5% RH levels. Then, samples were re-saturated in the RH chamber and measured at 5, 18, 23, 40, 60, 70% RH levels. During re-saturation, a vacuum pump was used to reach 100% RH, and measurements were performed after one day and one week of re-saturation, respectively. Samples were examined

gravimetrically, till mass equilibrium was reached. No specific precautions were adopted to prevent carbonation. In Figure 6.5.1 sorption curve for cylindrical WPC sample of w/c 0.5 is shown. Total signal intensity was obtained by T_1 measurements. Mass in the graph is the water mass inside the sample.

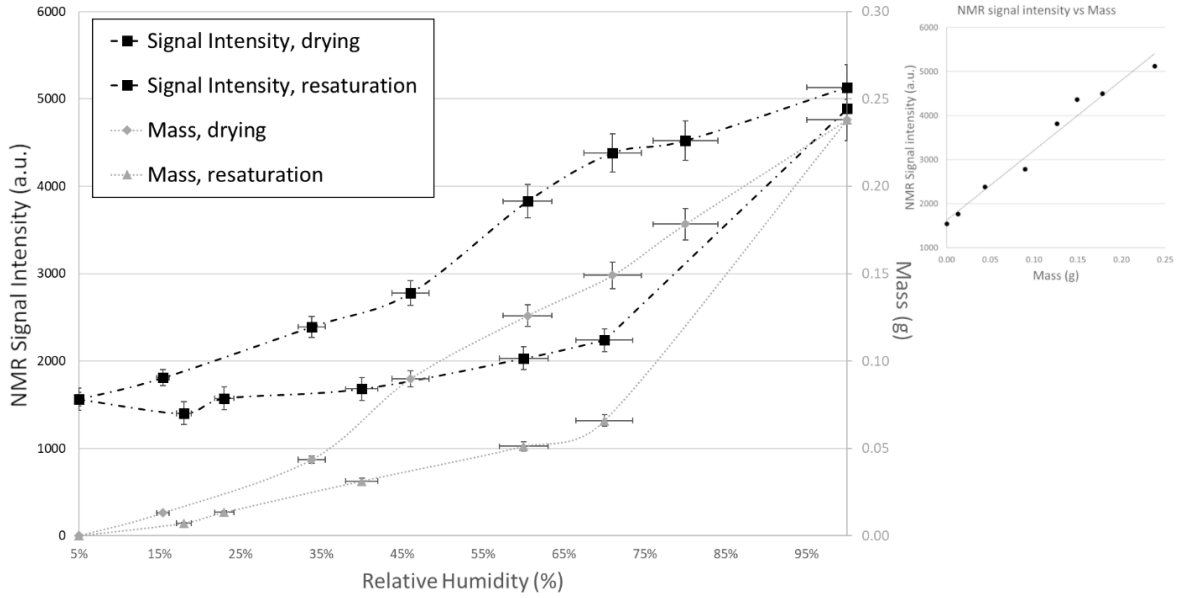

Figure 6.5.1 - Sorption curve of the progressively dried over controlled RH WPC sample with w/c of 0.5. On the left sorption curve is shown and on the right NMR signal intensity is plotted as a function of the water mass inside the sample.

The small graph on the right in Figure 6.5.1 stands for a quality control of the measurements. From previous works [136], it was concluded that the intensity of the NMR signal is proportional to the amount of water as a function of RH and as we dried the sample and evaporable water is removed, the mass loss should be proportional to the loss of the signal. The linear behavior of the NMR signal-mass relation indicates that all evaporable water was detected correctly. Also, as can be seen from Figure 6.5.1, the NMR signal does not start from zero, and this can be ascribed to the interlayer water, detectable by NMR, not lost by the drying process, that remains along with the whole RH range.

In Figure 6.5.2 some of the T_2 distributions for the sample at different RH levels are shown. Different proton populations, characterized by different T_2 classes, can be observed, ascribed to different classes of pores.

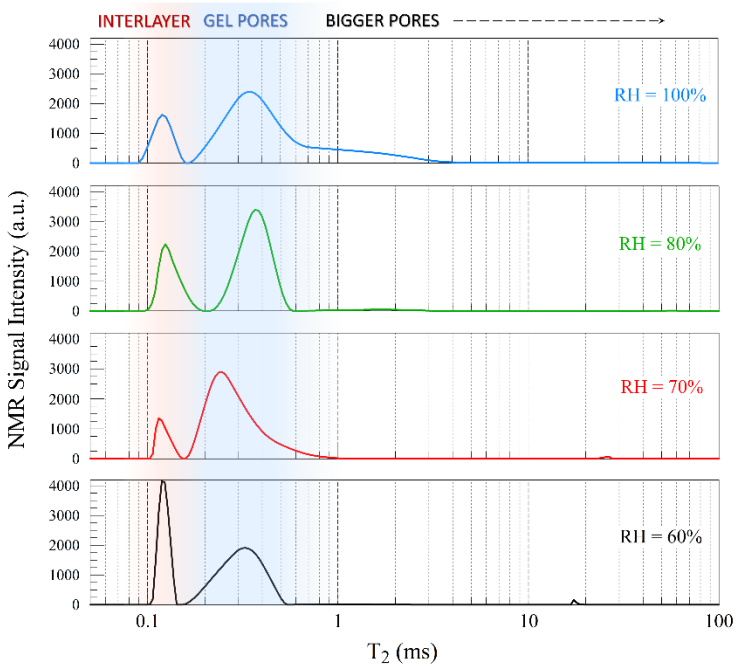

Figure 6.5.2 - T_2 distributions by UpenWin from CPMG measurements for cement, dried at different RH points. The intensity of bigger pores is so small that it is not visible in the plot.

Figure 6.5.3 shows the CPMG signal evolution, resolved into different ^{1}H components through drying and re-saturation, obtained on cylindrical samples. Here the signal intensity was normalized from 0 to 1, where 1 is the full signal intensity of the as-prepared sample. The dashed lines are polynomial spline curves to highlight the trend of the data. The error bar in the graphs corresponds to the 5% estimated by repeated measurements on cement test samples.

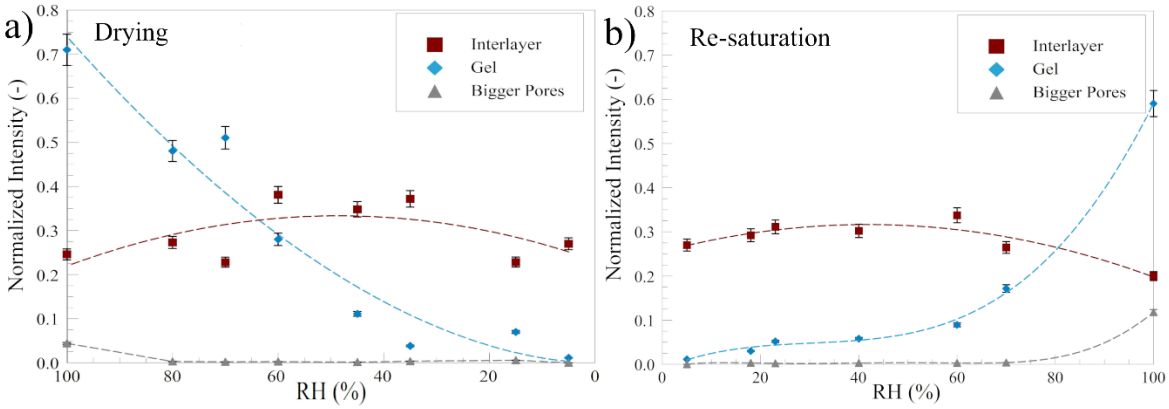

Figure 6.5.3 - Pore resolved signal intensity evolution through a) drying, b) re-saturation for the WPC sample of 0.5 w/c.

As it is possible to see from Fig. 6.5.3 a), the signal assigned to the gel pores water decreased through all the drying steps. Through the re-saturation process (Figure 6.5.3 b), it is seen that the gel pores water signal increased through all the steps. In Figure 6.5.4 changes of the T_2 of the interlayer space through drying and re-saturation are shown.

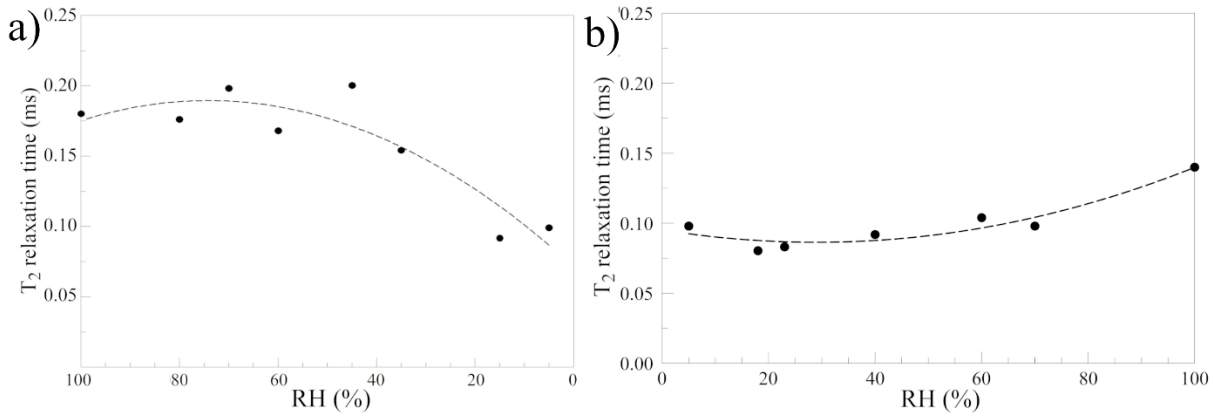

Figure 6.5.4 - Evolution of the interlayer space's T_2 through drying and re-saturation.

6.5.2. Partial drying

Samples, partial dried and re-saturated were observed by T_2 measurements as to understand at which drying point (RH level) changes to the structure are irreversible. Samples were dried down to 10%RH, at this level interlayer space signal remained the same. The structural changes due to such drying were distinguished.

Samples of 0.5 w/c were dried down to 10% RH and immersed in water for re-saturation. In Figure 6.5.5 T_2 distributions for as-prepared samples and dried are shown.

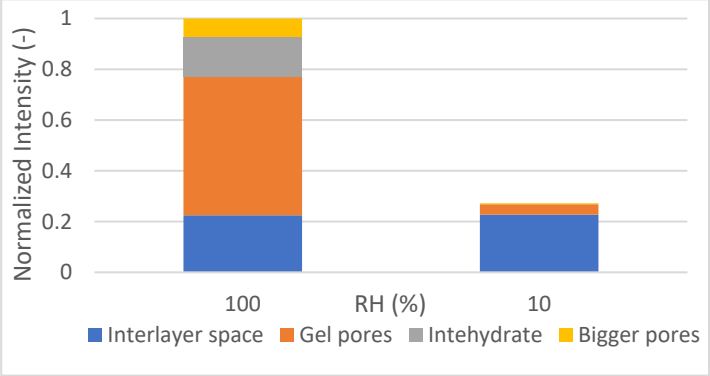

Figure 6.5.5 - T_2 distribution of the WPC partial dried sample of 0.5 w/c.

From Figure 7.4.5, it seems that the drying did not alter the amount of interlayer water signal, but for 10% RH we did not observe interhydrates, capillary pores and almost non-gel pores.

In Figure 6.5.6 re-saturation curve is shown.

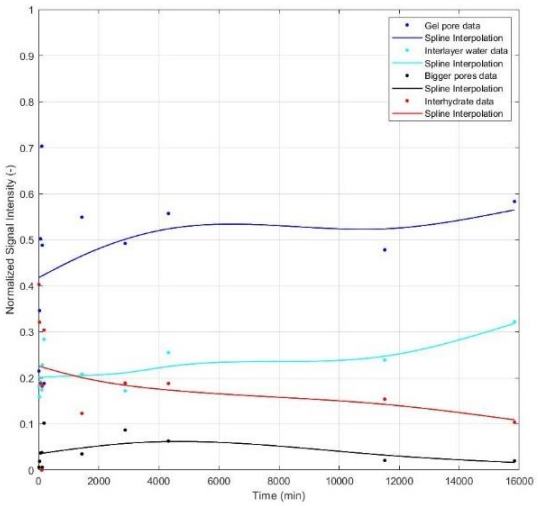

Figure 6.5.6 - Pore resolved normalized signal intensity evolution of partial dried WPC sample of 0.5 w/c through re-saturation.

As we will see later, for samples re-saturate with the same methods, gel pore signal, interhydrate and bigger pores (capillary and voids) showed a trend similar to other WPC samples, only not so sharp trend as for fully dried samples. Interlayer water did not show changes. For re-saturated sample we observed the same signal intensity as for as-prepared sample, but with slightly bigger amount of interlayer water and gel pore water, which might indicate changes of the structure. Further experiments are needed.

6.5.3. Oven drying

Some samples were dried in the vacuum oven and others in the ordinary oven. Cylindrically shaped samples with w/c 0.4 and 0.5 were dried up to two weeks. In Figure 7.4.5 separated pore resolved signal intensities are shown as a function of drying time (days) in the ordinary oven. The data are averaged over three samples.

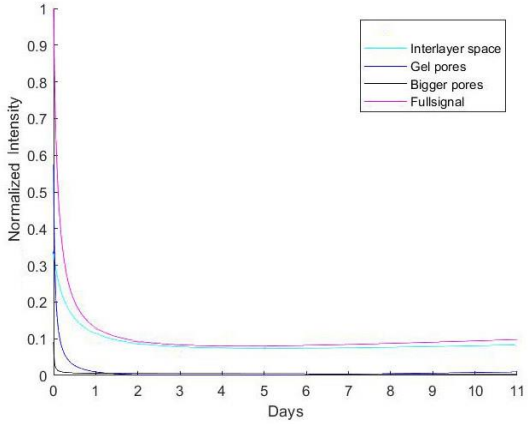

Figure 6.5.7 - Evolution of average estimated cement components through oven-drying for a 0.5 w/c WPC, computed by the inversion on CPMG data.

The solid lines in Figure 6.5.7 are merely a Spline trend. As seen in Figure 7.4.5 after the third day of drying the signal intensity reached a plateau and did not change till the end of the drying process. The remaining signal consists of the interlayer space, which is as well reduced two times (from around 25% to 13% of the whole amount).

Re-saturation of the same sample under-water is shown in Figure 6.5.8.

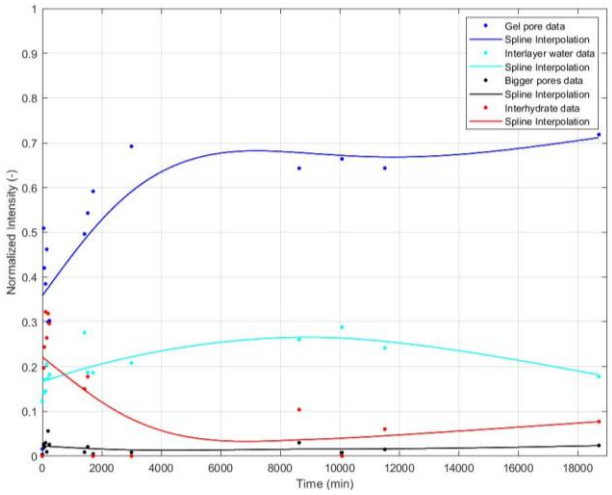

Figure 6.5.8 - Evolution of the of cement components resolved normalized intensity through re-saturation for 0.5 w/c, averaged over three samples.

As shown in Figure 6.5.8, the intensity for the gel pores and interhydrate pores increased and decreased accordingly up to 125 hours and stayed constant (with some variations due to signal scattering), whereas interlayer water signal intensity slightly increased up to circa 160 hours and then decreased. Nevertheless, the comparison of as-prepared and re-saturated T_2 distribution, which is shown in Figure 6.5.9 could serve as a proof to the mechanism of interlayer sheets collapsing.

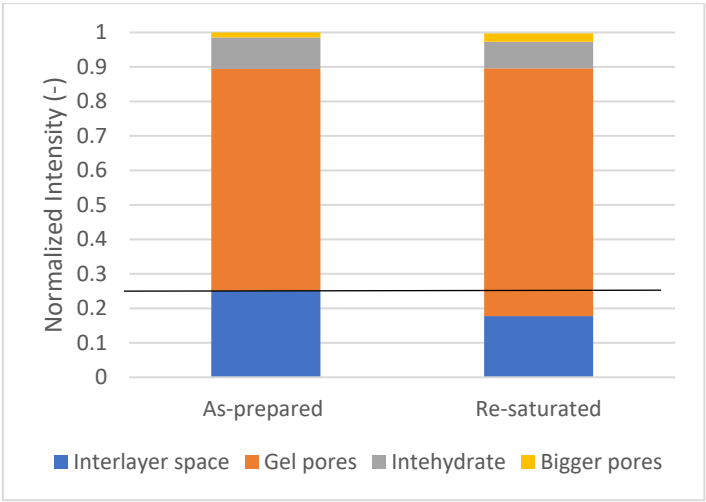

Figure 6.5.9 - Comparison of the T_2 normalized signal intensity of as-prepared and re-saturated averaged data.

The black line in Figure 6.5.9 is used as a guide for the eye to better see differences in gel pores and interlayer space signal intensity. As one can see, signal intensity of the interlayer space after re-saturation was less than in as-prepared state and signal intensity of gel pores increased, whereas bigger pores (capillary and voids) and interhydrate did not change significantly.

In Figure 6.5.10 pore evolution, resolved processing CPMG relaxation data, through drying in the oven, for 0.4 w/c are shown. Data are averaged over three samples.

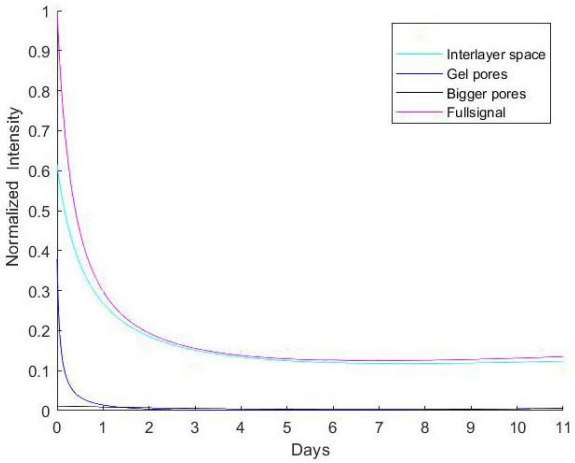

Figure 6.5.10 - Evolution of cement components, resolved from CPMG relaxation curve processing, through oven-drying for 0.4 w/c, averaged over three samples.

Similarly, to the 0.5 w/c samples, the solid lines are Spline trends. The samples were dried up to two weeks and after around 4th day the signal remained constant till the end of drying process.

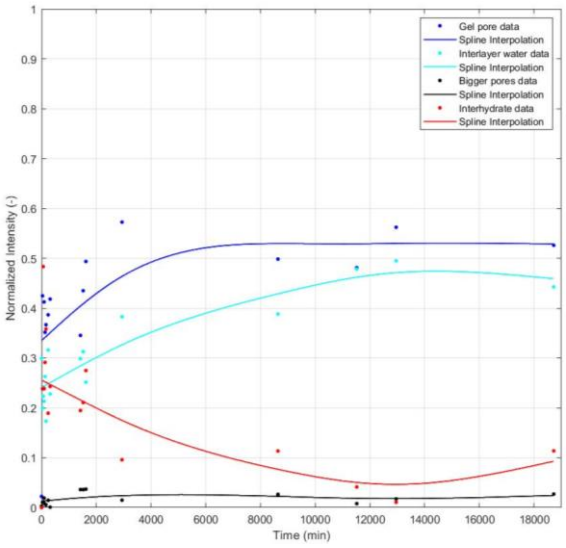

Figure 6.5.11 - Evolution of cement components, resolved from CPMG relaxation curve processing, of the averaged data for 0.4 w/c WPC through re-saturation.

As shown in Figure 6.5.8 and Figure 6.5.11, mechanisms for the re-saturation process and structural relaxation of the pore system for cement samples of different w/c ratios are similar.

A comparison of the as-prepared sample with the re-saturated samples is shown in Figure 6.5.12.

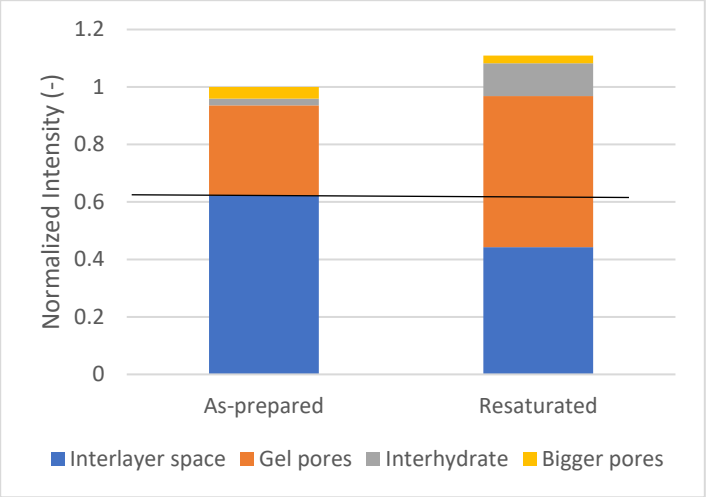

Figure 6.5.12 - Comparison of the WPC sample of 0.4 w/c: as-prepared and re-saturated.

As shown in Figure 6.5.12, there is a big difference in the amount of each signal and the difference is bigger than for 0.5 w/c sample despite the same drying and re-saturation processes and times.

Structure changes of the WPCG samples of 0.5 w/c ratio as well were observed during drying in the oven. Structural changes during drying of WPCG sample are showed in Figure 6.5.13 through T_2 distribution.

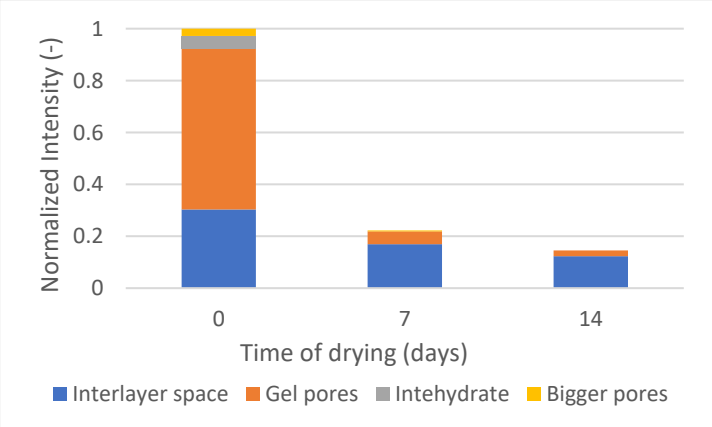

Figure 6.5.13 - Evolution of cement components, resolved from CPMG relaxation curve processing, through oven-drying for WPCG sample.

As shown in Figure 6.5.13 almost all of the signal after two weeks of drying consists of interlayer spaces with small amount of gel pores left. In the same way as for WPC samples, relaxation time of the interlayer spaces decreased to circa 100 μs, which suggests the same mechanism of interlayer sheets collapsing.

Re-saturation process, observed by the T_2 measurements, is shown in Figure 6.5.14.

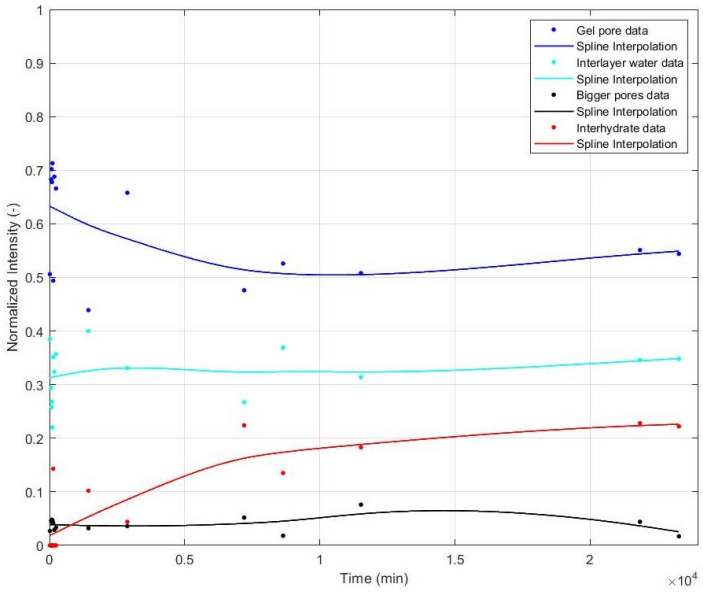

Figure 6.5.14 - Evolution of cement components, resolved from CPMG relaxation curve processing, through re-saturation for WPCG 0.5 w/c sample.

6.6. Changes in the solid composition

6.6.1. Pake-doublet measurements

In Figure 6.6.1 an example of the UpenWin analysis of the solid component, separated from the liquid is presented. The data presented are for a w/c 0.5 cylindrical sample, and the T_1 distributions of the solid component are shown for 100% and 15% RH levels.

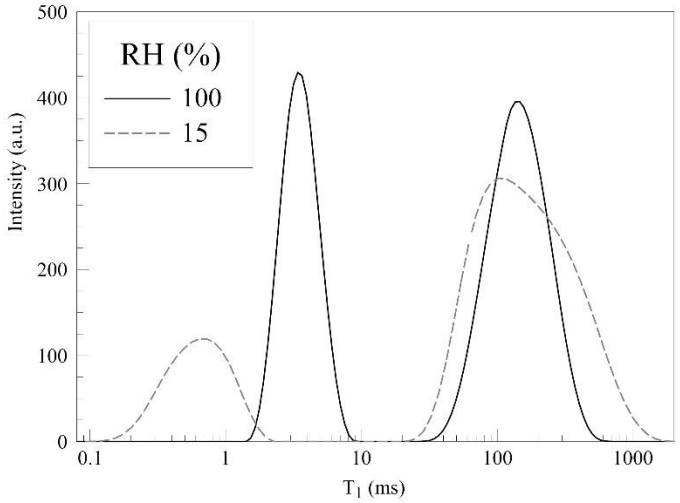

Figure 6.6.1 - T_1 distribution of the solid component computed by UpenWin after solid-liquid separation.

Stacks of FIDs which have a clear Pake-Doublet behaviour correspond to inversion times TI in the LAPSR sequence no shorter than 5 ms, meaning that these FIDs have contributions deriving only by the SL component. Therefore, only the SL component was examined. An example of the Pake-doublet fitting of a stack of FIDs contributed by SL is shown in Figure 6.6.2.

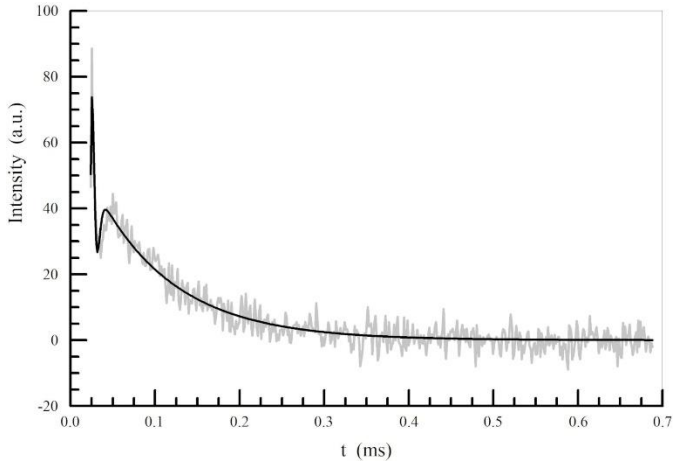

Figure 6.6.2 - Black solid curve is the G(t) function fitted to a stack of FIDs acquired from a WPC sample.

A significant improvement of the fit to Eq. 4.4.30 was obtained by assuming that the component SL was composed of two Gaussian populations with two different T_g values, and two different proton-proton distances, calculated by Eq. 4.4.31. Results of the fitting for the WPC sample of 0.5 w/c are shown in Table 6.6.1.

Table 6.6.1 Gaussian relaxation times T_{gE} and T_{gP} and proton-proton distances, for the two solid populations of the WPC sample, w/c = 0.5, dried at controlled RH.

RH(%)	T_{gE} (ms)	Proton-proton distance r_E (Å)	T_{gP} (ms)	Proton-proton distance r_P (Å)
100	0.011	1.58	0.028	1.89
80	0.013	1.42	0.038	1.95
70	0.010	1.47	0.037	1.97
60	0.010	1.46	0.033	1.96
46	0.011	1.40	0.032	1.93
34	0.013	1.44	0.036	1.91
15	0.011	1.45	0.036	1.98
5	0.010	1.48	0.033	2.00

Results for the sample of w/c ratio 0.5 dried in the oven are shown in Table 6.6.2.

Table 6.6.2 Gaussian relaxation times T_{gE} and T_{gP} and proton-proton distances, for the two solid populations of the WPC sample, w/c = 0.5, dried in the oven.

Time (d)	T_{gE} (ms)	Proton-proton distance r_E (Å)	T_{gP} (ms)	Proton-proton distance r_P (Å)
0	0.012	1.44	0.039	1.97
1	0.011	1.44	0.038	1.98
2	0.012	1.38	0.045	1.90
3	0.012	1.35	0.045	1.85
5	0.012	1.39	0.030	1.92
11	0.012	1.45	0.052	1.99

In Table 6.6.3 results for the WPC sample with w/c = 0.4 dried in oven are shown.

Table 6.6.3 Gaussian relaxation times and proton-proton distances for the WPC sample, w/c = 0.4, dried in the oven.

Time (d)	T_{gE} (ms)	Proton-proton distance rE (Å)	T_{gP} (ms)	Proton-proton distance rP (Å)
0	0.010	1.38	0.042	1.91
1	0.010	1.42	0.043	1.96
2	0.011	1.39	0.047	1.92
3	0.012	1.44	0.045	1.98
4	0.011	1.44	0.044	1.97
6	0.010	1.44	0.040	1.98
7	0.010	1.44	0.040	1.98
11	0.011	1.46	0.047	2.00

As shown in Tables 6.6.1, 6.6.2 and 6.6.3 Gaussian relaxation times for both components and their proton-proton distance seem not to change through drying and it seems that it does not depend on the type of drying.

Figure 6.6.3 shows the evolution of the signal intensity (in percent respect to the total solid signal) of the two components T_{gE} and T_{gP} for the WPC sample (0.5 w/c) dried in RH controlled conditions.

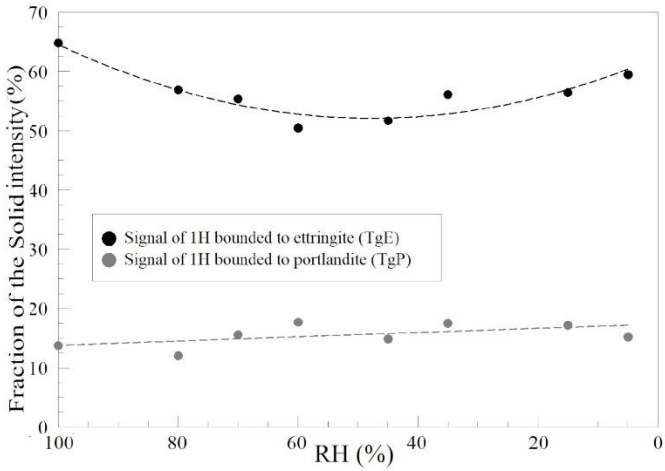

Figure 6.6.3 - Evolution of the signal (in percent) of the two components belonging to the SL signal, characterized by the two Gaussian times T_{gE} (Ettringite) and T_{gP} (Portlandite), through drying at controlled RH. Dashed lines are trend curves.

Very similar behavior of a solid component, assigned to Ettringite for samples dried in the oven in Figure 6.6.4 was observed.

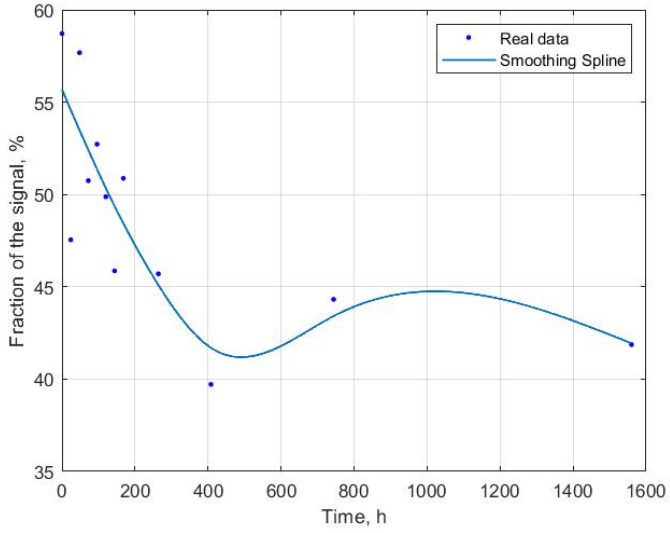

Figure 6.6.4 - Evolution of the signal (in percent) of the component belonging to the SL signal, characterized by Gaussian times T_{gE} (Ettringite) through oven-drying. Dashed lines are trend curves.

6.6.2. Quadrature Echo measurements

For all dried samples used for the analysis of the solid component also a QE analysis was performed for comparison with Pake-Doublet analysis. Unfortunately, QE method does not allow to distinguish two SL populations, as well as to separate SL and SS components.

In Figure 6.6.5 the evolution of the solid signal (normalized intensity in respect to the total QE signal (a), and T_{gQE} (b)) through drying at controlled RH obtained by the QE measurements is shown.

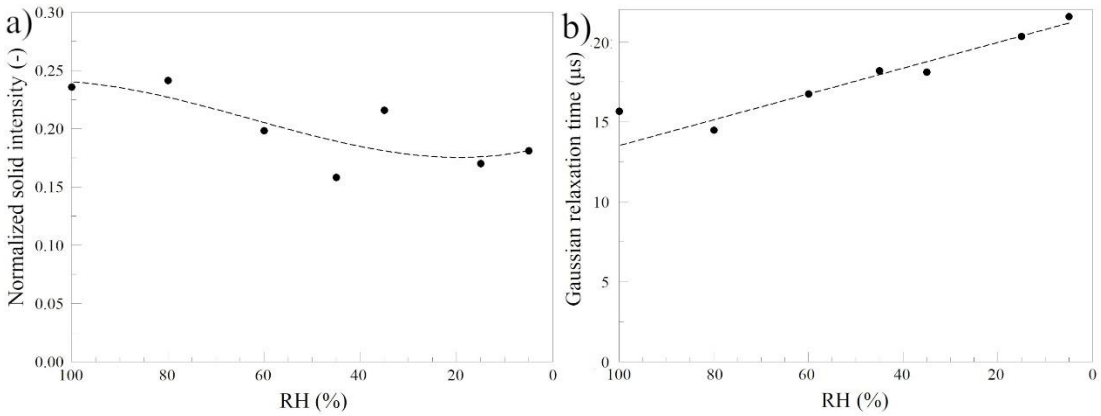

Fig. 6.6.5 - Evolution of the solid signal of cement through drying at controlled RH from QE measurements, a) normalized signal intensity, b) Tg_{QE}.

6.7. Comparison with other technique (MIP)

MIP measurements of the WPC samples of a 0.5 w/c ratio were done for the comparison with NMR technique measurements.

In Figure 6.7.1 pore size distribution of 0.5 w/c WPC sample is shown.

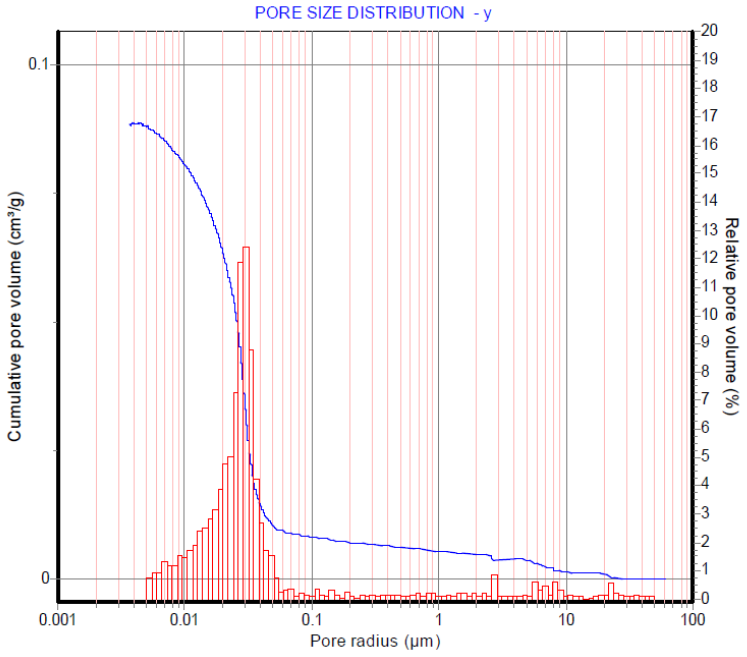

Figure 6.7.1 - Pore size distribution, done with MIP measurement on 0.5 w/c WPC sample.

7. One-sided magnet design

In addition to the planned activities, part of the work (performed together with another ESR of the ERICA project) was devoted to developing a prototype end-user MR magnet for in-situ use (in the built environment).

The background idea was to create a bespoke single-sided NMR instrument for the construction sectors to move the materials characterisation techniques from the academic laboratory to the cement manufacturer for product development. The desired characteristics for the unilateral magnet were to have as large a homogeneous region as possible positioned as far as possible from the top surface of the magnet. In particular, we have collaborated extensively on the aspects related to the magnet and coil design.

7.1. Design of the magnet-Finite element method model

Magnet design was based on Fukushima and Jackson patented (US Patent US6828892) [137]. The whole set-up is composed of a barrel magnet (outer magnet) with a centred movable bar magnet inside (inner magnet), consisting in total of about 450 individual cubic magnetic blocks. NdFeB was chosen as magnetic material for the 1 inch^3 (16.39 cm^3) blocks.

The calculated magnetic field strength along the bar and barrel magnet's axes of symmetry (z axis) adapted from ref.138 is shown in Figure 7.1.1.

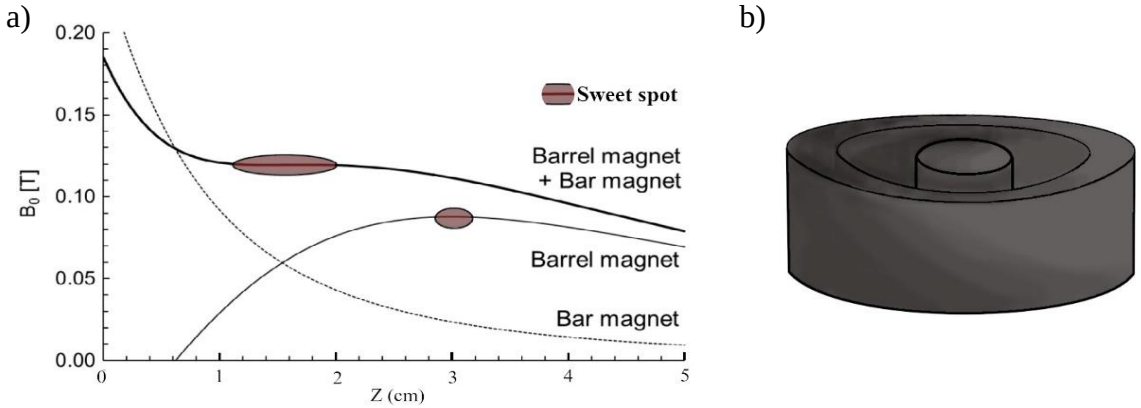

Figure 7.1.1 – Bar and Barrel magnet: a) graph of the magnetic field strength vs the distance along the magnet axis of symmetry (z axis), adapted from [138], b) Barrel magnet with a bar magnet inside

As it is shown in Figure 7.1.1(a), the magnetic field of the bar magnet monotonically decays with distance. Instead, the field of the barrel magnet shows a small uniform peak region (sweet spot). By the use of these two magnets aligned symmetrically (Figure 7.1.1(b)) a sweet spot that is a saddle point of a magnetic field could be created, where the first two derivatives

of the magnetic field are nulled. Axisymmetric position of the magnets contributes to the increase of the intensity of the filed in the direction parallel to the axis. Thus, if barrel and bar magnets are combined it is possible to select a position of the inner bar magnet that increase B_0 strength and improves uniformity around the sweet spot, although the sweet spot moves closer to the magnet compared to the plain barrel magnet. By varying position of the bar magnet, it is possible to control the field profile: modify the sweet-spot size and the field strength.

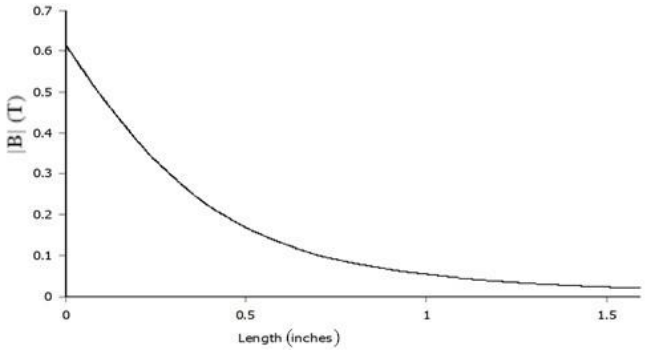

Figure 7.1.2 - Magnetic field strength as a function of distance from the one magnetic block N52 (consider z axis as a vertical line of symmetry of the magnetic block).

Firstly, a single magnetic block was studied. Figure 7.1.2 shows the plot of the magnetic field strength against the distance from the top of one magnetic block N52 computed with FEMM. At the distance of 1.5 inches from the top surface the magnetic field is of 0.019 T.

To verify FEMM results, a comparison with reported data from literature [139] was performed. In Figure 7.1.3 the plot of the magnetic field at the top of a N52 block for simulated (theoretical) and measured results are shown, but using a block of different size ($V=0.75$ inch^3 $\approx$ 12.3 cm^3). For an accurate comparison, one should consider the differences in the size of magnetic blocks. However, the theoretical curve in Figure 7.1.3 is similar to that shown in Figure 7.1.2, and therefore the result can be assumed significative.

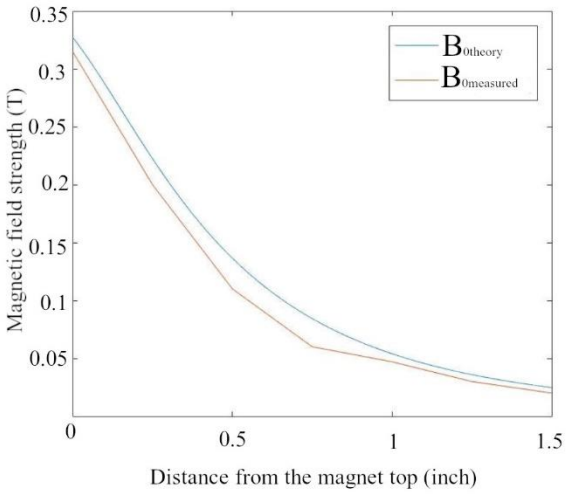

Figure 7.1.3 - Magnetic field strength as a function of distance from the N52 block surface, computed (blue line) and measured (yellow line), adapted from [139].

Moreover, measurements of the magnetic strength with the use of Fluxgate Magnetometer, showed around 0.019 T at the distance of 4 cm (≈1.57 in) from the top of a magnet block, which is in a pretty good agreement with the values reported in Figures 7.1.2 and 7.1.3.

In the first tentative the magnet frame design was approached with FEMM. Different designs – height (vertical number of cubes), diameter (number of cubes in the outer magnet), number of rings used for the outer magnet and the distance between inner barrel and outer bar magnet, were tested.

In Figure 7.1.4 a tentative design, with different possible assemblage of magnetic blocks, are shown with the according calculated proton NMR frequency.

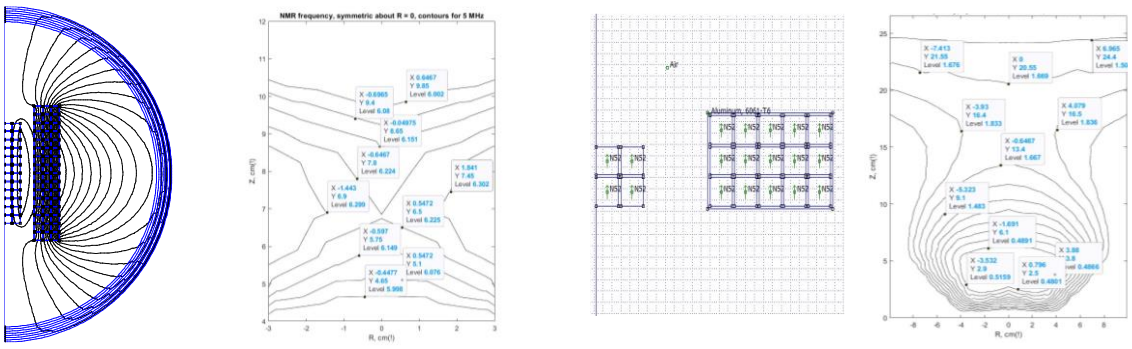

a) b)

Figure 7.1.4 - FEMM design of the bar-barrel magnet, where a)16 magnetic cubes and b) 3 cubes were positioned along the vertical.

In order to compute the direction of a magnetization vector *B* respect to the z direction, and to analyse the homogeneity of the field, the spread of the *B* orientation α angle has been computed:

$$\tan \alpha = \frac{B_r}{B_z} \tag{7.1.1}$$

where B_r is the radial magnetic field and B_z is the longitudinal magnetic field component along the z axis. The magnetization vector orientation is plotted against the z position (see Figure 7.1.5).

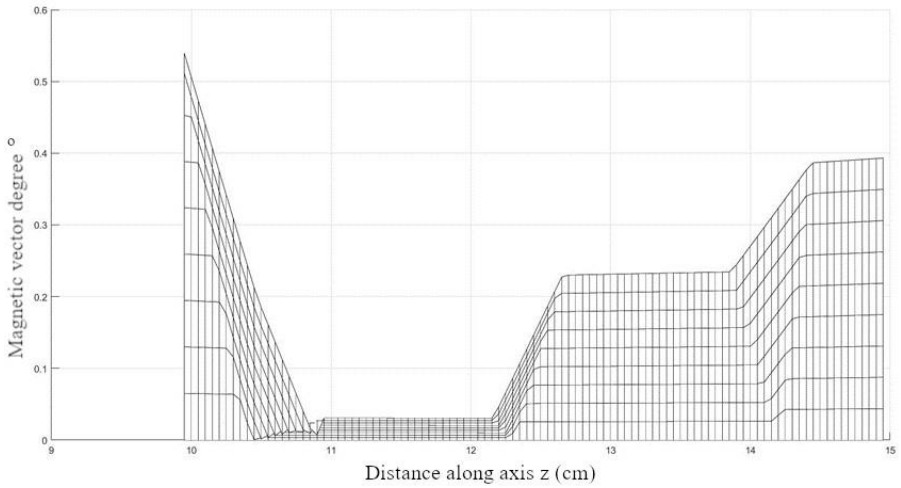

Figure 7.1.5 - B_0 magnetic vector orientation at different position along the z axis.

To compare the previous results, Ansys software was used with the same geometrical arrangement. In Figure 7.1.6 magnetic field strength at the 6 cm distance from the top of the outer magnet is shown.

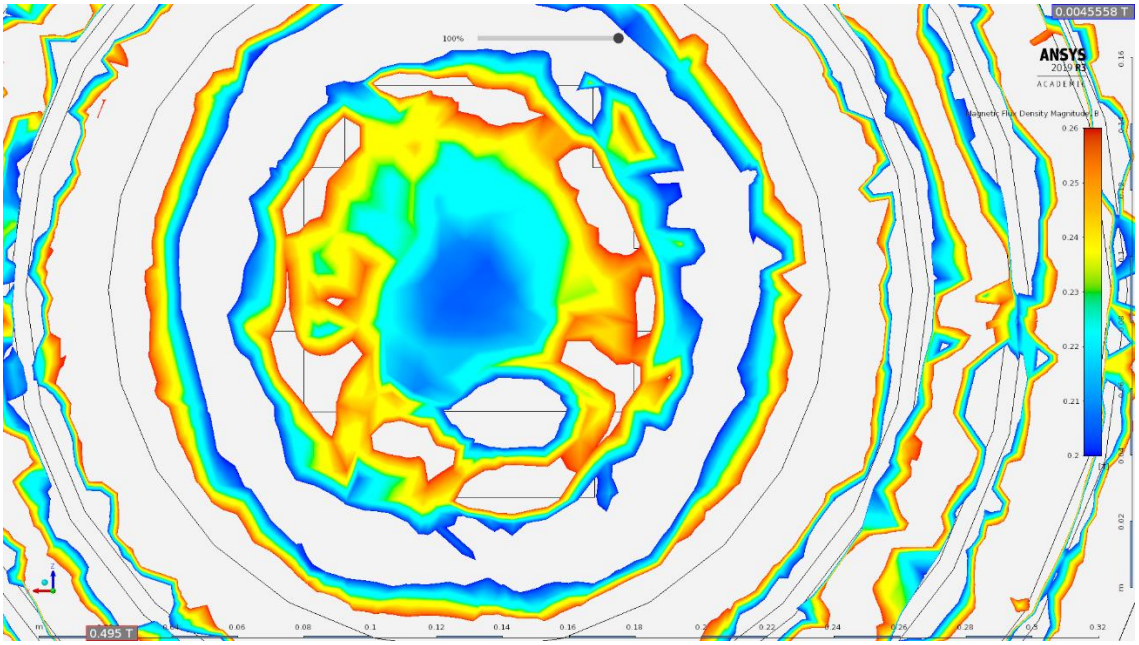

Figure 7.1.6 - Magnetic field strength distribution as computed with Ansys software.

A 2D projection trend of the proton NMR frequency (^{1}H Larmor frequency) distribution on a plane orthogonal to z axis at 6 cm from the upper top of a barrel magnet is shown in Figure 7.1.7.

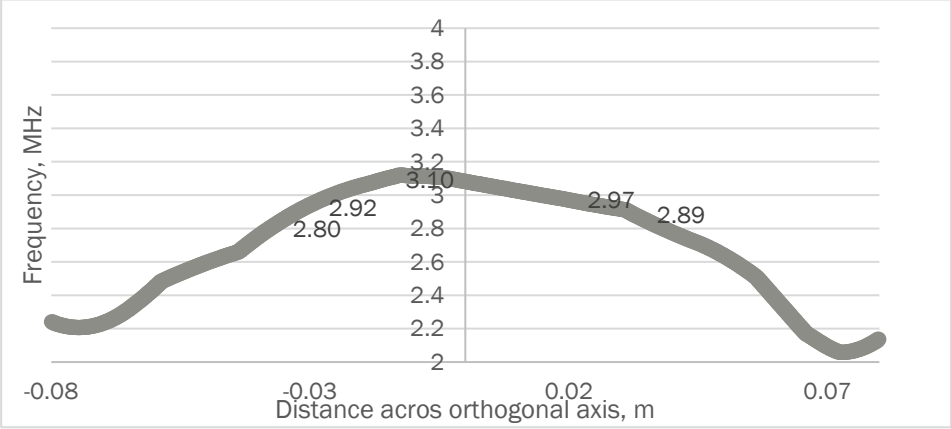

Figure 7.1.7 – A trend of the proton NMR frequency distribution around the symmetry z axis at 6 cm of distance from the top surface of the outer magnet.

As seen in Figure 7.1.7 and 7.1.6, with such arrangement of the magnetic blocks, it was possible to obtain a relatively high frequency (at around 3MHz) and homogeneous sweet spot of circa 4 cm in diameter.

The trend of a magnetic field strength as a function of a distance along the z axis from the top surface of the magnet as calculated by Ansys software is shown in Figure 7.1.8, where

it is possible to see that from around 7 to 12 cm, the magnetic field is pretty homogeneous with an NMR Frequency of around 2 MHz.

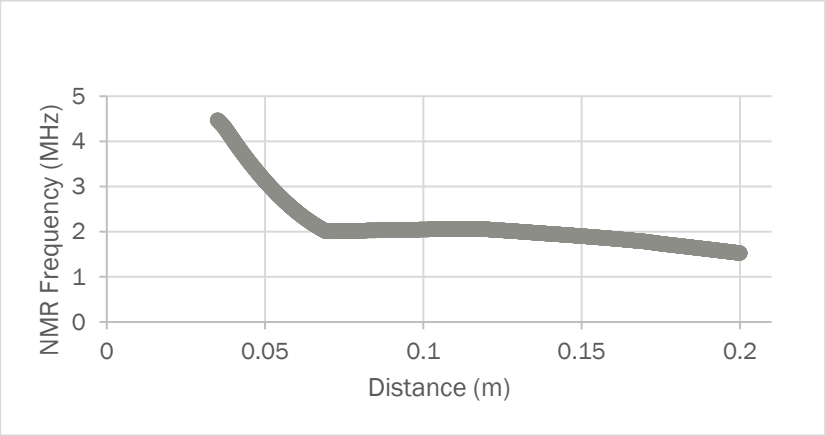

Figure 7.1.8 - NMR frequency as a function of distance from the top of a magnet.

Similar results using COMSOL software [140] were obtained during the secondment at MR solution.

In Figure 7.1.9 the top view of a possible setup computed and shown by means of Ansys software is shown.

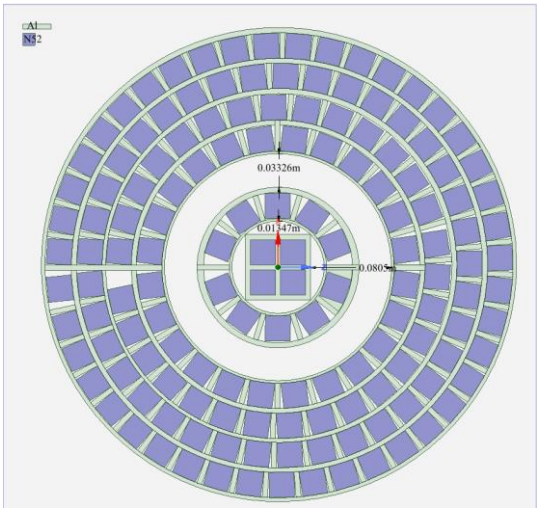

Figure 7.1.9 - Top view of the estimated design for the magnet, done with 320 N52 blocks, created with Ansys software, where olive colour are Al layer separator sheets of thickness 0.5 cm.

The computed spatial distribution of magnetic field and the preliminary magnet setup we designed were in a very good agreement with the ones done by ESR 5. Based on these findings the final CAD design of the magnet was performed by engineers at MR Solutions and is shown in Figure 7.1.10a. It consists of three outer layers (plates) each of 4 concentric rings, with the inner cylinder done by two plates with blocks positioned to get the most symmetrical form.

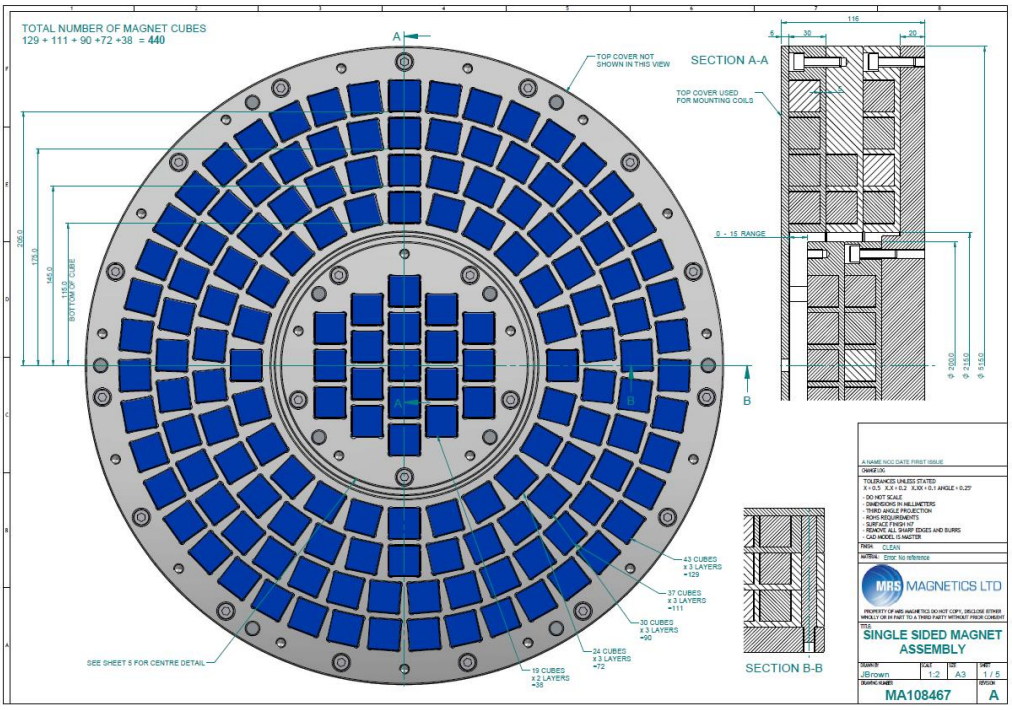

Figure 7.1.10a - The final CAD design of the designed permanent magnet.

As the plates and rings must be separated by aluminum separators, it was crucial to calculate the pulling forces of the whole assembly to understand how aluminum will be deformed by these forces.

This analysis is also fundamental to understand the best way to assemble the magnet, and if it could be assembled "by-hands" or some specific device should be used.

By the use of Ansys it was calculated that the pulling forces of the whole assembly is around 5 kN, as shown in Figure 7.1.10b.

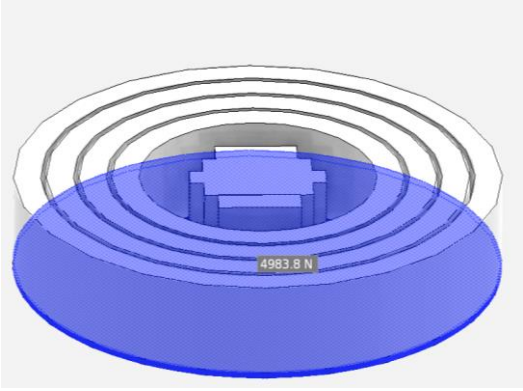

Figure 7.1.10b - Pulling force of the whole permanent magnet, occurring on the metal frame (highlighted in blue) computed by Ansys.

In Figure 7.1.10c plot of the pull forces for different distance from the top of the inner magnet is shown.

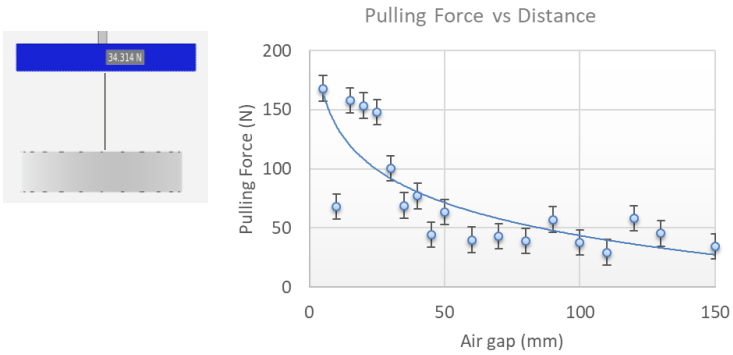

Figure 7.1.10c - Pulling force of the magnet set up as a function of the distance from the top.

As pulling forces among blocks were pretty high, a specific assembly tools (shown in Figure 7.1.11) were created and used.

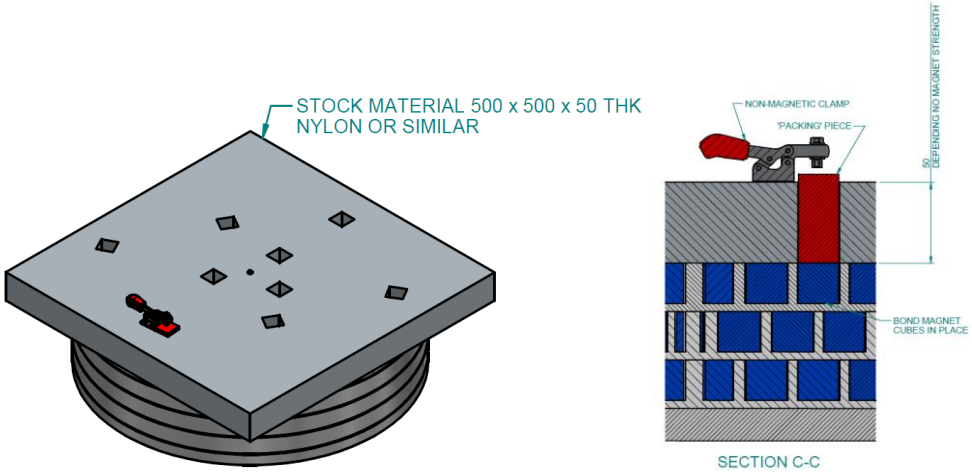

Figure 7.1.11 - Assembly tools for the magnet construction (image done by engineers in MR Solutions).

Magnetic field strength of the assembled barrel magnet was measured and the results, shown in Table 7.1.1 and Figure 7.1.12, are in a good agreement with the one found by mathematical model. The field is calculated from the Perspex top (7 mm in thickness) which is covering the assembled magnet.

Table 7.1.1 Magnetic field strength along z axes from the top of the Perspex cover.

Relative depth (cm)	Field strength (mT)	^{1}H Frequency (MHz)
1	164	6.98
2	113	4.81
3	98	4.17
4	81	3.45
5	78	3.32
6	71.2	3.03
7	66	2.81
8	62	2.64
9	58.5	2.49

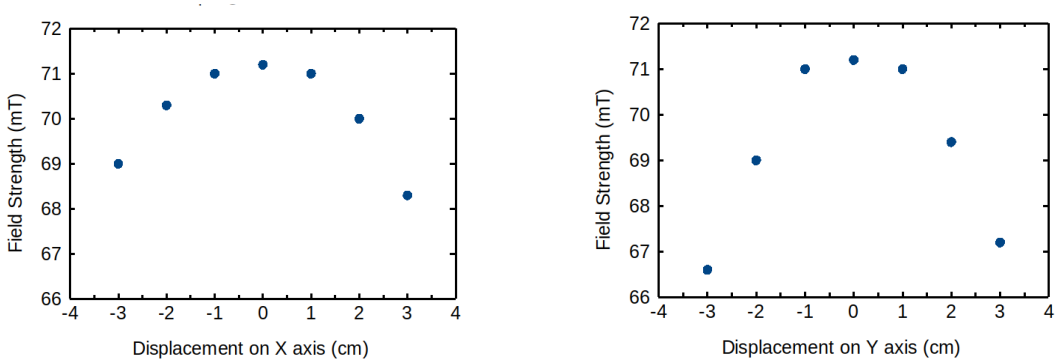

a) Magnetic field strength along X-Z plane b) Magnetic field strength along Y-Z plane

Figure 7.1.12 - Magnetic field strength at the 6 cm depth along X-Z and Y-Z planes.

As it possible to see in in Figure 7.1.12, the measured magnetic field had a homogeneous area of around 2-3 centimetres along X and Y axes.

7.2. Magnetic flux density model of r.f. coil

As it was explained in the paragraph 4.4 and more specifically in 4.4.7.2, where the geometry of the coils for one-sided magnets were discussed, the coil plays an important role in every NMR experiment as it serves to send the rf pulse and detect the NMR signal (in some cases NMR apparatus could have two separate coils for these purposes).

Magnetic fields of the coils with different geometries, located on the upper face of inner cylinder, were calculated with a self-modified version of Biot-Savart magnetic MatLab toolbox (see Appendix B for the developed Matlab code). In paragraph 4.4.7.3, the Biot-Savare law was explained. Regarding the specific geometry of spiral-shaped wire with one filament, the application of the law yielded following equation:

$$B = \frac{\mu_0 I}{4\pi} \int \frac{ds \times (R - r)}{|R - r|^3}, \tag{7.1.2}$$

Where *R* is the vector pointing to the point in which magnetic field is calculated and *r* is the vector pointing to the centreline infinitesimal element *ds* of the coil conductor.

Results of a RF magnetic field calculation for the coils of a different geometry (in "infinity symbol" shape) are shown in Figure 7.2.1.

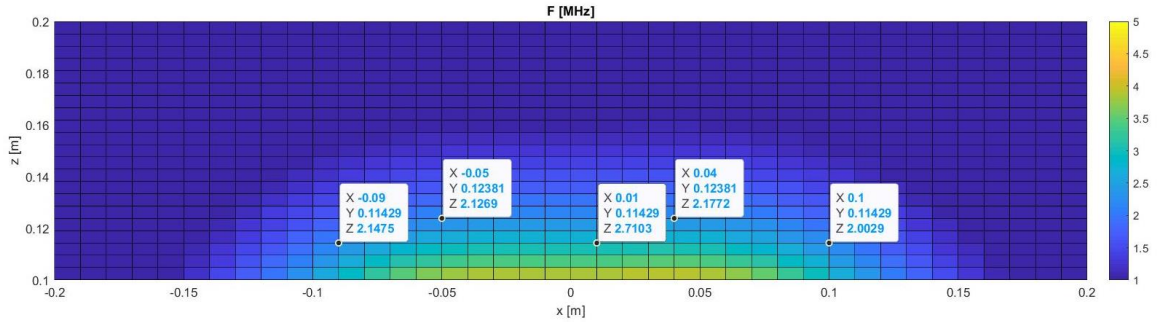

Figure 7.2.1 - X-Z axis slice of NMR Frequency calculated for the coil geometry in "infinity symbol" shape, computed with Biot-Savart magnetic MatLab toolbox.

From Figure 7.2.1 it is possible to see that the field has pretty large homogeneous zone along *x* and *y* axis at around 1 cm along *z* axis.

Alternatively, also the RF field for a coil made up of two square-shaped wires was calculated. The resulting NMR frequency is shown in Figure 7.2.2 a), b) and c).

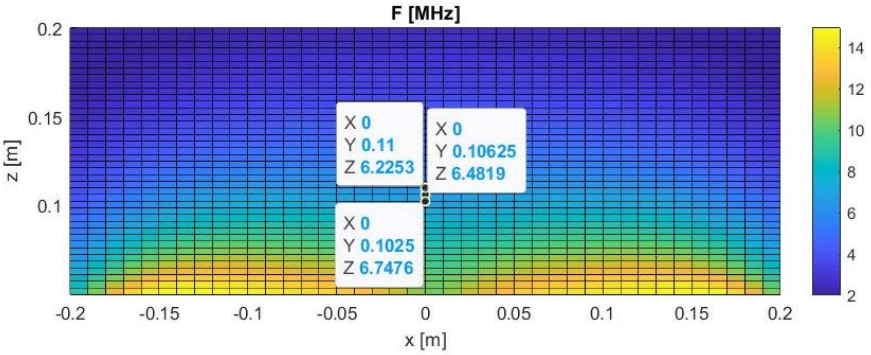

a) NMR frequency displayed on the Z-X slice (passing through the origin of the Y axis).

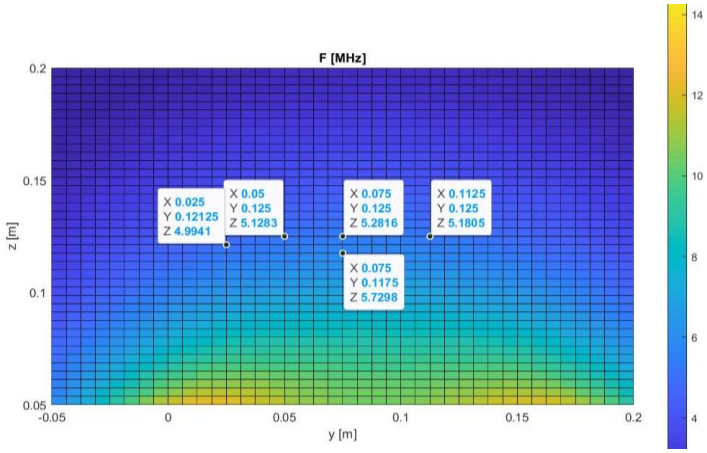

b) NMR Frequency displayed on the Z-Y slice (passing through the origin of X axis).

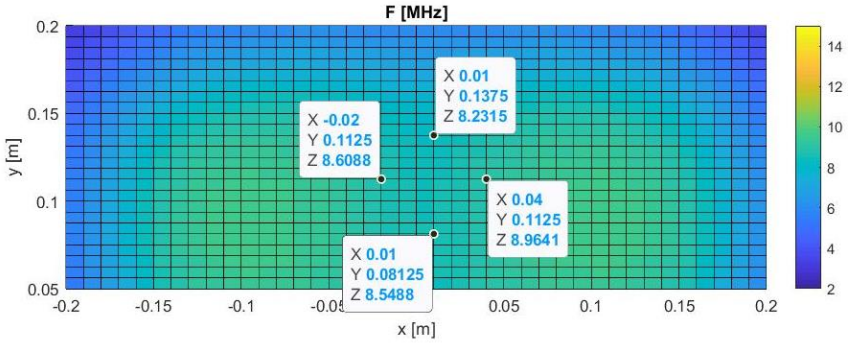

c) NMR Frequency displayed on the X-Y slice located at 8 cm from the magnet top surface.

Figure 7.2.2 - NMR Frequency calculated for the coil consisted of two square shaped wires with different axis views.

Simulation results we obtained were in good agreement with those obtained by ESR5. The final design implemented in the built uniliteral magnetic was a two wires square spiral coil as it showed a good homogeneity, and it is relatively easy to construct.

7.3. First cement samples measurements with one-sided set-up

The whole set-up – permanent magnet with the coil, spectrometer with amplifier were tested with cement sample hydrated for 13 hours, done in University Surrey by Dr. P. Mcdonald and A. Gajewicz (private communication). Figure 7.3.1 shows measured raw CPMG data and echo attenuation data.

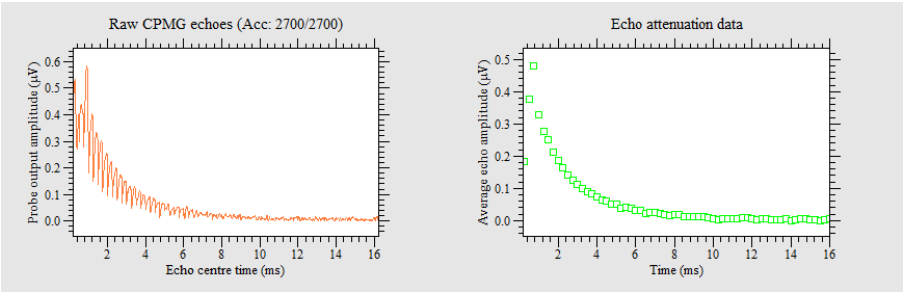

Figure 7.3.1 - Raw CPMG data, measured with one-sided set-up on cement paste hydrated for 13 hours.

In Figure 7.3.2 processed T_2 distribution of the same sample is shown.

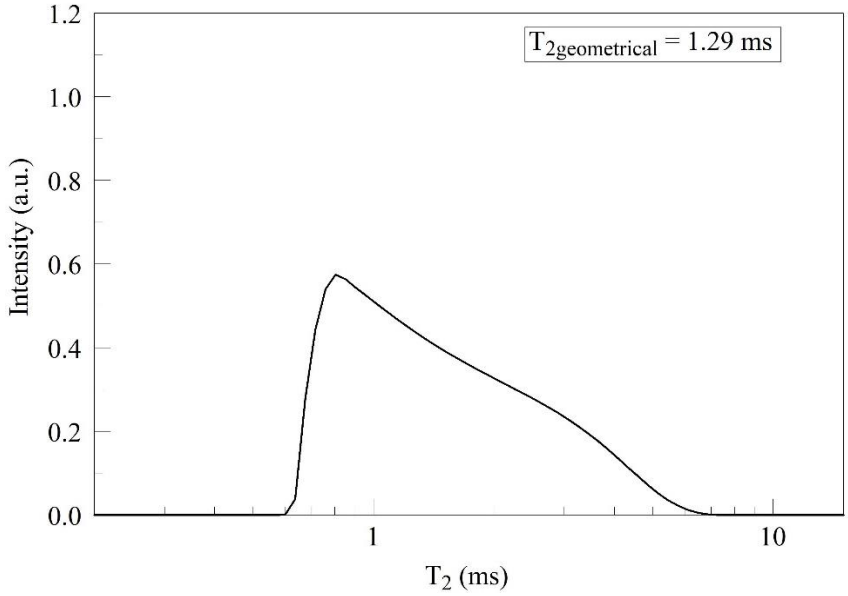

Figure 7.3.2 - T_2 distribution of a cement past, hydrated for 13 hours done with the use of one-sided set-up.

Here, the geometric-mean T_2 values was used for the description, because we have a continuous broad distribution of T_2 value.

8. 2D NMR measurements

In this chapter we show some first results from 2D NMR experiments on cement samples. We show T_1-T_2 measurements of as-prepared 0.5 w/c cement samples and compare results with one, published previously. Additionally, by T_1-T_2 measurements we observe cement structural changes through first sorption cycle. We believe that such observation has not been done previously.

8.1. As-prepared 0.5 w/c WPC

For 2D NMR measurements, samples shaped as disks were prepared and hardened under water. Several measurements were performed and only the most representative results are shown in this Chapter.

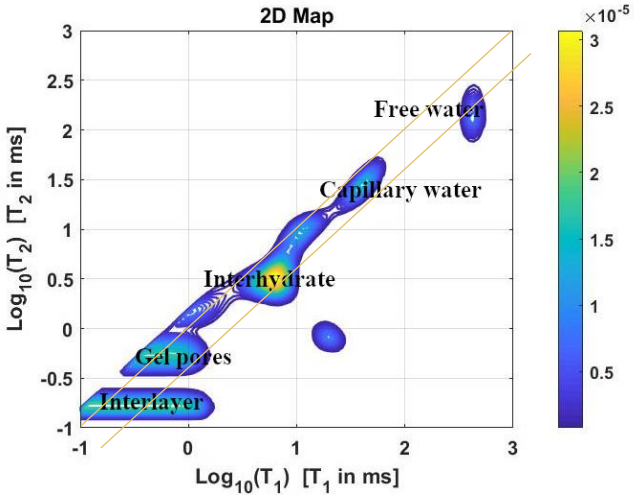

Figure 8.1.1 - T_1-T_2 map computed with Upen2D of the as-prepared WPC sample of 0.5.

A 2D map of the T_1-T_2 correlation function is shown in Figure 8.1.1, where at least 5 components could be distinguished. From the left-bottom to the top-right corner, the components are: interlayer water, gel pores, interhydrates, capillary pores and bulk water (in big cracks or voids). Following diagonal lines depicted in Figure 8.1.1, some components are shifted from the main diagonal (T_1/T_2 = 1) to T_1/T_2 ~ 3, independently of pore size. A good agreement was determined by comparing these results to the ones obtained by C. Cadar et al. [141], as shown in Figure 8.1.2 by a T_1-T_2 map of an as-prepared WPC sample. Samples used in the experiments were different by the w/c used, in the Cadar et al. experiments w/c was 0.3, which should influence the amounts of different pore types, but should not affect T_2 and T_1 values and T_1/T_2.

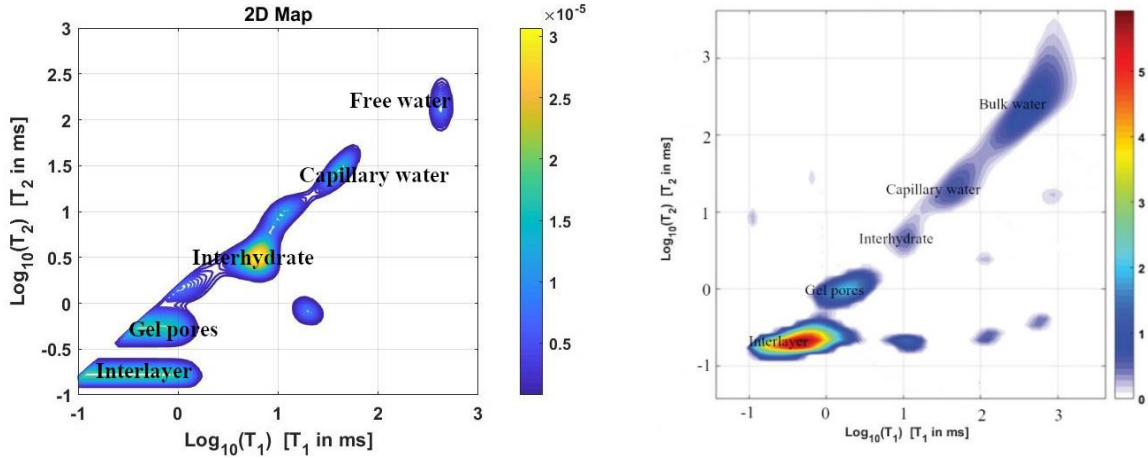

Figure 8.1.2 - T_1-T_2 map of an as-prepared WPC sample, w/c = 0.3, done by C. Cadar et al. (right), and comparison with the T_1-T_2 map done in this work (left).

8.2. Evolution of the 2D NMR maps data through re-saturation process

Figure 8.2.1 shows eight 2D maps of data acquired during the re-saturation process of the WPC samples by SR-CPMG measurements (at 1, 3, 5, 32, 68, 317, 749 and 821 hours). Due to the low SNR and the difficulties to select the correct sequence parameters for T_1 measurements of the dry sample, it was not possible to construct a full T_1-T_2 map for the dried sample. Anyway, it was possible to extract CPMG data from the measurements and by UpenWin inversion, treating the extracted data as 1D, we were able to have a T_2 distribution. In this way it was possible to observe that only interlayer water was left after drying. It was not possible to directly compare the amount of signal left. But, by comparing the previous measurements performed during this work, one can compute the amount of interlayer signal left that was around 15% (Figure 6.5.7). Regarding existence of the off-diagonal peak for as-prepared sample (Figure 8.1.2) it might be that the same peaks for re-saturated state indicate exchange of liquid, but the possibility of the inversion problem could not be excluded due to the low SNR. Further experiments are needed to corroborate these results.

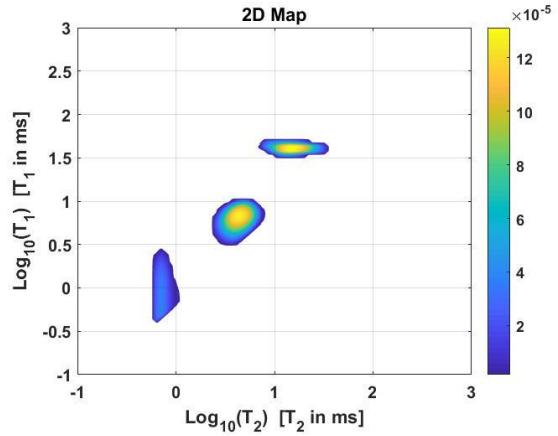

Re-saturated for 1 hour.

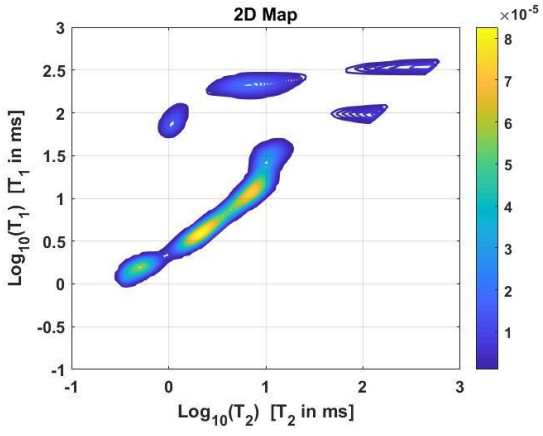

Re-saturated for 3 hours.

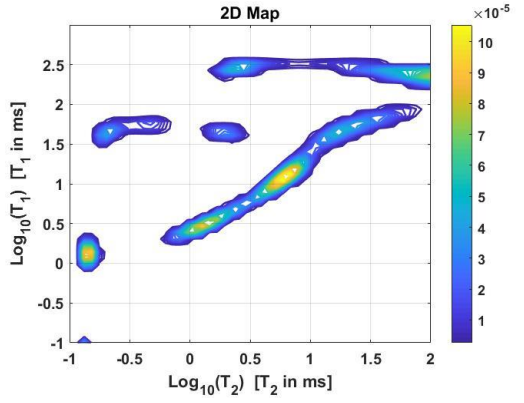

Re-saturated for 5 hours.

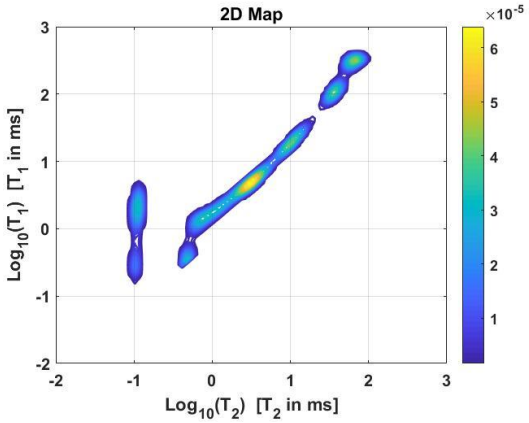

Re-saturated for 32 hours.

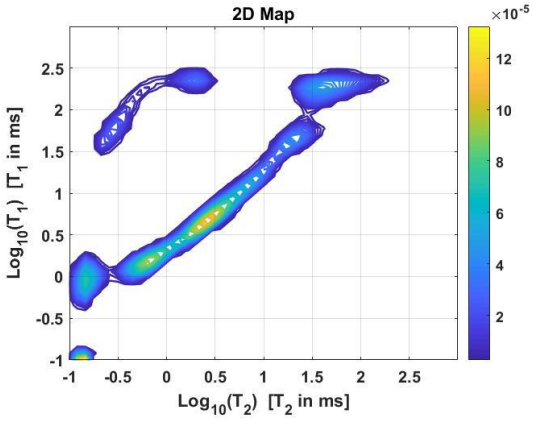

Re-saturated for 68 hours

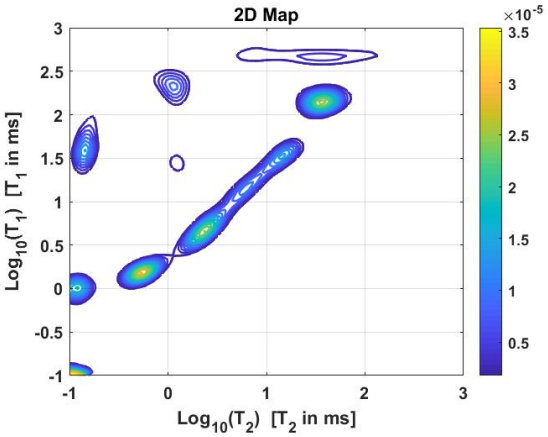

Re-saturated for 317 hours

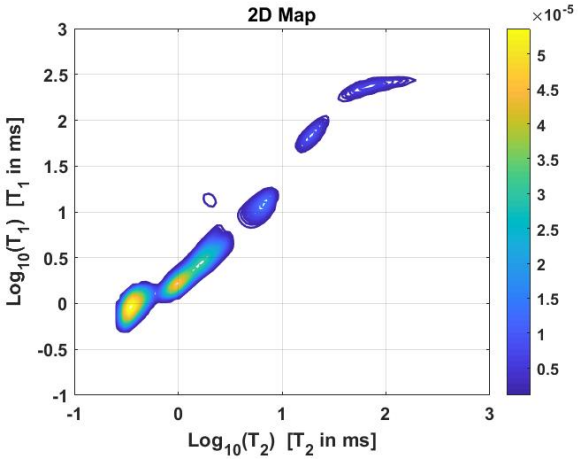

Re-saturated for 749 hours.

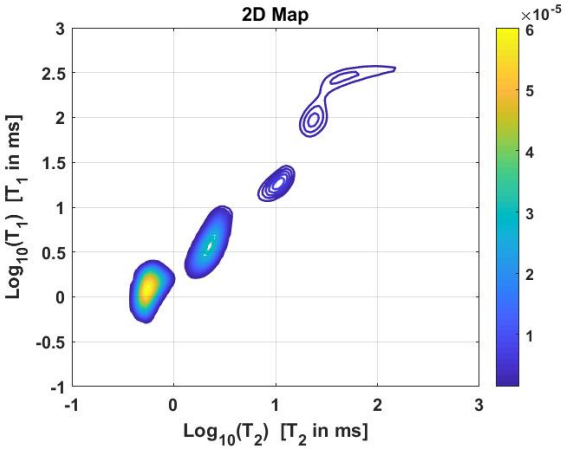

Re-saturated for 821 hours.

Figure 8.2.1 - T_1-T_2 maps of WPC sample 0.5 w/c through re-saturation process.

Figure 8.2.2 shows T_1-T_2 3D maps in different view. In these graphs T_1 axis is not visible due to the chosen view. This helps to look at the variations of T_2 distribution related to porosity changes during the re-saturation process. Numerical data in the insets (blue font colour) are X: T_2 values - $Log_{10}(T_2)$, Y: T_1 values – $Log_{10}(T_1)$ and Z: Signal density in a.u.

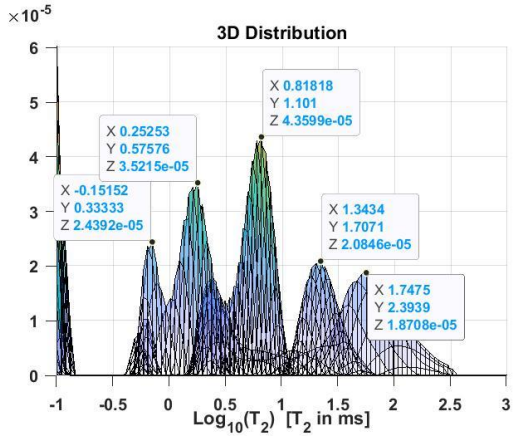

Re-saturation 5 hours

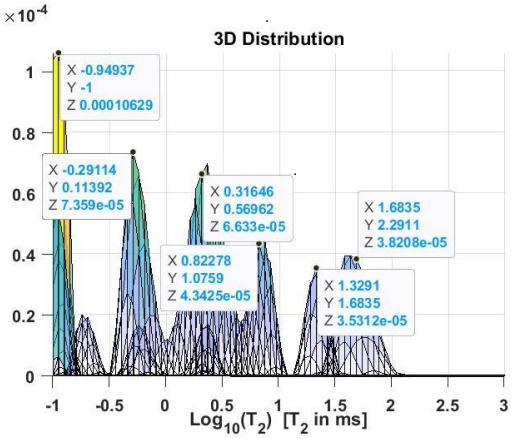

Re-saturation 68 hours

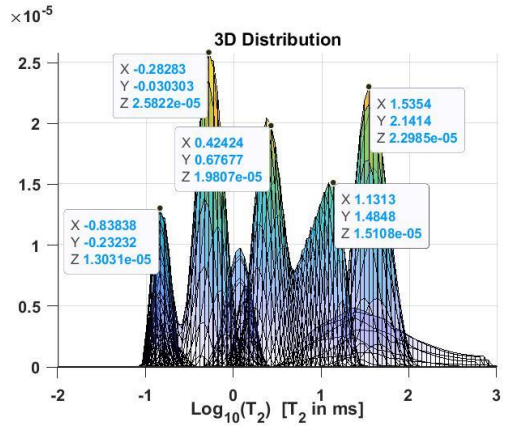

Re-saturation 317 hours

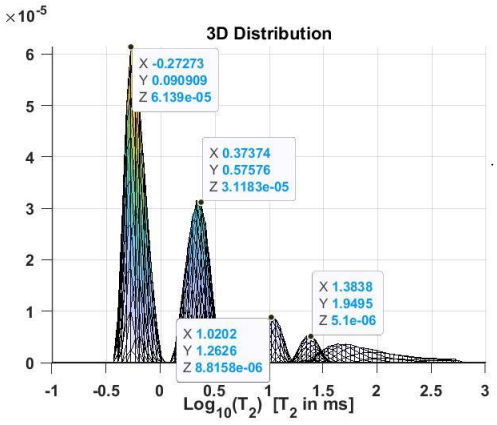

Re-saturation 821 hours

Figure 8.2.2 - T_1-T_2 3D maps of WPC sample 0.5 w/c through re-saturation, different axis view.

In Figures 8.2.1 and 8.2.2 not all performed T_1-T_2 experiments are shown, but only that with which it was possible to observe changes of the porous structure through re-saturation process. In between time of showed results changes of the structure were mild.

9. Discussion of the Results

In this paragraph, we discuss in detail the results of the experiments, shown in paragraphs 6-8. Discussion follows the same order as in paragraph 6: firstly, we discuss NMR experiments on the cement samples during early hydration and then as-prepared samples, followed by the discussion of sorption cycles of cement samples.

In the two final parts, we discuss one-sided set-up construction and 2D NMR experiments accordingly.

9.1. Pore structure development through hydration

Even though the difference between 0.5 and 0.4 w/c ratios is not very big, we still found differences in the hydration process for these samples. Samples with a larger gap between w/c ratios should be tested in the future.

The total measured signal intensity decreased slightly over time. As the decrease was constant, and we did not observe oscillation of the signal intensity, it is safe to assume that the signal intensity decrease is a physical phenomenon and not due to some instrumental effect.

It should be noted that the results seem to be in good agreement with the ones obtained by the ESR2 of the ERICA program and shown in Figure 6.1.2.

For the WPC samples, as it is shown in Figures 6.1.1 and 6.1.5, in the first 10-20 minutes of the hydration process there is only a peak around 5-8 ms which, at this hydration stage, is attributed to the capillary pores that is interstitial water between the clinker grains. But with longer hydration time it evolves to become interhydrate water, which is seen as the peak moves to the shorter T_2 time. From the beginning of the hydration process, a shoulder to the lower relaxation times (around 1 ms) was seen, which appeared as a separated peak at later hydration time (60 minutes and more) and might indicate forming C-S-H gel pores. It was clearly separated for w/c 0.5 sample and not for 0.4 w/c sample which is attributed to data processing and not to a real physical phenomenon. At 48 hours, a clear separation of the interlayer water signal was seen for w/c 0.5, with the remaining signal represented by gel pores and small amount – capillary water (at $\approx$ 60 ms, not shown in Figure 6.1.1).

To change the rate of the hydration process, some additives to the cement powder might be used. Additives could alter the porosity and pore size distribution of the cement. It was found by Wild [142] that the small amount of added gypsum results in the increase of compressive strength, but excess of it results in fall in strength and in reduced overall porosity, as well as increased pore size resolution. Previously, by A. Bentur, who studied how gypsum influences

hydration of the pure CS_3, it was reported that added gypsum accelerates the hydration of silicon phases [143]. By our results, we observed that smaller pores for the samples with additional gypsum (Figure 6.1.4) were formed faster than for WPC samples (Figure 6.1.1 and Figure 6.1.5). As shown in Figure 6.1.1 and Figure 6.1.2, ordinary WPC sample only at 1 hour of hydration demonstrated clear gel-interlayer pores separation in contradiction to WPCG sample, in which such separation was observed in the first 20 minutes of hydration process, which suggests an acceleration of the hydration by gypsum.

The biggest difference between all the samples is the time of interlayer space formation. As seen, in the WPCG sample, interlayer spaces started to form at early hydration time, already at 150 minutes of hydration (Figure 6.1.4), the peak with T_2 corresponding to the water of interlayer spaces (around 150-190 μs) was observed. For the WPC samples of w/c ratio 0.4, the first time any signal resembled that of interlayer water was visible at 240 minutes, with a distinct peak at 24 hours (Figure 6.1.5). Whereas, in the 0.5 w/c WPC it appeared at around 48 hours (Figure 6.1.1). This difference between 0.4 w/c and 0.5 w/c could be explained by that when bigger pores, such as interhydrate and capillaries, were formed, available water was still present for 0.5 w/c, while for 0.4 w/c ratio, as there was less available water, interlayer spaces start to form earlier.

9.2. As-prepared samples

Regarding the T_2 distribution of all cement samples, WPC with different w/c and WPCG, the porous structure is very similar, especially in w/c 0.5 and WPCG samples. The reason is that the amount of gypsum accelerated the interlayer space formation, but did not change the porous structure very much. The small difference we observed might be merely due to the degree of processing accuracy of these noisy data.

The difference in the amount of interlayer space and gel pores was observed between 0.5 w/c and 0.4 w/c WPC samples. As can be seen from Figure 6.2.4, WPC with 0.4 w/c does not have capillary pores of an order of 100 ms, which were present in the sample with 0.5 w/c (Figure 6.2.1). The distribution shows only some components of small intensity around 5ms and 60ms (not shown in Figure 6.2.4), which might be due to the smaller amount of added water, not enough to feel larger spaces or pores. Another difference with the 0.5 w/c samples is the higher percentage of interlayer spaces and smaller percentage of gel pores.

From the comparison of Figure 6.2.5 and 6.2.2, differences were observed as well for T_1 distributions. The main peak, which is most probably composed of two not separated

components – gel pores and interlayer water- has the same shape, though shifted to the left – toward shorter relaxation time- for 0.4 w/c sample, as it might be that amount of interlayer water exceeds the amount of gel pore water. The shoulder to the right of the main peak as well is shifted to the left for 0.4 w/c sample and the area below the longest relaxation time (capillary water) is smaller as well as its T_1 value. The results are in good agreement with the literature and T_2 measurements – 0.4 w/c WPC showed a larger amount of smaller pores.

Regarding the results of the QE measurements performed on all kinds of samples, there was not a big difference among them, as expected.

Comparison of the two different data processing methods.

From Figure 6.4.1 and Table 6.4.1 one can see that the results were in a pretty good agreement regardless of the method used. The few differences were that the multi-exponential fitting was greatly improved by assuming three components, whereas linear continuous fitting (UpenWin) showed 4 components. Another difference is that multi-exponential fitting tended to compute more interlayer space than continuous fitting. The T_2s were in the same range, even if some difference is present because T_2 values of the peaks computed from quasi-continuous distributions are geometric-mean values times.

A comparison of the T_2 data obtained in this work with other found in the literature was also performed (see Table 6.2.1). The data in Table 6.2.1 were obtained by assuming the hypothesis that there is a discrete number of components each with its characteristic T_2, and computationally separable. On the contrary, the UpenWin approach assumes a quasi-continuous distribution of relaxation times, based on the idea that each component can have a distribution of relaxation times and, more than that, the T_2 of two adjacent components can partially overlap. The peak and the shoulder in the distribution shown in Figure 6.2.1 could be not separable. Simply the discrete multi-component analysis imposes a hypothesis that the components are separable, with possible resulting distortion of amplitudes and relaxation times, if they were not separable. While it is difficult, if not impossible, to decide what model is true and what is false, what we need is that the two models produce not much unlike results and can be useful to follow the evolution of the systems with the progress of the chemical-physical processes.

9.3. Sorption study

9.3.1. Full RH drying

In our experiments on long sorption process – drying WPC samples by lowering RH and re-saturating with the opposite process – increasing RH- we found that the hysteresis is present through all RH steps for both mass and NMR signal intensity measurements (see Figure 6.5.1). Although after re-saturation the sample mass returned to its as-prepared value, the NMR signal intensity reached only ≈95% of the initial value. This could be attributed to a reduction of the amount of signal detectable by NMR measurements (i.e. part of the water could be no more detectable due to a substantial reduction of its transverse relaxation time, as it might happen for water molecules that turned from liquid to crystalline phase).

It seems therefore that gel pores have undergone irreversible changes. By studying T_2 pore-resolved component intensity evolution (see Figure 6.5.2), we saw that the component intensity of the gel pores was less than for the as-prepared sample after re-saturation, which did not change even for one-week waiting period.

In Figure 6.5.3 b) for re-saturation process, the intensity assigned to interlayer water increased up to 60% RH and decreased after. Later on, it will be shown, that oven-dried samples of the same w/c exhibited the same behavior during re-saturation. But, due to the signal scattering and approximations of the data processing, more investigations will be needed to corroborate the behavior of interlayer water signal.

At the end of the re-saturation process under-water the whole CPMG signal of the cement sample re-established a value comparable with the value of 95% obtained by LAPSR. This result resembles the observation reported in ref. [143]. Moreover, the analysis of the T_2 values (Figure 6.5.4) strengthens these findings. As observed for the component intensity, also the T_2 of interlayer water started to decrease from the initial value of 180 μs (as-prepared value) for the fully saturated sample to 90 μs for 15% RH drying condition. The decrease of T_2 is consistent with the shrinking of the interlayer space. The NMR signal assigned to the bigger pores was negligible below 80% RH.

The behavior of the interlayer spaces during drying and re-saturation may suggest the collapse of the C-S-H sheets during drying. As suggested by the T_2 values, it seems that some of the interlayer spaces could not re-establish back or need some longer time of re-saturation than in these experiments. Such irreversible change of the interlayer spaces that we observed is in good agreement with results from the literature [118].

In summary, the behavior of the interlayer spaces and gel pores suggests irreversible changes in the cement structure when samples undergo long drying procedure.

9.3.2. Partial drying

WPC samples of 0.5 w/c were dried down to 10% RH and immersed under-water for partial re-saturation. From Figure 6.5.5, we can conclude that this drying method influences bigger pores (capillary and voids) and gel pores, but seems to not significantly alter interlayer spaces as the amount of the signal did not change for the dried sample. Most probably we did not observe a difference for the dried sample because of data scattering problem.

The trends for gel pore and interhydrate signals for partially dried samples are in good agreement with other experiments in this work. The time at which the trends became constant is as well similar to other experiments, only the increase and decrease of gel pores and interhydrate were not steep as for fully dried samples, which might indicate that the structure was not modified in the same way. Interlayer water signal, on contrary, shows a different trend, which might indicate structural changes.

Re-saturated sample despite having the same signal amount as as-prepared sample, demonstrated a slight increase in gel pores and interlayer water amount. To verify any results in the case of partially dried samples, more experiments are needed.

9.3.3. Oven drying

WPC samples were dried for up to two weeks and for both 0.5 and 0.4 w/c samples after around 3rd and 4th day the signal reached a plateau and remained constant till the end of the drying process. The difference between 0.4 and 0.5 w/c samples is the amount of interlayer space, as samples with w/c 0.4 show a higher percentage of interlayer water, that is harder to dry out. It may affect the number of days needed to reach the equilibrium. With both w/c samples, the remaining signal consists of the interlayer water, reduced to a similar value, despite the different amount of interlayer water for as-prepared samples, which suggests that the value for interlayer water around 15% of whole water sensed by the instrument is not removable (Figure 6.5.7 and 6.5.10).

The re-saturation trend of oven dried and RH dried 0.5 w/c samples showed similarities. For both kinds of samples, interlayer component slightly increased and decreased through re-saturation. This could suggest interlayer sheets collapse during drying, where in the beginning

of re-saturation process bigger spaces left by collapsed C-S-H sheets were filling with water and started to “un-zip” at some point of re-saturation, with water re-filling smaller spaces. As the data were scattered, it is not possible to make a safe conclusion.

For oven-dried 0.5 w/c sample after re-saturation we found an increased gel pore intensity component compared to its as-prepared state (Figure 6.5.9), which is in contrast with RH-dried samples (Figure 6.5.3), where gel pore signal was less for re-saturated state of a sample. This could indicate bigger structural changes in oven-dried samples, or that the time of re-saturation for RH dried samples was not enough.

Mechanism of re-saturation for 0.4 and 0.5 w/c samples are similar at least, as one can see from the trends in Figures 6.5.8 and 6.5.11 for gel pores, interhydrate and bigger pores. It could be due to the relatively small difference in the w/c value. Therefore, further experiments with the bigger difference in w/c should be performed.

On the contrary, as it is seen for as-prepared sample presented in paragraph 6.2, we observe a different amount of smaller porosity (interlayer spaces and gel pores) for samples of w/c = 0.5 with respect to w/c = 0.4. Samples with w/c 0.4 have larger amount of interlayer water and smaller amount of gel pores compared with w/c 0.5, which is consistent with the literature (see paragraph 4.3.1).

For interhydrate and gel pores, the two kinds of samples seem to have the same time scale for structural relaxation, in fact signals were decreasing and increasing accordingly up to about 192 hours and after they stayed more or less constant. Contrarily, interlayer component for samples of w/c 0.4 seems to take more time to re-establishing, as the value is much smaller at the end of re-saturation than in the as-prepared state.

After re-saturation for both w/c ratios there was less interlayer water signal and more gel pores, and in the case of 0.4 w/c also the interhydrate component changed. By comparing Figure 6.5.12 and 6.5.9, one can see that the difference between as-prepared and re-saturated states are more pronounced for 0.4 w/c sample than for 0.5 w/c sample. The difference might be due to a different time for the structure to relax and since the smaller pores or voids collapsed during drying, it affected more the 0.4 samples due to their bigger amount of smaller porosity.

Comparing Figures 6.5.14 (WPCG) and 6.5.8 (0.5 w/c WPC) and 6.5.11 (0.4 w/c WPC), it seems that the mechanism for re-saturation is different for the WPCG sample, as the trend lines are different. If for WPC samples gel pores component was increasing and interhydrate decreasing, for the WPCG sample it seemed to be the opposite – it decreased and increased accordingly, but only at the beginning of the re-saturation process gel pores and interlayer space components are increasing. Interhydrate pores component for WPCG sample

increased during re-saturation and after circa 120 hours stayed constant. This could suggest that the WPCG samples have different porous structure, or different porous connectivity, or that the porous structure was more disturbed by the drying process than in WPC samples. More experiments are needed to understand structural changes in the case of the WPCG samples.

9.3.4. Changes in solid composition

By the use of UpenWin software it was found that the solid signal of WPC samples appeared to be due to two different components: one with shorter T_1 (solid-short, labeled as SS) of the order of a few milliseconds or less and another one (solid-long, labeled as SL) with longer T_1 of the order of hundreds of milliseconds, which is shown in Figure 6.6.1.

The Pake-Doublet analysis, described in Section 4.4.3 allowed us the find that the SL component is composed of two Gaussian populations with two different T_g values (T_{gE} and T_{gP}), and two different corresponding proton-proton distances, r_E and r_P. Comparing these values of proton-proton distances with previously done work [73], the first component T_{gE} with distance r_E around 1.5 Å was assigned to crystalline water in Ettringite, and the second component T_{gP} with distance r_P around 1.9 Å was assigned to ^1H of $(OH)_2$ groups in Portlandite.

The Gaussian relaxation times and proton-proton distances for samples of 0.5 and 0.4 w/c dried in the oven or by progressively lowering RH seemed not to change and we might conclude that the structure of the solid components did not change through drying cycles regardless of the type of drying or w/c ratio. It should be noted that the difference between 0.4 and 0.5 w/c samples might be too low to draw any conclusion. Further experiments are needed to prove or refute the results.

By studying the solid components of the WPC samples through drying by QE measurements we found that the T_{gQE} increased through drying (see Figure 6.6.5 b). This is in apparent contrast with the results obtained by Pake-Doublet methods. The observed effect might be due to the increase of the SS component, present in larger amount, because the sample was dried and therefore the solid signal was not “covered” by the liquid part of the signal, but not separable from the other solid component through the QE method. The same was observed for the behavior of T_{gQE} in Figure 6.6.5 because, as said before, with the QE procedure it was not possible to separate the signal into SL and SS components and what it is shown is their average Gaussian time. The apparent contrast is resolved if one considers that Figure 6.6.5 a) shows the signal amplitude of the whole solid phase, while Figure 6.6.3 shows the behavior of two separate components.

9.3.5. Comparison with MIP technique

From the MIP measurements, accessible porosity of a sample is ≈15% and inaccessible ≈3%, which is less than what could be found by NMR measurements. It is clear that MIP could not depict interlayer spaces, and the pores that prevail by MIP measurements is of order 20-30 nm, which is by Table 4.5.1 and eq. 4.4.33 the characteristic size of interhydrate pores, with some small distribution over sizes typical for gel pores. On the contrary, by NMR measurements reported in Figure 6.2.1, the biggest signal is from water in gel pores.

9.4. One-sided magnet design

In a first approximation the magnet problem (magnetic field analysis of a set of magnet blocks) was solved by means of a model created with the Free FEM software. As it is possible to see by comparing Figure 7.1.2 and Figure 7.1.3, the theoretical (numerically computed) and measured values of the magnetic field strength were in a good agreement, which means that also the model of a full design should give reliable values.

Different designs – height (vertical number of magnetic blocks, the number of layers), diameter (the radial number of blocks in the outer magnet, the number of rings) were tried for the outer magnet and different relative distance between inner bar and outer barrel magnets.

As it possible to see from Figure 7.1.4 adding more blocks vertically leads to a frequency increase (up to ≈6 MHz), but the volume of the "sweet spot" is low ≈ 7 cm^3 and the design is too heave. By increasing the vertical distance between two magnets (inner and outer), two interesting "sweet spots" with different size and NMR frequencies appears, but the frequency is too low, less than 2 MHz and the design is too heavy and composed of too many magnetic blocks.

Based on the preliminary results, the outer magnet should consist of 3 plates, each made by 4 magnetic blocks along with the diagonal directions (rings) and one inner magnet of cylindrical form, made of two concentric rings. With this arrangement NMR frequency was ≈3 MHz with an oval homogeneous volume of about 35.3 cm^3 (with a maximum Δf=100 kHz).

And as shown in Figure 7.1.8, around 7 to 12 cm from the top of the magnet, the magnetic field is pretty homogeneous with NMR Frequency of around 2 MHz. Similar results were obtained with the use of the COMSOL Multiphysics software at MR Solutions during my secondment.

After more in-depth analysis, in the final CAD design of the permanent magnet set-up, shown in Figure 7.1.10, the outer magnet has 3 plates (layers) each of 4 concentric rings and the inner cylinder done by two plates and blocks positioned as to gain the most symmetric form. Around 450 N52 cubes were needed for the assembly.

By the use of Ansys block pulling forces were calculated as it is crucial information to drive the building process. The value of around 5 kN for the whole assembly was found (the pulling force was calculated as an influence of the whole magnet on a metallic frame), and at MR Solutions it was calculated that an aluminum spacer of 5 mm thickness will be deformed by the 0.1 mm, which is an acceptable value, and a change of designed aluminum plates thickness was not needed.

The magnetic field for the rf coil was calculated by the Biot-Savart law implemented in the self-modified script reported in Appendix B.

We found that the best arrangement for the rf coil – is two square shaped wires coil, with which it was possible to have a relatively big homogeneous region along x and y axis, but relatively thin (around 1 cm in Z direction). Nevertheless, the magnet and the coil of this equipment compared to the common uniliteral tools has a large homogeneous region at a big distance from the top surface of the magnet. These results were in a good agreement with those obtained by ESR5, and the final design chosen was a two wires square spiral coil as it showed good homogeneity and is relatively easy to construct.

The instrument equipped with the designed single-sided magnet and coil was built by the ERICA partner company MR Solutions (Abingdon, UK), and will be available to beneficiaries and partners of the ERICA project from winter 2022.

Some preliminary measurements on the cement paste, hydrated for 13 hours with the new set-up (courtesy of University of Surrey) were performed. Measured CPMG raw data in Figure 7.3.1 were good and did not show much noise or interferences. In Figure 7.3.2 T_2 distribution shows a good result, though it was not possible to see interlayer spaces due to the too long echo time and it was not possible to directly compare it with the one done by conventional bore magnet. Nevertheless, excluding interlayer space from consideration, the result is in good agreement with previously done experiments.

9.5. 2D experiments on re-saturation of WPC sample with w/c 0.5

A typical T_1-T_2 correlation map of a fully saturated sample is shown in Figure 8.1.1 and it is in good agreement with the results obtained by C. Cadar et al. [141]. We were able to determine 5 components with small amount of signal at T_2 ~ 1 ms and T_1 ~ 1.6 ms, which is compatible with the shoulder to the right of gel pores in 1D experiments for WPC sample 0.5 w/c (Figures 6.2.1). Thus, we can assume that this signal arises from a real component of cement, and it is not a noise artifact. At T_2 ~ 0.8 ms and T_1 ~ 20 ms, an off-diagonal peak is present, which could indicate ^{1}H chemical exchange of water molecules in the pores with corresponding relaxation times, or represent an isolated spin population with this T_1 and T_2 value. Another possibility that the off-diagonal peak is merely artifacts. An explanation of possible chemical exchange in cement samples (off-diagonal peaks) was observed in the work in ref [75] or in [141]. Despite in our sample the off-diagonal signal had higher T_2 and T_1 values, which might be due to that our sample was older and most of the hydration processes already ended.

In Figure 8.2.1 changes in the porous structure are shown. During the first hour of re-saturation process, the signal was clearly separated into three components: gel, interhydrate and capillary water. Observed peaks at the first hour of re-saturation were at the same diagonal with as-prepared sample, at 3 hours the peaks shifted from this diagonal to higher T_1/T_2 rates, which might indicate changes in ^{1}H mobility or effects of the surface tension and diffusion process. Whereas peaks of gel pores and interhydrates returned back to as-prepared diagonal, T_1/T_2 ratio of capillary water component increased from ≈1.6 to ≈3.5.

After 3 hours of re-saturation till at least 317 hours we observed off-diagonal peaks which shifted to the lover T_2 time through the process and disappear after 749 hours. As it was stated previously these off-diagonal peaks might indicate ^{1}H chemical exchange of water molecules in the pores with corresponding relaxation times. This explanation could be supported by the movement of the off-diagonal peaks to the smaller relaxation time values as rearrangement of water was happening through the re-saturation. Another possible explanation could lie in the data inversion process. Further experiments are needed to confirm these results.

At 68 and 317 hours it was possible to see interlayer water signal and it was not present at other times, which is most probably due to the reduced sensitivity of the 2D analysis, with respect to the 1D analysis, which makes the interlayer component visible only when its amplitude has grown up enough and the parameters of the measurement are carefully adjusted.

Component associated with the gel pores constantly increased in signal intensity (Figure 8.2.2) through re-saturation, T_2 relaxation time of the peak decreased up to 68 hours reaching its as-prepared value, T_1 time decreased up to 317 hours and increased slightly after which suggests refilling of the pores and relaxation process is influenced by the pore surface interactions.

Peak associated with capillary pores increased in signal intensity up to 317 hours and decreased later to the relative value at 821 hours less than for as-prepared sample.

The relaxation time of the component associated to interhydrate pores increased from the start of re-saturation up to 821 hours but never gained the same value as for as-prepared sample which suggests structural changes considering that the relaxation time of the component to the right of interhydrates increased. By these preliminary experiments on cement samples, we showed that the 2D technique is a powerful tool to continuously observe changes in the porous structure of cement during sorption experiments. Mupen2D and Upen2D software are still developing, nevertheless we showed that it worked well for the 2D experiments fitting.

CONCLUSION

During this work we established and applied the testing procedure for cement samples NMR observation during sorption cycles of drying and re-saturation, done by RH controlled drying procedure (over months) and by drying in the oven (over weeks).

For the measurements, different cement samples were used – with different w/c ratios, and with additional gypsum to account for different porous structures.

Concerning the analysis of different w/c ratios, it was found that samples with higher w/c ratio tends to have a greater number of larger pores, which is in good agreement with results from literature by other methods.

Added gypsum changed the speed of the hydration process of a cement – gel porosity developed for the WPCG samples faster than for WPC samples, but for as-prepared samples (hydrated for 28 days under-water) of the same w/c ratio (0.5), pore size distribution did not show a large difference.

Comparison was done with the data obtained by ESR2 on samples measured during early hydration stages, and results were in good agreement.

Different data fitting technique for the T_2 measurements were performed and results compared. Quasi-continuous distribution fitting by UpenWin went along with the multi-exponential fitting, performed with the use of Psi-Plot software.

Results on as-prepared samples were in good agreement with the results shown in literature by NMR methods and cited in this work.

As a general comment, we showed that NMR technique is a good way to obtain pore-resolved isotherm, which allows a close observation of structural changes during drying – re-saturation cycles.

We found that by both oven drying and RH drying, the non-evaporable water seems to be enclosed in interlayer spaces. This water took up around 15% of the whole water signal (detectable in our experiments with oven-dried samples), which seems to be around the same for samples of different w/c.

We were able to observe irreversible shrinkage of the interlayer spaces occurring during the first sorption cycle by the T_2 values, changing through drying and re-saturation. For all WPC samples, we found that the amount of interlayer water signal decreased after re-saturation, which indicates structural changes.

On contrary, sample with added gypsum showed different trends for re-saturation than WPC samples. This might indicate that the structure of the sample was more altered during drying than in other samples. In fact, we showed that the porous structure of the as-prepared WPC samples and with and without added gypsum did not differ much.

By the Pake-Doublet analysis, it was possible to determine changes in solid structure (crystal water), namely Ettringite, which showed a similar trend during drying for the WPC samples of different w/c ratios. These behavior of water in Ettringite is similar to what was found in literature, using different non-NMR methods.

As far as we known, this is the first time that the Pake-Doublet analysis is used to characterize the structural change in cement sample by drying/re-saturating cycles. These results were presented at the Spinus-2021 conference in Saint-Petersburg [144] and published in the Journal of Applied Magnetic Resonance [145].

For better understanding the processes during sorption cycles, also 2D NMR measurements were performed with the use of NMR MOUSE PM10 (measurements performed at the Department DIFA, University of Bologna) and the data inversion performed with Upen2D, an inversion software still under development by the NMR and porous media Bologna group. By continuous T_1-T_2 measurements it was possible to see water re-distribution during re-saturation process. We believe that such experiments have not been done previously. We concluded that water at the beginning of the process entered through smaller pores, went to bigger pores and distributed through all pore structure. The T_1/T_2 ratio of the capillary water component after drying and re-saturation changed, but as we cannot have a clear understanding of such behaviour, further experiments with different methods (T_2-T_2 and D-T_2) are planned. Changes of the interhydrate and capillary porosity due to drying was shown.

In addition to the sorption cycles observation, work on the developing a prototype end-user MR magnet for in-situ use (in the built environment) was done.

In collaboration with University of Surrey and MR Solution, we were able to develop fully working one-sided NMR set-up with relatively large and relatively highly homogeneous magnetic sweet spot. The work included modelling of the magnetic field from the permanent magnet with the use of FEMM and Ansys CADs, and COMSOL software. The magnetic field from the NMR coil was also modelled by using a specifically modified Biot-Savart magnetic MatLab toolbox. And the calculation of pulling forces was also performed. Finally, the magnet has been assembled and some first measurements on fresh cement paste were done and demonstrated good results.

To conclude:

1. Quasi-continuous distribution of relaxation times computed on the WPC NMR data show NMR parameters that are in good agreement with literature results performed with different data processing and with ones presented by ESR2 with the same data analysis method;

2. We were able to build pore-resolved isotherm of the WPC samples dried at controlled RH;

3. From our experiments on oven-dried samples, we found that non-evaporable water in interlayer spaces might be around 15% of total water sensed by the instrument;

4. Mechanisms of drying and re-saturation processes are similar for all the WPC samples at different w/c ratio examined;

5. Mechanism of re-saturation for samples with added gypsum is different, might be due to the different level of structural changes during drying;

6. Water at the beginning of re-saturation seems to enter through smaller pores to bigger pores and spread through the structure;

7. We argue that some changes of the water proton mobility, surface tension or diffusion are happening during drying;

8. We showed, as far as we know for the first time, that Pake-Doublet analysis is a good way to observe changes in the solid structure of cement samples during sorption cycles, and found changes to the amount of Ettringite during drying;

9. A new inversion algorithms (MUpen2D and Upen2D), still under development, were used to obtain 2D T_1-T_2 correlation maps. 2D NMR analyses confirmed 1D NMR results and offered further details to characterize the evolution during hardening of WPC ^{1}H components.

10. We cooperate to the development of a fully functioning one-sided NMR instrument for *in-situ* measurements.

To corroborate these results, some more experiments in future are needed, concerning more 2D measurements with different samples and different experiments, such as D-T_2 and T_2-T_2, and experiments to prove or refute results on samples with added gypsum. Also, to reaffirm results on the solid structure, more experiments at specific RH points are planned.

In the future, measurements on different cementitious materials will be performed and correlated with strength development during hydration.

11. References

1. Our projects, ERICA ETN, viewed 1st of December 2021, <https://www.erica-etn.eu/projects/>
2. R. P. Chhabra, J. F. Richardson, Non-Newtonian Flow and Applied Rheology, IInd edition, Butterworth-Heinemann, Oxford, U. K., 2008, pp.: 54-81.
3. D.D. Ganji, S.H.H. Kachapi, Application of Nonlinear Systems in Nanomechanics and Nanofluids Analytical Methods and Applications, William Andrew, Micro and Nano Technologies Series, 2015, p. 412.
4. Ron Darby, Raj P. Chhabra, Chemical Engineering Fluid Mechanics, Third Edition, CRC Press, 2017, p. 577. https://doi.org/10.1201/9781315370675
5. *IUPAC. Compendium of Chemical Terminology, 2nd ed. Compiled by A. D. McNaught and A. Wilkinson. Blackwell Scientific Publications, Oxford, 1997. Online version (2019-) created by S. J. Chalk. ISBN 0-9678550-9-8.* https://doi.org/10.1351/goldbook.
6. Z.A. Alothman, A Review: Fundamental Aspects of Silicate Mesoporous Materials. Materials, V. 4, pp: 2874 – 2902, 2015, https://doi.org/10.3390/ma5122874.
7. H. Zhao, Q. Xiao, D. Huang, Sh. Zhang, Influence of Pore Structure on Compressive Strength of Cement Mortar, The Scientific World Journal, V. 5, 2014, https://doi.org/10.1155/2014/247058
8. I. Odler, M. Rößler, Investigations on the relationship between porosity, structure and strength of hydrated Portland cement pastes. II. Effect of pore structure and of degree of hydration, Cement and Concrete Research, V. 15, N. 3, pp. 401–410, 1985, https://doi.org/10.1016/0008-8846(85)90044-4.
9. A. Valori, Characterisation of Cementitious Materials by ^{1}H NMR, Doctoral thesis, University of Surrey.
10. ASTM C150/C150M Standard Specification for Portland Cement, ASTM: West Conshohocken, PA, USA, 2021
11. Specification for blastfurnace cements with strength properties outside the scope of BS EN 197-1, BSI, 2002.
12. W. Kurdowsi, Cement and Concrete Chemistry, Springer, Dordrecht, 2014, p. 700. https://doi.org/10.1007/978-94-007-7945-7
13. H.F.W. Taylor, Cement chemistry, 2nd Edition, Default Book Series, 1997, p. 475.

14. P.-C. Aïtcin, R. J. Flatt, Science and Technology of Concrete Admixtures, P.-C. Aïtcin, Part 3 Portland cement, Université de Sherbrooke, 2015, p. 616.
15. P. Hewlett, M. Liska, Lea's Chemistry of Cement and Concrete, J. Beaudoin, I. Odler Part 5 Hydration, Setting and Hardening of Portland Cement, Butterworth-Heinemann, 2017, p. 858, https://doi.org/10.1016/C2013-0-19325-7.
16. Xiandong Cong, R. James Kirkpatrick, ^{17}O and ^{29}Si MAS NMR study of β–C2S hydration and the structure of calcium-silicate hydrates, Cement and Concrete Research, V. 23, N. 5, pp.: 1065-1077, 1993, https://doi.org/10.1021/j100289a010.
17. N. Shiferaw, L. Habte, T. Thenepalli, J.W. Ahn, Effect of Eggshell Powder on the Hydration of Cement Paste. *Materials*, V.12(15):2483, 2019, https://doi.org/10.3390/ma12152483
18. R. F. Feldman, P. J. Sereda, A model for hydrated Portland cement paste as deduced from sorption-length change and mechanical properties. Matériaux et Construction, Vol. 1, pp: 509–520, 1968.
19. J H. M. Jennings, Refinements to colloid model of C-S-H in cement: CM-II, Cement and Concrete Research, V. 38 (3), pp. 275-289, 2008, http://dx.doi.org/10.1016/j.cemconres.2007.10.006.
20. T.C. Powers, T.L. Brownyard, Studies of the physical properties of hardened Portland cement paste, Bull. 22, Res. Lab. of Portland Cement Association, Skokie, IL, U.S.A., reprinted from J. Am. Concr. Inst. (Proc.), vol. 43 (1947)
21. R.B. Williamson, Solidification of Portland cement, Progress in Materials Science, Volume 15, Issue 3, 1972, Pages 189-286.
22. D. Hillel, J.L. Hatfield, D.S. Powlson, C. Rosenzweig, K.M. Scow, M.J. Singer, Encyclopedia of Soils in the Environment, First Edition, Elsevier Academic Press, 2005, p. 2200.
23. D.H. Everett, Manual of symbols and terminology for physicochemical quantities and units. Appendix II definitions, terminology and symbols in colloid and surface chemistry part I adopted by the IUPAC council at Washington DC, USA, 1971.
24. V. Baroghel-Bouny, Water Vapour Sorption Experiments on Hardened Cementitious Materials: Part I: Essential Tool for Analysis of Hygral Behaviour and its Relation to Pore Structure. Cement and Concrete Research, V. 37 (3), pp: 414-437, 2007, https://doi.org/10.1016/j.cemconres.2006.11.019.
25. M. Wu, B. Johannesson, M.R. Geiker, A study of the water vapor sorption isotherms of hardened cement pastes: Possible pore structure changes at low relative humidity and the

impact of temperature on isotherms. Cement and Concrete Research, V. 56, pp.: 97-105, 2014, 10.1016/j.cemconres.2013.11.008.

26. L. Casnedi, O. Cocco, M. Paola, G. Pia, Water Absorption Properties of Cement Pastes: Experimental and Modelling Inspections. Advances in Materials Science and Engineering, 2018. 10.1155/2018/7679131.
27. O.C.G. Adan, Determination of moisture diffusivities in gypsum renders. HERON-English edition, Vol. 40, pp: 201-216, 1995.
28. C. Gallé, Effect of drying on cement-based materials pore structure as identified by mercury intrusion porosimetry: A comparative study between oven-, vacuum-, and freeze-drying. Cement and Concrete Research, Vol. 31(10), pp:1467-1477, 2001, http://dx.doi.org/10.1016/S0008-8846(01)00594-4.
29. H.J.H. Brouwers, The work of Powers and Brownyard revisited: Part 1. Cement and Concrete Research, Vol. 34(9), pp: 1697–1716, 2004, http://dx.doi.org/10.1016/j.cemconres.2004.05.031.
30. A. Korpa, R. Trettin, The influence of different drying methods on cement paste microstructures as reflected by gas adsorption: Comparison between freeze-drying (F-drying), D-drying, P-drying and oven-drying methods,Cement and Concrete Research, V. 36, N. 4, pp.: 634-649, 2006, https://doi.org/10.1016/j.cemconres.2005.11.021.
31. V. Baroghel-Bouny, T. Chaussadent, Texture and Moisture Characterization of Hardened Cement Pastes and Concretes from Water Vapour Sorption Measurements. In: H. Jennings, J. Kropp, K. Scrivener (eds) The Modelling of Microstructure and its Potential for Studying Transport Properties and Durability. NATO ASI Series (Series E: Applied Sciences), V. 304. Springer, Dordrecht, pp.: 241-255, 1996, https://doi.org/10.1007/978-94-015-8646-7_11
32. A. Kumar, S. Ketel, K. Vance, T. Oey, N. Neithalath, G. Sant, Water Vapor Sorption in Cementitious Materials-Measurement, Modeling and Interpretation. *Transport in Porous Media*, V. *103*(1), pp.:69-98, 2014. https://doi.org/10.1007/s11242-014-0288-5
33. J. Hagymassy, S. Brunauer, R.Sh Mikhail, Pore structure analysis by water vapor adsorption: I. t-Curves for water vapor, Journal of Colloid and Interface Science, V.29, N.3,pp.: 485-491, 1969, https://doi.org/10.1016/0021-9797(69)90132-5.
34. G. L. Kalousek, Fundamental Factors in Drying. Shrinkage of Concrete Block. J. Am. Concrete Inst., pp: 233-348, 1954.

35. S. Brunauer, L. E. Copeland, R. H. Bragg, The Stoichiometry of the Hydration of Tricalcium Silicate at Room Temperature. I. Hydration in Paste Form, J. Phys. Chem., V. 60(1), pp: 112-116, 1956, DOI: 10.1021/j150535a027.
36. S. Brunauer, D. L. Kantro, L. E. Copeland, The Stoichiometry of the Hydration of β-Dicalcium Silicate and Tricalcium Silicate at Room Temperature. Journal of the American chemical society, V. 80(4), pp: 761-767, 1958, DOI: 10.1021/ja01537a001.
37. I. Odler, H. Köster, Investigations on the structure of fully hydrated Portland cement and tricalcium silicate pastes. II. Total porosity and pore size distribution. Cement and Concrete research. V. 16, pp: 893-901, 1986.
38. R. Sh. Mikhail, Pore Structures and Surface Areas of Hardened Portland Cement Pastes by Nitrogen Adsorption. Can. Jour. Chem., V. 42, pp. 426-438, 1964.
39. V. Baroghel-Bouny, M. Mainguy, T. Lassabatère, O. Coussy, Characterization and identification of equilibrium and transfer moisture properties for ordinary and high-performance cementitious materials. *Cement and Concrete Research, V.29*, pp.: 1225-1238, 1999, https://doi.org/10.1016/S0008-8846%2899%2900102-7.
40. S. Lowell, J. Shields, M.A. Thomas, M. Thommes, Characterization of Porous Solids and Powders: Surface Area, Pore Size and Density, Springer, 2006, 10.1007/978-1-4020-2303-3.
41. H. Ranaivomanana, Toward a better comprehension and modelling of hysteresis cycles in the water sorption–desorption process for cement based materials. Cement and Concrete Research, V. 41(8), pp: 817-827, 2011, http://dx.doi.org/10.1016/j.cemconres.2011.03.012.
42. B.M. Pinson, E. Masoero, P.A. Bonnaud, H. Manzano, Q. Ji, S. Yip, J.J. Thomas, M.Z. Bazant, V. Van, J. Krystyn, H.M. Jennings, Hysteresis from Multiscale Porosity: Modeling Water Sorption and Shrinkage in Cement Paste, American Physical Society, V. 3, 2015, https://doi.org/10.1103/PhysRevApplied.3.064009.
43. D.H. Everett, Manual of symbols and terminology for physicochemical quantities and units. Appendix II definitions, terminology and symbols in colloid and surface chemistry part I adopted by the IUPAC council at Washington DC, USA, Butterworths, pp.: 579-638, 1971.
44. A.E. Idiart, Coupled analysis of degradation processes in concrete specimens at the meso-level, Doctoral Thesis, Doctoral Program in Geotechnical Engineering Barcelona, 2009.

45. P.W. Schiller, M. Wahab, T.A. Bier, S. Waida, H.J. Mögel, Capillary Forces and Sorption Hysteresis of Cement Pastes with Small Slit Pores, Procedia Materials Science. V.11., pp.: 649-654, 2015, 10.1016/j.mspro.2015.11.010.
46. V.G. Papadakis, C.G. Vayenas, M.N. Fardis, Physical and chemical characteristics affecting the durability of concrete, ACI Materials Journal. V. 88, pp.: 186-196., 1991.
47. J. W. McBain, An Explanation of Hysteresis in the Hydration and Dehydration of Gels. J. Am. Chem. Soc., Vol. 57(4), p. 700, 1935, DOI: 10.1021/ja01307a502.
48. Z.P. Bazant, Constitutive equation for concrete creep and shrinkage based on thermodynamics of multiphase systems. Matériaux et Constructions, V. 3(1), pp: 3-36, 1970, DOC: 10.1007/BF02475106
49. Z.P. Bazant, M.Z. Bazant, Theory of Sorption Hysteresis in Nanoporous Solids: I. Snap-Through Instabilities. Journal of the Mechanics and Physics of Solids, V. 60(9), pp: 1644–1659, 2012, https://doi.org/10.1016/j.jmps.2012.04.014.
50. T. C. Powers, Structure and Physical Properties of Hardened Portland Cement Paste. Journal of The American Ceramic Society, 1958, https://doi.org/10.1111/j.1151-2916.1958.tb13494.x.
51. F. Beltzung, F.H. Wittmann, Role of Disjoining Pressure in Cement Based Materials. Cement and Concrete Research, V. 35(12), pp.: 2364-2370, 2005, doi:10.1016/j.cemconres.2005.04.004.
52. A.M. Gajewicz-Jaromin, E.M. Gartner, K. Kang, P.J. McDonald, V. Yermakou, A ^{1}H NMR relaxometry investigation of gel-pore drying shrinkage in cement pastes. Cement and Concrete Research, V. 86, pp.: 12-19, 2016, 10.1016/j.cemconres.2016.04.013.
53. J. Thomas, A.J. Allen, H.M. Jennings, Structural Changes to the Calcium–Silicate–Hydrate Gel Phase of Hydrated Cement with Age, Drying, and Re-saturation, The American Ceramic Society, V. 91, pp: 3362-3369, 2008, [online], https://tsapps.nist.gov/publication/get_pdf.cfm?pub_id=851119
54. Y. Aono, F. Matsushita, S. Shibata, Y. Hama, Nano-structural Changes of C-S-H in Hardened Cement Paste during Drying at 50°C. Journal of Advanced Concrete Technology, V.5(3), pp.: 313-323, DOI:10.3151/jact.5.313.
55. D. Pearson, A.J. Allen. A study of ultrafine porosity in hydrated cements using small angle neutron scattering. Journal of Materials Science, v.20(1), pp.:303–315, 1985, https://doi.org/10.1007/BF00555924
56. I. Maruyama, G. Igarashi, Y. Nishioka, Bimodal Behavior of C–S–H Interpreted From Short-Term Length Change and Water Vapor Sorption Isotherms of Hardened Cement

Paste. Cement and Concrete Research. V.73, pp.:158-168, DOI:10.1016/j.cemconres.2015.03.010.

57. A. Bentur, R.L. Berger, F.V. Lawrence, N.B. Milestone, S. Mindess, J.F. Young, Creep and drying shrinkage of calcium silicate pastes III. A hypothesis of irreversible strains. *Cement and Concrete Research, V.9*, pp.: 83-95, DOI:10.1016/0008-8846(79)90098-X
58. X. Cong, R. J. Kirkpatrick, Effects of the temperature and relative humidity on the structure of C-S-H gel, Cement and Concrete Research, V. 25(6), pp.:1237-1245, 1995, DOI : 10.1016/0008-8846(95)00116-T.
59. I. Maruyama, Y. Nishioka, G. Igarashi, K. Matsui, Microstructural and Bulk Property Changes in Hardened Cement Paste During the First Drying Process. Cement and Concrete Research, V. 58, pp.: 20–34, 2014, DOI: 10.1016/j.cemconres.2014.01.007.
60. B. Cowan, Nuclear Magnetic Resonance and Relaxation. Cambridge: Cambridge University Press., p. 434, 1997, doi:10.1017/CBO9780511524226
61. C.F. Thomas, D.B. Edwin, Pulse and Fourier Transform NMR Introduction to Theory and Methods, p. 132, 1971.
62. M.H. Levitt, Spin Dynamics: Basics of Nuclear Magnetic Resonance, 2nd Edition, WILEY, p. 740, 2008,
63. A. R. Edmonds, Angular Momentum in Quantum Mechanics, Index Princeton University Press, p.160, 1957, DOI: https://doi.org/10.1515/9781400884186-013
64. P.J. Hore, Nuclear Magnetic Resonance. Oxford Chemistry Primers No. 32 Oxford Science Publications, Oxford University Press, p. 90, 1995.
65. K.-J. Dunn, D.J. Bergman, G.A. LaTorraca, NMR LOGGING Principles and Applications, 1st Edition, p.312, 2002.
66. J. Higinbotham, I. Marshall, NMR lineshapes and lineshape fitting procedures, Annual Reports on NMR Spectroscopy, Academic Press, V. 43, pp.: 59-120, 2001, DOI:10.1016/S0066-4103(01)43009-2.
67. P. J. McDonald, A. M. Gajewicz, The Characterisation of Cement Based Materials Using T_2 ^{1}H Nuclear Magnetic Resonance Relaxation Analysis, Good Practice guide No.144, NPL Management Limited, p.165, 2016.
68. J.G. Powles, J.H. Strange, Zero Time Resolution Nuclear Magnetic Resonance Transient in Solids, *Proc. Phys. Soc.* V.82, 1963.
69. G.E. Pake, E.M. Purcell, Lineshapes in nuclear paramagnetism, Phys. Rev. V. 74(9), 1948.
70. A. Abragam, The Principles of Nuclear Magnetism, Clarendon Press, p. 618, 1983.

71. D. C. Look, I. J. Lowe, Nuclear Magnetic Dipole—Dipole Relaxation Along the Static and Rotating Magnetic Fields: Application to Gypsum, J. Chem. Phys. V. 44, 1996, https://doi.org/10.1063/1.1727169.
72. W. Derbyshire, M. van den Bosch, D. van Dusschoten, W. MacNaughtan, I.A. Farhat, M. A. Hemminga, J. R. Mitchell, Fitting of the beat pattern observed in NMR free-induction decay signals of concentrated carbohydrate-water solutions. *Journal of Magnetic Resonance*, V.*168*(2), pp.: 278-283, 2004, https://doi.org/10.1016/j.jmr.2004.03.013
73. V. Bortolotti, L. Brizi, R. J. S. Brown, P. Fantazzini, M. Mariani, Nano and Sub-nano Multiscale Porosity Formation and Other Features Revealed by 1H NMR Relaxometry during Cement Hydration, Langmuir V. 30, pp.:10871−10877, 2014, https://doi.org/10.1021/la501677k.
74. K.R. Brownstein, C.E Tarr, Spin-lattice relaxation in a system governed by diffusion, Journal of Magnetic Resonance, V.26(1), 1969, https://doi.org/10.1016/0022-2364(77)90230-X.
75. P.J. McDonald, J.P. Korb, J. Mitchell, L. Monteilhet, Surface relaxation and chemical exchange in hydrating cement pastes: a two-dimensional NMR relaxation study, Phys Rev E Stat Nonlin Soft Matter Phys. V.72(1), 2005, DOI: 10.1103/PhysRevE.72.011409.
76. S. Davies, K.J. Packer, D.R. Roberts, F.O. Zelaya, Pore-size distributions from NMR spin-lattice relaxation data, Magnetic Resonance Imaging, V.9, pp.: 681-685, 1991, https://doi.org/10.1016/0730-725X(91)90357-R.
77. S. Stapf, R. Kimmich, R.-O. Seitter, Proton and Deuteron Field-Cycling NMR Relaxometry of Liquids in Porous Glasses: Evidence for Levy-Walk Statistics, Physical Review Letters, V.75, 1995, DOI:https://doi.org/10.1103/PhysRevLett.75.2855.
78. J.P. Korb, M.W. Hodges, R. Bryant ,Translational diffusion of liquids at surface of microporous materials: new theoretical analysis of field cycling magnetic relaxation measurements, Magn Reson Imaging, V.16(5-6), pp.:575-578, 1998, DOI: 10.1016/s0730-725x(98)00051-4. PMID: 9803912.
79. D.A. Faux, R. Kogon, V. Bortolotti, P. McDonald, Advances in the Interpretation of Frequency-Dependent Nuclear Magnetic Resonance Measurements from Porous Material, *Molecules*, V. 24(20):3688, 2019, https://doi.org/10.3390/molecules24203688.
80. J. Jeener, G. Alewaeters, unpublished work, G. Alewaeters, Doctoral thesis, Free University of Brussels, 1976.

81. W. P. Aue, E. Bartholdi, R. R. Ernst, Two-dimensional spectroscopy. Application to nuclear magnetic resonance, Journal of Chemical Physics V.64, pp.: 2229–2246, 1976, doi:10.1063/1.432450.
82. A. Valori, V.V. Rodin, P.J. McDonald, On the interpretation of ^{1}H 2-dimensional NMR relaxation exchange spectra in cements: Is there exchange between pores with two characteristic sizes or Fe3+ concentrations?, *Cement and Concrete Research, V.40*, pp.:1375-1377, 2010, DOI:10.1016/J.CEMCONRES.2010.03.022
83. Y.-Q. Song, L. Zielinski, S. Ryu, Two-Dimensional NMR of Diffusion Systems, Phys. Rev. Lett., V.100(24):248002, 2008, https://link.aps.org/doi/10.1103/PhysRevLett.100.248002
84. H. C. Torrey, Bloch Equations with Diffusion Terms, Phys. Rev., V.104(3), pp.: 563–565, 1956, https://link.aps.org/doi/10.1103/PhysRev.104.563.
85. L. Brizi, Time domain and spatially resolved NMR: advanced applications to porous media of interest to environmental sustainability and human healthcare, Doctoral Thesis, Dottorato di ricerca in fisica, Universita di Bologna, 2016.
86. D.P. Cistola, M.D. Robinson, Compact NMR relaxometry of human blood and blood components.,Trends Analyt Chem V.83(A), pp.:53-64, 201,. doi:10.1016/j.trac.2016.04.020.
87. S.W. Provencher, CONTIN: A general purpose constrained regularization program for inverting noisy linear algebraic and integral equations. Comput. Phys. Commun. V.27(3), pp.:229-242, 1982, https://doi.org/10.1016/0010-4655(82)90174-6.
88. UpenWin, V. Bortolotti, R.J.S. Brown, P. Fantazzini, UpenWin: A software to invert multi-exponential decay data, viewed 12/12/2021, <http://www.unibo.it/PortaleEn/Research/Services+for+companies/UpenWin.htm >
89. E. Fordham, L. Venkataramanan, J. Mitchell, A. Valori, What are , and what are not , Inverse Laplace Transforms, Journal for the Basic Principles of Diffusion Theory, Experiment and Application, 2017.
90. Y.Q. Song, L. Venkataramanan, L. Burcaw, Determining the resolution of Laplace inversion spectrum, J Chem Phys, V.122(10):104104, 2005, DOI: 10.1063/1.1858436. PMID: 15836306.
91. P. Berman, O. Levi, Y. Parmet, M. Saunders, Z. Wiesman, Laplace Inversion of Low-Resolution NMR Relaxometry Data Using Sparse Representation Methods, Concepts Magn Reson Part A Bridg Educ Res, V.42(3), pp.:72-88, 2013, DOI: 10.1002/cmr.a.21263.

92. V. Bortolotti, R. J. S. Brown, P. Fantazzini, G. Landi, F. Zama, Uniform Penalty inversion of two-dimensional NMR Relaxation data, Inverse Problems, V.33(1):015003, 2016, DOI: 10.1088/1361-6420/33/1/015003.
93. J. P. Butler, J. A. Reeds, S. V. Dawson, Estimating Solutions of First Kind Integral Equations with Nonnegative Constraints and Optimal Smoothing, SIAM Journal on Numerical Analysis, V.18(3), pp.:381-397, 1981.
94. K.W. Whittall, A.L. MacKay, Quantitative interpretation of NMR relaxation data, Journal of Magnetic Resonance (1969), V. 84(1), pp.:134-152, 1989, https://doi.org/10.1016/0022-2364(89)90011-5.
95. K. M. Koch, D. L. Rothman, R. A. de Graaf, Optimization of static magnetic field homogeneity in the human and animal brain in vivo, Progress in Nuclear Magnetic Resonance Spectroscopy, V.54, I.2, pp: 69-96, 2009, https://doi.org/10.1016/j.pnmrs.2008.04.001.
96. D.V. Perepelitsa, Johnson Noise and Shot Noise, MIT Department of Physics, 2006.
97. A.J. Maubon, J.-M. Ferru, V. Berger, M. C. Soulage, M. DeGraef, P. Aubas, P. Coupeau, E. Dumont, J.-P. Rouanet, Effect of Field Strength on MR Images: Comparison of the Same Subject at 0.5, 1.0, and 1.5 T, RadioGraphycs, V, 19(4), pp.: 1057-1067, 1999, https://doi.org/10.1148/radiographics.19.4.g99jl281057.
98. G. Eidmann, R. Savelsberg, P. Blümler, B. Blümich, The NMR MOUSE, a Mobile Universal Surface Explorer, Journal of Magnetic Resonance, Series A, V.122(1),pp.:104-109, 1996, https://doi.org/10.1006/jmra.1996.0185.
99. B. Blümich, P. Blümler, G. Eidmann, A. Guthausen, R. Haken, U. Schmitz, K. Saito, G. Zimmer, The NMR-mouse: construction, excitation, and applications, Magn Reson Imaging, V.16(5-6), pp.:479-84, 1998, DOI: 10.1016/s0730-725x(98)00069-1
100. F. Casanova, J. Perlo, B. Blümich, Single-Sided NMR, Springer, Heidelberg, p. 244, 2011, https://doi.org/10.1007/978-3-642-16307-4.
101. I.M. Savukov, S.J. Seltzer, M.V. Romalis, Detection of NMR signals with a radio-frequency atomic magnetometer, J Magn Reson, V.185(2), pp.:214-20, 2007, doi: 10.1016/j.jmr.2006.12.012.
102. P. Andris, J. Weis, I. Frollo, Magnetic Field of Spiral-shaped Coil, MEASUREMENT 2009, Proceedings of the 7th International Conference, Smolenice, Slovakia, 2009.
103. R. Blinc, M. Burgar, G. Lahajnar, M. Rozmarin, V. Rutar, I. Kocuvan, J. Ursic, NMR relaxation study of adsorbed water in cement and C3S pastes, J. Am. Ceram. Soc., V.61 (1-2), pp. 35–37, 1978, DOI: 10.1111/j.1151-2916.1978.tb09224.x.

104. L. J. Schreiner, J. C. Mactavish, L. Miljkovic, M. M. Pintar, R. Blinc, G. Lahajnar, D. D. Lasic, L. W. Reeves, NMR Line Shape-Spin-Lattice Relaxation Correlation Study of Portland Cement Hydration, J. Am. Ceram. Soc., V.68 (1), pp.:10–16, 1985, https://doi.org/10.1111/j.1151-2916.1985.tb15243.x.
105. W. P. Halperin, J.-Y. Jehng, Y.-Q. Song, Application of spin-spin relaxation to measurement of surface area and pore size distributions in a hydrating cement paste, Magn. Reson. Imag., V.12(2), pp.:169–173, 1994, https://doi.org/10.1016/0730-725X(94)91509-1.
106. M. Al-Zahrani, A.-H. Al-Tayyib, E. Twum, S. Al-Dulaijan, ^{29}Si MAS-NMR study of hydrated cement paste and mortar with varying content of fly ash, Advances in Cement Research - ADV CEM RES., V.18, pp.:27-34, 2006. DOI:10.1680/adcr.2006.18.1.27.
107. R. Gummerson, C. Hall, W. Hoff, R. Hawkes, G. N. Holland, W. S. Moore, Unsaturated water flow within porous materials observed by NMR imaging, Nature V.281, pp.:56–57, 1979, https://doi.org/10.1038/281056a0.
108. A.J. Bohris, U. Goerke, P.J. McDonald, M. Mulheron, B. Newling, B. Le Page, A broad line NMR and MRI study of water and water transport in Portland cement pastes, Magn Reson Imaging, V.16(5-6), pp.:455-61, 1998, DOI: 10.1016/s0730-725x(98)00072-1. PMID: 9803890.
109. M. Bogdan, B.J. Balcom, T.W. Bremner, R.L. Armstrong, Single-point imaging of partially dried, hydrated white Portland cement, JOURNAL OF MAGNETIC RESONANCE, Series A, V. 116, pp.:266–269, 1995, DOI: 10.1006/jmra.1995.0019.
110. J.-Y. Jehng, D.T. Sprague, W.P. Halperin, Pore structure of hydrating cement paste by magnetic resonance relaxation analysis and freezing, Magnetic Resonance Imaging, V.14(7-8), pp.:785-791, 1996, https://doi.org/10.1016/S0730-725X(96)00164-6.
111. J. Greener, H. Peemoeller, C. Choi, R. Holly, E.J. Reardon, C.M. Hansson, M.M. Pintar, Monitoring of Hydration of White Cement Paste with Proton NMR, J. Am. Ceram. Soc, V.83, pp.:623–627, 2000, https://doi.org/10.1111/j.1151-2916.2000.tb01242.x.
112. F. Barberon, J.-P. Korb, D. Petit, V. Morin, E. Bermejo, What is the surface specific area of porous cement-based material? A nuclear magnetic relaxation dispersion approach, Magnetic Resonance Imaging, V.21(3–4),pp.:355-357, 2003, https://doi.org/10.1016/S0730-725X(03)00137-1.
113. A. Plassais, M.P. Pomiès, N. Lequeux, P. Boch, J.P. Korb, D. Petit, F. Barberon, Micropore size analysis by NMR in hydrated cement, Magn Reson Imaging, V.21(3-4), pp.:369-371, 2003, DOI: 10.1016/s0730-725x(03)00141-3. PMID: 12850736.

114. P. J. McDonald, J.-P. Korb, J. Mitchell, L. Monteilhet, Surface relaxation and chemical exchange in hydrating cement pastes: A two-dimensional NMR relaxation study, Phys. Rev. E, V.72(1):011409, 2005, https://doi.org/10.1103/PhysRevE.72.011409.

115. M. Gombia, V. Bortolotti, B. De Carlo, R. Mongiorgi, S. Zanna, P. Fantazzini, Nanopore Structure Buildup during Endodontic Cement Hydration Studied by Time-Domain Nuclear Magnetic Resonance of Lower and Higher Mobility ^{1}H, J. Phys. Chem. B., V.114, pp.:1767–1774, 2010, https://doi.org/10.1021/jp907248r.

116. V. Bortolotti, P.Fantazzini, R. Mongiorgi, S. Sauro, S. Zanna, Hydration kinetics of cements by Time-Domain Nuclear Magnetic Resonance: application to Portland-cement-derived endodontic pastes, Cement and Concrete Research, V.42, pp.:577-582, 2012, DOI:10.1016/j.cemconres.2011.12.006.

117. A.C.A. Muller, K.L. Scrivener, A.M. Gajewicz, P.J. McDonald, Densification of C–S–H Measured by ^{1}H NMR Relaxometry. J. Phys. Chem., V 117, pp.:403–412, 2013, https://doi.org/10.1021/jp3102964.

118. A.M. Gajewicz, E. Gartner, K. Kang, P.J. McDonald, V. Yermakou, A ^{1}H NMR relaxometry investigation of gel-pore drying shrinkage in cement pastes. Cem. Concr. Res. V.86, pp.: 12-19, 2016, https://doi.org/10.1016/j.cemconres.2016.04.013.

119. F.K. Saleh, C. Teodoriu, C. Sondergeld, Review of NMR Studies for Oilwell Cements and Their Importance, *ChemEngineering*, V.*5(2)*:18, 2021, https://doi.org/10.3390/chemengineering5020018

120. V. Bortolotti, R.J.S. Brown, P. Fantazzini, M. Mariani, Evolution of a short-T2 liquid-like 1H signal during the hydration of White Portland Cement, Microporous and Mesoporous Materials, V.178, pp.:108-112, 2013, https://doi.org/10.1016/j.micromeso.2013.03.010.

121. V. Bortolotti, L. Brizi, R. J. S. Brown, P. Fantazzini, M. Mariani, Nano and Sub-nano Multiscale Porosity Formation and Other Features Revealed by ^{1}H NMR Relaxometry during Cement Hydration, Langmuir V. 30, pp.:10871−10877, 2014, https://doi.org/10.1021/la501677k.

122. S. Sykora, E. Vacchelli, V. Bortolotti, P. Fantazzini, New Universal NMR Sequences: PERFIDI and LAPSR, GIDRM - XXXVI National Congress on Magnetic Resonance, Salerno (Italy), 2006, https://doi.org/10.3247/SL1Nmr06.006.

123. Psi Plot, Poly Software International, Inc., USA.

124. G.C. Borgia, R.J.S. Brown, P. Fantazzini, Uniform-Penalty Inversion of Multiexponential Decay Data, Journal of Magnetic Resonance, V.132(1), 1998, pp.: 65-77, https://doi.org/10.1006/jmre.1998.1387.

125. G.C Borgia, R.J.S Brown, P Fantazzini, Uniform-Penalty Inversion of Multiexponential Decay Data: II. Data Spacing, T2 Data, Systematic Data Errors, and Diagnostics, Journal of Magnetic Resonance, V.147(2), 2000, pp.: 273-285, https://doi.org/10.1006/jmre.2000.2197.
126. Y.-Q. Song, L. Venkataramanan, M.D. Hürlimann, M. Flaum, P. Frulla, C. Straley, T1–T2 Correlation Spectra Obtained Using a Fast Two-Dimensional Laplace Inversion, Journal of Magnetic Resonance, V.154(2), 2002, pp.: 261-268, https://doi.org/10.1006/jmre.2001.2474.
127. Upen2DTool, Software DICAM, Upen2DTool, viewed 01/11/2021, <https://site.unibo.it/softwaredicam/en/software/2dupen>
128. Victoria University of Wellington Software
129. D. C. Meeker, Finite Element Method Magnetics, Version 4.2 (28Feb2018 Build), https://www.femm.info
130. Ansys® Discovery AIM, Release 2019R3.
131. MATLAB. version 9.6.0 (R2019a). Natick, Massachusetts: The MathWorks Inc.; 2019.
132. L. Quéval, "BSmag Toolbox User Manual," Tech. report, Dept. Elect. Eng., University of Applied Sciences Düsseldorf, Germany, April 2015. Available: http://www.lqueval.com [Accessed 01/10/2021].
133. H.J. Haugen, S. Bertoldi, Characterization of morphology—3D and porous structure (Characterization of Polymeric Biomaterials), Woodhead Publishing, 2017, pp.:21-53, https://doi.org/10.1016/B978-0-08-100737-2.00002-9.
134. R.A.B. Kogon, ^{1}H NMR relaxation characterization of hydrates, Doctoral Thesis, Dottorato di ricerca in fisica, Universita di Bologna, 2021.
135. R. Kleinberg, S.A. Farooqui, M. Horsfield, T_1/T_2 Ratio and Frequency Dependence of NMR Relaxation in Porous Sedimentary Rocks, Journal of Colloid and Interface Science, V.158, pp.:195–198, 1993, DOI: 10.1006/jcis.1993.1247.
136. A. C. A. Muller, K. L. Scrivener, A.M. Gajewicz, P.J. Mcdonald, Use of bench-top NMR to measure the density, composition and desorption isotherm of C–S–H in cement paste. Microporous and Mesoporous Mater, V.178(15), pp.:99-103, 2013, https://doi.org/10.1016/j.micromeso.2013.01.032.
137. E. Fukushima, J.A. Jackson, Unilateral magnet having a remote uniform field region for nuclear magnetic resonance, (US patent, Patent no.US6489872B1). Patent of New Mexico Resonance, Albuquerque, NM.

138. S. Utsuzawa, E. Fukushima, Unilateral NMR with a barrel magnet, J Magn Reson., V.282, pp.:104-113, 2017, DOI: 10.1016/j.jmr.2017.07.006.
139. G. Alberts, H. Hollis, H. LaBollita, G. Mueller, On the sensitivity of a laser heterodyne polarimeter for vacuum birefringence detection, UF Journal of Undergraduate Research, V.20(3), 2019, DOI: 10.32473/ufjur.v20i3.106302.
140. COMSOL Multiphysics® v. 5.6. www.comsol.com. COMSOL AB, Stockholm, Sweden.
141. C. Cadar, A. Cretu, M.Moldovan, C. Mattea, S. Stapf, I. Ardelean, NMR T_1-T_2 correlation analysis of molecular absorption inside a hardened cement paste containing silanised silica fume, Molecular Physics, V.117(7-8), pp.:1000-1005, 2019, https://doi.org/10.1080/00268976.2018.1513582.
142. S. Wild, M. Hadi, J. Khatib, The influence of gypsum content on the porosity and pore-size distribution of cured PFA—lime mixes, Advances in Cement Research, V.7(26), pp.:47-55, 1995, https://doi.org/10.1680/adcr.1995.7.26.47.
143. A. Bentur, K. Kovler, A. Goldman, Gypsum of improved performance using blends with Portland cement and silica fume, Advances in Cement Research, V.6(23), pp.:109-116, 1994.
144. A. Nagmutdinova, L. Brizi, P. Fantazzini, V. Bortolotti, Time domain NMR Pake-Doublet analysis of sorption cycles experiments of cement materials, Magnetic resonance and its applications. Spinus-2021 Saint Petersburg, 2021.
145. A. Nagmutdinova, L. Brizi, P. Fantazzini, V.Bortolotti, Investigation of the First Sorption Cycle of White Portland Cement by ^{1}H NMR. Appl Magn Reson 52, pp.:1767–1785, 2021, https://doi.org/10.1007/s00723-021-01436-w.
146. J.C. Mactavish, L. Miljković, M.M. Pintar, R. Blinc, G. Lahajnar, Hydration of white cement by spin grouping NMR. Cement and Concrete Research, V.15, pp.:367-377, 1985.
147. École Polytechnique Fédérale de Lausanne.

Appendix A

This Appendix contains models for multi-exponential fitting and solid-liquid anlasys of the raw NMR data. The models have been implemented by Bologna University NMR group using the scripting language of the technical plotting and data analysis software Psi-Plot(Poly Software International, NY, USA).

Here models with two exponents (two components with different $T_{1,2}$) are showed, but models could be easily adjusted for a greater number of components. In all models $T_{1,2}$ are calculated in ms, only for Solid curve fitting in QE model T_g is in μs.

CPMG

```
[INDVAR]: t
[DEPVAR]: S
[PARAMS]: Mo, P1, T21, T22
[EQUATIONS]:
S=Mo*(P1*exp(-t/T21)+(1-P1)*exp(-t/T22))
[INIT PARAMS]:
Mo = Mo_ini
P1=P1_ini
T21  = T21_ini
T22  = T22_ini
[LOWER LIMITS]:
Mo = 1
P1 = 0.1
T21 = 0.0001
T22 = 0.0001
[UPPER LIMITS]:
Mo = 100000
P1 = 0.99
T21  = 10000
T22  = 10000
ENDMODEL
```

The model is based on eq. 4.4.25, where Mo_ini, P1_ini, T21_ini, T22_ini are the initial values provided by the user and used for the regression of parameters. For better understanding we suggest reading the paragraph 4.4.2.4.

IR

```
[INDVAR]: t
[DEPVAR]: s
[PARAMS]: T11,P11,T12, M0
[EQUATIONS]:
s=M0-(P11*exp(-t/T11)+(1-P11)*exp(-t/T12))*2*M0
[INIT PARAMS]:
P11=P11_ini
T11= T11_ini
T12=T12_ini
M0 =M0_ini
[LOWER LIMITS]:
P11=0.01
T11=0.001
T12=0.001
M0 =1
[UPPER LIMITS]:
P11=0.99
T11=5000
T12=5000
M0 =10000
ENDMODEL
```

Where P11_ini, T11_ini, T12_ini, M0_ini are the initial values provided by the user and used for the regression of parameters. Model is based on eq. 4.4.26. For better understanding we suggest to read paragraph 4.4.2.5.

Scripts for the solid signal analysis with **QE** data

The first script is to separate liquid and solid parts from data measured at each tau used. And the second is for fitting the solid data curve. computed with the first script, and to find T_g of a sample. The fitting is based on eq. 4.4.28 and 4.4.29. For better understanding we suggest to read paragraph 4.4.3.

Solid + Liquid

```
[INDVAR]: t
[DEPVAR]: y
[PARAMS]: Xs, Xl, T2f, Ts
[EQUATIONS]:
y=Xs*exp(-1/2*(t/Ts)^2)+Xl*exp(-t/T2f)
```

[INIT PARAMS]:

Xs =Xs_ini

Ts = Ts_ini

Xl = X1_ini

T2f = T2f_ini

[LOWER LIMITS]:

Xs = 0.001

Ts = 0.001

Xl = 0.001

T2f = 0.001

[UPPER LIMITS]:

Xs = 1000

Ts = 1000

Xl = 10000

T2f = 10000

[START ROW]: Parameter depends on the raw data (point with the higher signal)

[END ROW]: Parameter depends on the raw data (number of points used)

ENDMODEL

Where Xs_ini, Ts_ini, X1_ini, T2f_ini are the initial values provided by the user and used for the regression of parameters.

Script to fit Solid data curve

[INDVAR]: tau

[DEPVAR]: y

[PARAMS]: Xs, Tg

[EQUATIONS]:

y=Xs*exp(-1/2*(tau/Tg)^2)

[INIT PARAMS]:

Xs = Xs_ini

Tg = Tg_ini

[LOWER LIMITS]:

Xs = 0.001

Tg = 0.001

[UPPER LIMITS]:

Xs = 100000

Tg = 1000

ENDMODEL

Where Xs_ini and Tg_ini are the initial values provided by the user and used for the regression of parameters.

Pake-Doublet fitting model

Here the model is written for two solid components (with amplitudes M1 and M2) and one liquid component (with amplitude M0). The model is based on the eq. 4.4.30. For better understanding we suggest to read paragraph 4.4.3.

```
[INDVAR]: t
[DEPVAR]: S
[PARAMS]: M0, M1, M2, Tg1, Tg2, a1, a2, T2f, b1, b2

[EQUATIONS]:
PI=3.14159
x1=sqrt(6*a1*t/PI)
x2=sqrt(6*a2*t/PI)
f1=(1+0.926*x1)/(2+1.792*x1+3.104*x1^2)
g1=1/(2+4.142*x1+3.492*x1^2+6.670*x1^3)
C1=1/2+f1*sin(PI/2*x1^2)-g1*cos(PI/2*x1^2)
S1=1/2-f1*cos(PI/2*x1^2)-g1*sin(PI/2*x1^2)
f2=(1+0.926*x2)/(2+1.792*x2+3.104*x2^2)
g2=1/(2+4.142*x2+3.492*x2^2+6.670*x2^3)
C2=1/2+f2*sin(PI/2*x2^2)-g2*cos(PI/2*x2^2)
S2=1/2-f2*cos(PI/2*x2^2)-g2*sin(PI/2*x2^2)
Sol1=a1*M1*sqrt(8*PI)*exp(-1/2*(t*b1)^2) * ( (cos(a1*t)/sqrt(a1*t))*C1 + (sin(a1*t)/sqrt(a1*t))*S1 )
Sol2=a2*M2*sqrt(8*PI)*exp(-1/2*(t*b2)^2) * ( (cos(a2*t)/sqrt(a2*t))*C2 + (sin(a2*t)/sqrt(a2*t))*S2 )
S=Sol1 + Sol2 + M0*exp(-t/T2f)

[INIT PARAMS]:
M0 =M0_ini
M1 = M1_ini
M2 = M2_ini
Tg1=Tg1_ini
Tg2=Tg2_ini
a1=a1_ini
a2=a2_ini
T2f=T2f-ini
b1=b1_ini
b2=b2_ini

[LOWER LIMITS]:
M0 = 1
```

M1 = 1

M2=1

Tg1=0.001

Tg2=0.001

a1=1

a2=1

T2f=0.001

b1=1

b2=1

[UPPER LIMITS]:

M0 = 1000000

M1 = 1000000

M2=1000000

Tg1=100

Tg2=100

a1=1000

a2=1000

T2f=1000

b1=1000

b2=1000

ENDMODEL

Where M0_ini, M1_ini, M2_ini, Tg1_ini, Tg2_ini, a1_ini, a2_ini, T2f-ini, b1_ini, b2_ini are the initial values provided by the user and used for the regression of parameters.

Appendix B

This part contains MATLAB code used for the magnetic flux density of a r.f. coil computation using the Biot-Savart law.

For the computation we modified the freeware Biot-Savart magnetic MatLab toolbox (ref .132).

The main changes implemented concerns the geometry of a coil and the number of wires used.

Here only parts concerning geometry is shown as other code could be accessed freely.

Square geometry

```
% Source points (where there is a current source)
Gamma = [0.005,0,0;
    0.175,0,0;
    0.175,0.17,0;
    0.005,0.17,0;
    0.005,0,0]; % x,y,z [m,m,m]
I = 0.1; % filament current [A]
dGamma = 1e-3; % filament max discretization step [m]


Gamma2 = [-0.005,0,0;
    -0.175,0,0;
    -0.175,0.17,0;
    -0.005,0.17,0;
    -0.005,0,0]; % x,y,z [m,m,m]]; % x,y,z [m,m,m]
I2 = 0.1; % filament current [A]
dGamma2 = 1e-3; % filament max discretization step [m]
```

Two rings geometry

```
% Source points (where there is a current source)
theta = linspace(0,pi*2,2*100);
Gamma = [0.09+0.085*(cos(theta')),0.085*(sin(theta')),0*(theta')]; %
x,y,z [m,m,m]
I = 0.1; % filament current [A]
dGamma = 1e9; % filament max discretization step [m]

theta2 = linspace(0,2*pi,2*100);
Gamma2 = [0.085*(cos(theta2'))-
0.09,0.085*(sin(theta2')),0*(theta2')]; % x,y,z [m,m,m]
I2 = 0.1; % filament current [A]
dGamma2 = 1e9; % filament max discretization step [m]
```

Archimedean spiral

```
% Source points (where there is a current source)
theta = linspace(0,pi*4,2*100);
Gamma =
[0.12+0.009*(theta'.*(cos(theta'))),0.01*(theta'.*(sin(theta'))),0*(t
heta')]; % x,y,z [m,m,m]
```

```
I = 0.1; % filament current [A]
dGamma = 1e9; % filament max discretization step [m]

theta2 = linspace(pi*4,0,2*100);
Gamma2 = [(0.009*(theta2'.*(cos(theta2'))))-
0.12,0.01*(theta2'.*(sin(theta2'))),0*(theta2')]; % x,y,z [m,m,m]
I2 = 0.1; % filament current [A]
dGamma2 = 1e9; % filament max discretization step [m]
```

Two rings

```
% Source points (where there is a current source)
theta = linspace(0,pi*2,2*100);
Gamma = [0.09+0.085*(cos(theta')),0.085*(sin(theta')),0*(theta')]; %
x,y,z [m,m,m]
I = 0.1; % filament current [A]
dGamma = 1e9; % filament max discretization step [m]

theta2 = linspace(0,2*pi,2*100);
Gamma2 = [0.085*(cos(theta2'))-
0.09,0.085*(sin(theta2')),0*(theta2')]; % x,y,z [m,m,m]
I2 = 0.1; % filament current [A]
dGamma2 = 1e9; % filament max discretization step [m]
```

Infinity symbol

```
% Source points (where there is a current source)
theta = linspace(-2*pi,pi*2,2*100);
Gamma = [0.17*(cos(theta'/2))/2,0.17*(sin(theta')/2),0*(theta')]; %
x,y,z [m,m,m]
I = 0.1; % filament current [A]
dGamma = 1e9; % filament max discretization step [m]
```

List of Figures

List of Tables